

High-Resolution Crystal Truncation Rod Scattering: Application to Ultrathin Layers and Buried Interfaces

Ankit S. Disa,^{*} Frederick J. Walker,^{*} and Charles H. Ahn^{*}

In crystalline materials, the presence of surfaces or interfaces gives rise to crystal truncation rods (CTRs) in their X-ray diffraction patterns. While structural properties related to the bulk of a crystal are contained in the intensity and position of Bragg peaks in X-ray diffraction, CTRs carry detailed information about the atomic structure at the interface. Developments in synchrotron X-ray sources, instrumentation, and analysis procedures have made CTR measurements into extremely powerful tools to study atomic reconstructions and relaxations occurring in a wide variety of interfacial systems, with relevance to chemical and electronic functionalities. In this review, an overview of the use of CTRs in the study of atomic structure at interfaces is provided. The basic theory, measurement, and analysis of CTRs are covered and applications from the literature are highlighted. Illustrative examples include studies of complex oxide thin films and multilayers.

1. Introduction

The diffraction of X-rays by crystals, as discovered by von Laue in 1912, allows one to determine a crystalline material's atomic structure—that is, the position of each atom within the material. Since the earliest scientific investigations, it has been realized that the physical properties exhibited by an object are intimately connected with its structure. Such properties may be, for instance, chemical, electrical, mechanical or optical in nature, and thus, X-ray diffraction has become a ubiquitous tool across the natural sciences.

Conventional X-ray diffraction and crystal structure determination, however, generally provide information about the atoms in the bulk of a 3D crystal. Modern technologies often rely on the unique interactions at the surface of a material or the behavior

at the interface between two materials in a heterostructure; consider, for instance, heterogeneous catalysis and semiconductor field effect transistors. The atomic structure at a crystalline surface or interface can differ considerably from that expected from the bulk. Hence, recent research has sought to understand structure–function relationships at surfaces and interfaces, with the aim of designing, controlling, and exploiting tailored interfacial systems.^[1]

This review focuses on the use of so-called crystal truncation rod (CTR) scattering, an extension of conventional X-ray diffraction, as a valuable and distinctive tool for determining the atomic structure of surface and interfacial systems. In short, the CTR technique can provide full information about the atomic constituents

and positions of surface and near-surface structures. Importantly, the technique is depth-sensitive and can be applied to heteroepitaxial systems with ultrathin layers (on the order of 10 nm or less) and even buried interfaces, which are often inaccessible by other surface characterization tools. Recently, progress in X-ray sources, detection, and data analysis has enabled CTR-based structural characterization of multilayered structures with picometer scale precision.

We begin the review with a short historical background of CTR scattering and surface X-ray diffraction.

1.1. Historical Background

Robinson was the first to use the term “crystal truncation rod,” in a paper published in 1986.^[2] In it, he wrote the basic expression for the X-ray scattering of an ideal crystal with a surface, which demonstrates the existence of extended scattering intensity perpendicular to the surface between the usual Bragg reflections of the 3D crystal. Andrews and Cowley had earlier obtained similar expressions for scattering and demonstrated that they could be observed with experimental measurements on GaAs(001) and KTaO₃(001) crystal surfaces.^[3] Robinson measured Pt(111), W(100), InSb(111), and Si(111) surfaces, and, most importantly, introduced a model of surface roughness which could fit the data in these dissimilar materials. The success of the model showed that angstrom scale surface roughness could be quantitatively determined from CTRs, hence validating its viability as a tool to study the structure at surfaces.

After these discoveries, the earliest applications of the technique concerned the surfaces of technologically relevant metals and semiconductors. Particular emphasis was given on the

Dr. A. S. Disa
Condensed Matter Department
Max Planck Institute for the Structure and Dynamics of Matter
22761 Hamburg, Germany
E-mail: ankit.disa@mpsd.mpg.de

Dr. F. J. Walker, Prof. C. H. Ahn
Department of Applied Physics and Center for Research on Interface Structures and Phenomena
Yale University, New Haven, CT 06520, USA
E-mail: fred.walker@yale.edu; Charles.ahn@yale.edu

 The ORCID identification number(s) for the author(s) of this article can be found under <https://doi.org/10.1002/admi.201901772>.

© 2020 The Authors. Published by WILEY-VCH Verlag GmbH & Co. KGaA, Weinheim. This is an open access article under the terms of the Creative Commons Attribution License, which permits use, distribution and reproduction in any medium, provided the original work is properly cited.

DOI: 10.1002/admi.201901772

effect of various treatment methods on common semiconductor substrates.^[4–7] Robinson showed that such scattering could access the structure at buried interfaces in measurements of interface roughness and stacking faults in Si(111) capped with amorphous Si and SiO₂ capping layers.^[8] In addition, simple metal surfaces provided valuable model systems for understanding of surface structure formation and temperature-dependent surface phase transitions.^[9–13] The temperature dependence and depth profile of surface segregation in a binary alloy (Cu₃Au (001)) was also observed for the first time using CTR scattering, which carried important implications for surface thermodynamics.^[14] These early works validated the efficacy of CTR scattering and helped develop standard methods for collecting and analyzing CTR data. Thorough reviews of these initial experiments have been written by Feidenhansl^[15] and Robinson.^[16]

The crystal truncation rod scattering technique is built, in large part, off of 2D surface X-ray diffraction techniques that had been developed earlier. In surface X-ray diffraction, a glancing incidence angle is used, often at or near the critical angle of X-ray total external reflection, in order to increase the scattering intensity of the X-rays from the surface layers.^[17–22] The resulting in-plane diffraction identifies, for instance, planar reconstructions of surfaces or monolayers relative to the bulk.^[23–27] In a sense, crystal truncation rod scattering represents the complement to surface X-ray diffraction. CTR studies are primarily concerned with the out-of-plane component of the surface scattering, which provides depth sensitivity, allowing for the complete layer-by-layer determination of the atomic structure near a surface or interface (or even multiple interfaces). A tandem structural analysis of surface and CTR scattering may also be used, which allows the out-of-plane structure of a reconstructed surface to be isolated and determined. One of the first studies to do so concerned the structure of chemisorbed oxygen on Cu(110), which ascertained the full in-plane and out-of-plane atomic structure of adsorbates on a crystalline surface.^[28]

1.2. Advantages and Disadvantages

The toolbox of structural characterization techniques for physicists, materials scientists, and chemists is overflowing. The crystal truncation rod technique offers both advantages and disadvantages relative to other well-established tools for studying surfaces and interfaces, which include scanning and wide-field transmission electron microscopy (STEM and TEM), scanning tunneling microscopy (STM), atomic force microscopy (AFM), and X-ray microscopy (XRIM). Practical considerations for the choice of CTR analysis versus other methods might include the spatial resolution, interface sensitivity, possible sample environments, destructiveness, and experimental requirements.

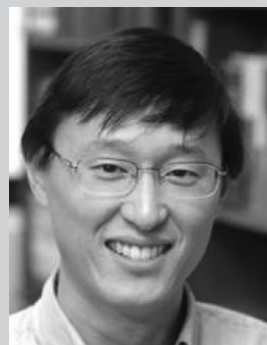
CTR scattering is, first and foremost, an X-ray-based technique, possessing all of the pros and cons therewith. As X-rays penetrate deeply into matter (tens to hundreds of micrometers at typical hard X-ray energies), the CTR technique can access structural information related to buried interfaces especially relevant to thin films and heterostructures, unlike surface microscopy techniques like STM and AFM. Furthermore, CTR



Ankit S. Disa is an Alexander von Humboldt postdoctoral research fellow, currently at the Max Planck Institute for the Structure and Dynamics of Matter in Hamburg, Germany. He received his B.S. from Cornell University and his Ph.D. from Yale University in Applied Physics. His research has focused on controlling electronic and magnetic order in correlated materials using atomic layer heterostructuring and ultrafast optical approaches.



Frederick J. Walker is currently Senior Research Scientist in the Department of Applied Physics at Yale University. Prior to joining Yale, he was a Research Professor at Oak Ridge National Laboratory working with Dr. Rodney McKee. He is an expert in the fabrication of epitaxial thin film heterostructures by molecular beam epitaxy and their characterization using synchrotron-based methods. His research focuses on the physics of crystalline oxides on semiconductors, chalcogenide and oxide heterostructures, and high-resolution X-ray characterization of heterointerfaces.



Charles H. Ahn is John C. Malone Professor of Applied Physics, Mechanical Engineering & Materials Science, & Physics at Yale University. He received his Ph.D. from Stanford University and carried out postdoctoral research at the University of Geneva. He is a leader in the study of functional behavior in complex oxide heterostructures, focusing on ferroelectrics, advanced dielectrics, correlated magnets, and high temperature superconductors.

scattering is a nondestructive characterization tool, requiring no special sample processing or environmental conditions. This advantage contrasts with STEM and TEM imaging, in which samples must be mechanically thinned and/or ion milled until they are electron transparent. In general, CTR experiments can be performed in ambient conditions or in temperature-controlled, gaseous, and even liquid environments (see discussion

in Section 4). Thus, CTR scattering also lends itself quite naturally to in situ and in operando studies of materials and devices

In terms of spatial resolution of atomic positions, high-quality CTR data sets measured at synchrotron X-ray sources routinely provide layer-resolved atomic positions with precisions in the range of 1–10 pm in the surface normal direction. Experimental factors such as instrumental resolution, crystalline quality, and the reliability of phase retrieval and/or structural refinement procedures influence the uncertainty in extracted structural parameters.^[29] High-resolution STEM and TEM analysis using new image processing techniques now also can approach this level of precision,^[30] providing real-space information which can complement CTR-derived parameters.

CTR scattering, however, generally requires the use of synchrotron facilities to achieve the highest resolutions. This requirement stems from the fact that the signal to background is weak: the intensities in the CTR regions are several orders of magnitude weaker than the bulk Bragg reflections. Thus, the high X-ray brightness available at synchrotron sources is needed to resolve structural features related to ultrathin layers with sufficient contrast. Another relevant aspect of the technique is that it provides spatially averaged information within the probe volume of the X-rays, which can be regarded as either an advantage or disadvantage. The typical size of the focused X-ray beam at the sample position at a synchrotron beamline may be in the range of a few to hundreds of micrometers. Newer synchrotron sources with dedicated nanoprobe beamlines can achieve spot sizes on the order of tens to hundreds of nanometers. Still, CTR measurements do not allow the local atomic scale sensitivity available to scanning microscopy techniques, which means that inhomogeneities complicate the structural analysis; here, CTR analysis may be guided by local probes, such as various electron microscopies, to tackle the existence of multiple domains or defect structures. Taking all of this into account, it is clear that certain applications exist that lend themselves to CTR measurements—in particular, those in which buried interfaces and nondestructive structural determination with atomic scale resolution are crucial. As is evident from the experimental works discussed in this review, the current research landscape allows for multiple techniques to be used to study the same materials system or problem. Using CTR scattering and STEM imaging in concert, researchers have revealed new and interesting structural features, such as polarization in metallic systems^[31] and the transfer of octahedral rotations across interfaces.^[32,33]

1.3. Scope of Review

The history and literature of the crystal truncation rod scattering technique are vast, covering all varieties of materials and applications from surface reconstructions of simple metals to the electrochemistry of geological minerals. In this review, we seek to focus on the contemporary applications of the technique to structural determination in epitaxial thin films and buried interfaces. Particular emphasis is given to complex oxide heterointerfaces, an area of burgeoning interest with a proliferation of recent CTR studies.

We hope to emphasize here that CTR analysis is a useful tool for understanding how materials structures are modified at

interfaces, which can be related to observed macroscopic functionalities (electronic, magnetic, chemical, and others). Hence, CTR methods are used as standard tools in efforts to develop new materials with desired properties. Moreover, state-of-the-art CTR-based characterization is an integral component of picoscale materials engineering efforts, which combine growth, characterization, and theoretical modeling to tune functional behavior through structural manipulation at interfaces.^[1]

Section 2 continues with a basic overview of the theory of crystal truncation rod scattering, beginning with conventional X-ray diffraction and including a discussion of commonly used structural analysis and phase retrieval methods. In Section 3, we summarize the major CTR studies carried out on various materials classes, mostly over the last 20 years. We give most attention to in-depth studies on complex oxide interfaces combining experimental and theoretical analyses, which have led to new insights on interfacial control of functional behavior. In the final section, Section 4, we synthesize general findings from CTR experiments and mention emerging trends and future developments involving such types of measurements.

2. Theory and Measurement of CTRs

2.1. General Treatment of X-Ray Scattering

In this section, we review the basic formulation of X-ray diffraction from a crystal (following, e.g., ref. [34]). The discussion forms the basis for CTR analysis of interface and surface structures. This section also serves to establish the terminology and notation used throughout the text. For the purposes of this review, we start with the classical interaction of X-rays with electrons.

We assume an incident electromagnetic plane wave whose electric field at time t and position \vec{r} is given by

$$E_i = A_i e^{i(\vec{k}_i \cdot \vec{r} - \omega t)} \quad (1)$$

where $\vec{k}_i = \frac{2\pi}{\lambda} \hat{r}_i$ with λ the wavelength and \hat{r}_i a unit vector pointing along the propagation direction of the wave. An electron interacting with such a field oscillates at frequency ω , leading to a time-varying dipole and emission of an electromagnetic wave at the same frequency. For $\hbar\omega$ much larger than the binding energy of the electron, the amplitude of the radiated wave at a position \vec{R} relative to the electron is (in cgs units)

$$E_e = p A_i \frac{e^2}{mc^2} \frac{e^{-i(\vec{k}_f \cdot \vec{R} - \omega t)}}{|\vec{R}|} \quad (2)$$

where e and m are the charge and mass of the electron, respectively, and c is the speed of light. Here, $\vec{k}_f = \frac{2\pi}{\lambda} \hat{r}_f$ points along the direction from the electron to \vec{R} . The factor $p = |\hat{r}_f \times (\hat{r}_i \times \hat{E}_i)|$ depends on the polarization of the incident wave (\hat{E}_i) relative to the scattering plane, which is the plane that contains \vec{r}_i and \vec{r}_f . For \hat{E}_i normal to the scattering plane (σ polarization) $p = 1$, and for \hat{E}_i in the scattering plane (π polarization) $p = \cos 2\theta$, where 2θ is the angle between incident and scattered waves.

Equation (2) is the Thomson scattering formula and the value $r_e = \frac{e^2}{mc^2} \approx 2.8 \times 10^{-5} \text{ \AA}$ is the classical electron radius. The scattering process considered here is elastic and we are interested in time-averaged quantities, so we hereafter omit the explicit time dependence of the scattered electromagnetic field.

As r_e and hence the scattered wave amplitude are relatively small, we make use of the kinematical approximation when considering the X-ray diffraction arising from atoms and crystals, in which the total scattered amplitude from an ensemble of electrons is taken as the sum of the scattered wave amplitudes from each individual electron. Within the kinematical approximation, we may calculate the scattering amplitude from an electron distribution whose density is given by $\rho(\vec{r})$ with the integral

$$E_\rho = p A_i r_e \int_V \frac{\rho(\vec{r}) e^{-i(\vec{k}_f \cdot (\vec{R} - \vec{r}) + \vec{k}_i \cdot \vec{r})}}{|\vec{R} - \vec{r}|} d\vec{r} \quad (3)$$

The additional factor $e^{-i\vec{k}_i \cdot \vec{r}}$ gives the relative phase of the wave scattered from position \vec{r} versus that scattered from the origin. Assuming the detector position $|\vec{R}| \gg |\vec{r}|$, the denominator becomes $|\vec{R}|$ and can be pulled out of the integral. We also ignore the term $e^{-i\vec{k}_f \cdot \vec{R}}$ as it does not affect the scattered wave interference. Then, we are left with

$$E_\rho(\vec{q}) = p \frac{A_i r_e}{|\vec{R}|} \int_V \rho(\vec{r}) e^{i\vec{q} \cdot \vec{r}} d\vec{r} \quad (4)$$

The vector $\vec{q} = \vec{k}_f - \vec{k}_i$ is known as the scattering vector or momentum transfer. It is the fundamental independent variable in any X-ray diffraction experiment. Its magnitude $|\vec{q}| = \frac{4\pi \sin \theta}{\lambda}$ is dependent on the scattering angle (2θ) and the wavelength of radiation (λ). A schematic of the typical scattering geometry is shown in **Figure 1**. In most cases, we are concerned with monochromatic X-ray diffraction measurements, in which the scattering angle is varied at a fixed wavelength.

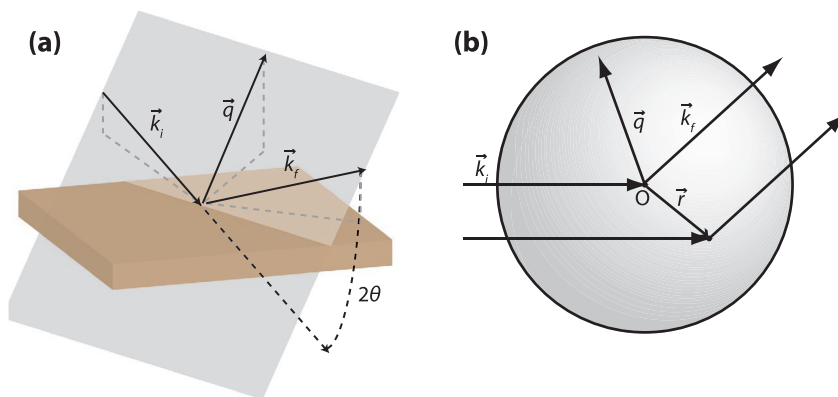


Figure 1. a) Geometry of a typical X-ray scattering measurement depicting the incident wavevector \vec{k}_i , the final wavevector, \vec{k}_f , and the scattering vector or momentum transfer, \vec{q} . The scattering angle, 2θ is shown as the angle between \vec{k}_i and \vec{k}_f , which determines the magnitude of \vec{q} . b) Depiction of scattering from an electron distribution, where O is the real space origin and \vec{r} is the position vector within the distribution.

From Equation (4) one can see that the amplitude of the X-ray diffraction from a medium represents the Fourier transform of the medium's electron density distribution. Therefore, if one had knowledge of $E_\rho(\vec{q})$ for all \vec{q} , an inverse Fourier transform operation would provide knowledge of the spatial distribution of electrons, which, for most condensed matter, is tantamount to knowing the atomic structure of the material—that is, the location and charge of every atom that makes up the material. It is for this reason that X-ray scattering has been an invaluable tool for characterizing the structure of materials for over a hundred years.

The focus of this review is on the study of surfaces and interfaces of crystalline materials. We continue to develop the basic theory by applying Equation (4) to a crystal, which we assume is formed by a repeating lattice of unit cells composed of a basis of atoms. The full scattered wave amplitude from the crystal is thus generated (taking advantage of the kinematical approximation) by superimposing the X-ray scattering amplitude of each atom in the unit cell and each unit cell in the crystal. The extension to crystal truncation rod scattering from surfaces and interfaces is carried out in the next section (Section 2.3).

2.1.1. Atomic Form Factor

For an atom, the quantity

$$f_a(\vec{q}) = \int_{V_{\text{atom}}} \rho(\vec{r}) e^{i\vec{q} \cdot \vec{r}} d\vec{r} \quad (5)$$

is the atomic form factor, also known as the atomic scattering factor. This quantity represents the scattering amplitude (excluding prefactors) arising from the electron density of a single atom. We adopt the usual assumption used in X-ray diffraction that $\rho(\vec{r})$ for the atom is spherically symmetric, so that $f_a(\vec{q}) = f_a(|\vec{q}|)$. For all atoms, $f_a(|\vec{q}|)$ behaves similarly, with a maximum value at $|\vec{q}| = 0$ and a decay as $|\vec{q}| \rightarrow \infty$. Notice that $f_a(|\vec{q}| = 0) = Z$, where Z is the atomic number. As a result, X-ray scattering is generally insensitive to light elements and gives

weak contrast between adjacent elements in the periodic table. The energy dependence of $f_a(|\vec{q}|)$, which we are ignoring at the moment, provides a way to overcome such limitations.

The utility of defining the atomic form factor is that the value of $f_a(|\vec{q}|)$ can be determined for a given atom and employed in the calculation of a material's X-ray scattering amplitude. A commonly used approximation is to assume the $f_a(|\vec{q}|)$ takes the form of a four-component Gaussian

$$f_a(q) = \sum_{i=1}^4 a_i e^{-b_i \frac{|\vec{q}|^2}{4\pi}} + c \quad (6)$$

Values of the coefficients of Equation (6) have been tabulated for most atoms in the periodic table and common ionic species and

can be found in various sources.^[35] The coefficients are obtained by the evaluation of Equation (5) with $\rho(\vec{r})$ determined by quantum mechanical calculations of the atomic wavefunction.

2.1.2. X-Ray Scattering from Crystals

To determine the X-ray scattering amplitude from a crystal, we consider first the scattering from an individual unit cell of the crystal. The atomic form factor can be used in the computation of the unit cell's scattering amplitude. One can simply sum up the contributions from each atom within the unit cell. The result is the structure factor

$$F(\vec{q}) = \sum_j f_j(|\vec{q}|) e^{i\vec{q} \cdot \vec{r}_j} \quad (7)$$

where $f_j(|\vec{q}|)$ is the form factor for the atom at position \vec{r}_j within the unit cell.

Finally, the scattered wave amplitude from the entire crystal, from Equation (4), is written as a sum over the scattering from each unit cell

$$E_c(\vec{q}) = A_i \frac{r_e}{|\vec{R}|} F(\vec{q}) \sum_n e^{i\vec{q} \cdot \vec{R}_n} \quad (8)$$

Here, \vec{R}_n is the position of the origin of unit cell n within the crystal lattice, and the sum is carried out over all unit cells of the illuminated region of the crystal.

2.1.3. Debye–Waller Factor

Until now we have assumed that the atoms in the crystal are fixed in their equilibrium positions. We have ignored vibrations of the atoms as a result of thermal fluctuations, which can significantly affect the scattered intensity. We can incorporate such fluctuations by allowing that the position of an atom j in unit cell n can be instantaneously displaced at a given time relative to its equilibrium position: $\vec{r}_{j,n}(t) = \vec{r}_{j,n} + \vec{u}_{j,n}(t)$. This modifies Equation (8) to include a time-varying term

$$E_c(\vec{q}) = A_i \frac{r_e}{|\vec{R}|} \sum_j f_j(q) e^{i\vec{q} \cdot \vec{r}_j} \sum_n e^{i\vec{q} \cdot \vec{R}_n} e^{i\vec{q} \cdot \vec{u}_{j,n}(t)} \quad (9)$$

The time scale of a typical X-ray scattering measurement is much slower than the time scale of atomic motions; hence, the time average of $E_c(\vec{q})$ is relevant. Only the last factor has a time dependence, and its time average is generally evaluated in the harmonic approximation

$$\langle e^{-i\vec{q} \cdot \vec{u}} \rangle \approx e^{-\frac{1}{2} \langle (\vec{q} \cdot \vec{u})^2 \rangle} \quad (10)$$

$$\approx e^{-\frac{1}{6} q^2 \langle u^2 \rangle} \quad (11)$$

In terms of the X-ray scattering intensity, this term becomes

$$F_{DW} = e^{-\frac{1}{3} q^2 \langle u^2 \rangle} \quad (12)$$

which is known as the Debye–Waller factor. F_{DW} essentially can be thought of as a modification to the atomic form factors. The value of $\langle u^2 \rangle$, which is often written in terms of the so-called B -factor $= 8\pi^2 \langle u^2 \rangle$, depends on temperature, atomic species, and crystal, and it can be anisotropic. F_{DW} must often be taken into account when modeling X-ray data, entering as a fitting parameter (or it may be calculated from first-principles via the phonon spectrum).

2.1.4. Detection of X-Ray Intensity

Crucially, detectors used in X-ray scattering experiments are sensitive not to the field amplitude, but rather the intensity, or the number of X-ray photons impinging on the detector area in a given time. Thus, the detected quantity is given by

$$I_c(\vec{q}) = \frac{1}{2} \eta \frac{n\epsilon_0}{c} |E_c(\vec{q})|^2 \quad (13)$$

where n is the refractive index, ϵ_0 is the vacuum permittivity, and η is related to the detection process (efficiency, conversion factors, etc.) and will vary from instrument to instrument.

The significance of the experimental detection of $I_c(\vec{q})$ is that all phase information contained in $E_c(\vec{q})$ is eliminated. For instance, consider a crystal with an electron density $\rho_A(\vec{r})$, leading to the scattered X-ray field $E_A(\vec{q})$ and another with electron density $\rho_B(\vec{r})$, which happens to give a scattered X-ray field $E_B(\vec{q}) = E_A(\vec{q}) e^{i\phi}$, where ϕ is some arbitrary phase. While representing different electron density profiles, the measured intensity in an experiment for both crystals would correspond to $I_A(\vec{q}) = I_B(\vec{q}) = |E_A(\vec{q})|^2$. Thus, direct Fourier inversion of Equation (8) from an X-ray diffraction experiment to arrive at $\rho(r)$ for the entire crystal is in general not possible; this is often referred to as the phase problem of X-ray diffraction. However, various specialized techniques have been developed to deal with this issue and extract the relevant information for a given material or problem, which are discussed in Section 2.6.

2.1.5. Dynamical Effects

All of the results above have been derived assuming the kinematical theory of X-ray diffraction from crystals. This approximation assumes that all scattered X-rays interact only once with the sample and each scattering event can be treated independently. In principle, this approximation breaks down when the scattering cross-section is high, as is the case when \vec{q} is very close to a Bragg point. Then, multiple scattering events become likely and a more complete dynamical treatment must be used to compute the scattered wave amplitude. In the context of crystal truncation rod scattering, several theoretical studies of the dynamical scattering intensity for surface and interfaces have been carried out using model or exact numerical calculations.^[17,36–40] While strong deviations are found close to the Bragg peaks, the kinematical theory is shown to be approximately valid until $\approx 0.001 \text{ \AA}^{-1}$ or ≈ 0.01 reciprocal lattice units (R.L.U., see Section 2.3) of the Bragg peak for all investigated systems. Moreover, the kinematical

approximation agrees with the dynamical treatment down to intensities of at least 10^{-7} of the peak intensity.^[39] For this reason, structural analyses of crystal truncation rods typically omit wavevectors sufficiently close to the Bragg peak in order to avoid dynamical effects.

Additional modifications come from the fact that X-rays have a finite cross-section of absorption with matter, which has the effect of attenuating the impinging X-ray field magnitude as a function of propagation distance, z . Assuming linear absorption, the incident X-ray magnitude follows the form $A(z) = A_0 e^{-\mu z}$, where μ^{-1} is the attenuation length. The attenuation length depends on the material's density, elemental components, incident angle, and X-ray energy.^[35] This effect can be taken into account by including the exponential term in the calculation of the structure factor. Absorption has the impact of reducing the scattered intensity as it restricts the probed region to a finite volume. In addition, self-absorption of diffracted X-rays gives rise to an additional nontrivial \vec{q} -dependence of the scattered X-ray intensity, again limiting the validity of kinematical models close to Bragg peaks.

As with visible light, the reflection and transmission of X-rays can be strongly affected by refraction at interfaces. The refractive index for crystalline materials at hard X-ray wavelengths is typically written as $n = 1 - \delta + i\beta$, where δ and β are both positive and small. The imaginary component $\beta = \frac{\mu}{|k|}$

is given by the magnitude of the incident wavevector $|k| = \frac{2\pi}{\lambda}$ and the attenuation length. For the real part of n , the deviation from unity can be approximated as $\delta \approx \frac{r_e \lambda^2 n_a Z}{2\pi}$, where n_a is the

formula unit number density and Z is the number of electrons per unit. Because the real part of $n < 1$ in the X-ray regime, total external reflection occurs below a certain critical angle of the incident beam, in analogy with total internal reflection of visible light. The critical angle is given by $\alpha_c = \cos^{-1}(n) \approx \sqrt{2\delta}$, which is usually in the range $\approx 0.1^\circ$ to 1° .^[35] For the incident X-ray angle $\alpha < \alpha_c$, the (specular) reflectivity is close to unity and an evanescent wave propagates along the interface with an attenuation length given by $\frac{1}{2|k|\sin\alpha_c}$, which is < 10 nm for

most materials. When $\alpha = \alpha_c$, the incident and reflected waves interfere constructively, enhancing the intensity of the evanescent field by up to a factor of four.^[41,42] This effect has been used to increase the strength of X-ray diffraction from surface structures in surface X-ray diffraction and CTR studies.

2.2. Anomalous Scattering

In principle, the above treatment may be used to take into account both the energy and angular dependence of the X-ray scattering intensity through different values of q . However, in the vicinity of atomic transitions, the atomic form factor can change dramatically and take on complex values. As a result, if the incident X-ray energy E is scanned through a transition of a constituent element of a material, the scattered X-ray intensity will be modified for a given q ; that is, the scattered intensity becomes a function of both q and E . This feature may be

harnessed to extract element specific information from X-ray diffraction measurements, since different atoms possess distinct transition energies. The use of this energy dependence to isolate structural features due to particular species is generally termed anomalous scattering.^[43,44] As discussed in Section 3, the technique can also be extended to surfaces and interfaces by incorporating anomalous scattering into CTR measurements (see also refs. [45–49]).

2.3. Basic Models

Equations (5)–(13) form the basis of conventional X-ray scattering techniques. We proceed by using a simple model, which provides a convenient way to understand the emergence of crystal truncation rods when a surface is introduced to a 3D crystal. It also affords a basis upon which the scattering from complex surface structures and interfaces can be understood. We formulate the model within the kinematical theory, ignoring dynamical effects and absorption. Therefore, the results are only applicable in regions sufficiently far from the bulk Bragg reflections (Section 2.1.5). For convenience, in this and the following sections, we also adopt the convention of assuming the prefactors in Equations (8) and (13) to be included in the definition of $F(\vec{q})$.

2.3.1. Infinite Crystal

We first treat an infinitely large 3D crystal in order to define the Bragg peaks and reciprocal lattice. Consider a crystal whose lattice can be indexed by the orthogonal lattice vectors $\{\vec{a}, \vec{b}, \vec{c}\}$ (although the result can be generalized to any Bravais lattice). The origin of each unit cell in the lattice is given by $\vec{R}_n = n_1 \vec{a} + n_2 \vec{b} + n_3 \vec{c}$ for integers n_1 , n_2 , and n_3 . Then, from Equation (13), the measured X-ray diffraction intensity is

$$I_{3D}(\vec{q}) = \left| F(\vec{q}) \sum_{n_1, n_2, n_3} e^{i(\vec{q} \cdot \vec{R}_n)} \right|^2 \quad (14)$$

$$= \left| F(\vec{q}) \sum_{n_1, n_2, n_3} e^{i(n_1 q_a a + n_2 q_b b + n_3 q_c c)} \right|^2 \quad (15)$$

where $q_a = \vec{q} \cdot \hat{a}$, $q_b = \vec{q} \cdot \hat{b}$, and $q_c = \vec{q} \cdot \hat{c}$. For an infinitely large crystal (letting $-\infty < n_1, n_2, n_3 < \infty$), we can exploit the identity for the Dirac delta function

$$\frac{1}{2\pi} \sum_{m=-\infty}^{\infty} e^{inx} = \delta(x - 2\pi m) \quad (16)$$

which is valid for any Brillouin zone centered around $2\pi m$, where m is an integer. Using this, Equation (15) becomes

$$I_{3D}(\vec{q}) = \left| F(\vec{q}) (2\pi)^3 \sum_{h,k,l} \delta(q_a a - 2\pi h) \delta(q_b b - 2\pi k) \delta(q_c c - 2\pi l) \right|^2 \quad (17)$$

The above equation demonstrates that, within the kinematical approximation, in a 3D crystal of infinite extent one observes scattering only for isolated values of \vec{q} where

$$\vec{q} \cdot \vec{a} = 2\pi h, \quad \vec{q} \cdot \vec{b} = 2\pi k, \quad \vec{q} \cdot \vec{c} = 2\pi l \quad (18)$$

These are the well-known Laue conditions and the integers h , k , and l are the Miller indices which dictate the allowed values of the scattering vector \vec{q} to observe diffraction. For the orthogonal real-space lattice used in this example, the vectors $\{\vec{a}^*, \vec{b}^*, \vec{c}^*\} = \left\{ \frac{2\pi\hat{a}}{a}, \frac{2\pi\hat{b}}{b}, \frac{2\pi\hat{c}}{c} \right\}$ and the Miller indices define

the reciprocal lattice: $\vec{G} = h\vec{a}^* + k\vec{b}^* + l\vec{c}^*$. It is often the case that the scattering vector is given in R.L.U., in which \vec{q} is defined in the basis of the reciprocal lattice vectors. When employing these units, we write the indices as H , K , and L , which can take on noninteger values. In this language, the Laue conditions can be written very simply as

$$\vec{q} = \vec{G} \quad (19)$$

which is also identical to the Bragg's law expression

$$n\lambda = 2d_{hkl} \sin \theta \quad (20)$$

where n is an integer and $d_{hkl} = \frac{2\pi}{|\vec{G}|}$ is the spacing between adjacent planes normal to the (hkl) direction in real space.

2.3.2. Half-Infinite Crystal

Now, we consider a crystal with a surface. As an example, we take a surface which is cut along a plane perpendicular to the c -axis. In this case, the crystal now has a finite number of planes, N_c , along the c -axis. Consequently, we take the sum over n_3 in Equation (17) from 1 to N_c , while the rest of the expression remains identical

$$I_{2D}(\vec{q}) = \left| F(\vec{q}) \sum_{n_1, n_2=0}^{\infty} e^{i(n_1 q_a a + n_2 q_b b)} \sum_{n_3=1}^{N_c} e^{i n_3 q_c c} \right|^2 \quad (21)$$

Instead of a Dirac delta function, the last summation in the equation can be expressed in closed form as a ratio of sinusoidal functions. Plugging into 21 gives

$$I_{2D}(\vec{q}) = \left| F(\vec{q}) (2\pi)^2 \sum_{h,k} \delta(q_a a - 2\pi h) \delta(q_b b - 2\pi k) \frac{\sin\left(\frac{N_c q_c c}{2}\right)}{\sin\left(\frac{q_c c}{2}\right)} \right|^2 \quad (22)$$

To understand how the scattered wave intensity behaves in 2D, we examine some limits. First, in the extreme case of a 2D crystal with a single plane perpendicular to the c -axis such that $N_c = 1$, the last term in Equation (22) becomes unity. The scattered intensity in this case is independent of q_c —i.e., as long as the in-plane Bragg conditions are satisfied ($q_a = \frac{2\pi h}{a}$ and $q_b = \frac{2\pi k}{b}$) a uniform “rod” of scattering exists along $\frac{a}{q_c}$, modulated by

$F(\vec{q})$. This behavior is a simple manifestation of the crystal truncation rod.

Another relevant limit is that of large but finite $N_c \gg 1$, emulating the case of a macroscopic crystal with a well-defined surface. In this limit, the numerator in the last term of Equation (22) varies rapidly with q_c . One may then separate it and use its average value, $\langle |\sin\left(\frac{N_c q_c c}{2}\right)|^2 \rangle = \frac{1}{2}$. The scattered intensity becomes

$$I_{2D}(\vec{q}) = \frac{1}{2} \left| F(\vec{q}) (2\pi)^2 \sum_{h,k} \delta(q_a a - 2\pi h) \delta(q_b b - 2\pi k) \frac{1}{\sin\left(\frac{q_c c}{2}\right)} \right|^2 \quad (23)$$

This equation diverges along q_c near the Bragg points of the reciprocal lattice, $q_c = \frac{2\pi l}{c}$; however, significant intensity remains in between. The minimal intensity is at the anti-Bragg position exactly in between two adjacent reciprocal lattice points ($q_c = \frac{\pi(2l+1)}{c}$) where the value of the last term in Equation (23) is unity. This type of long-ranged scattering extending away from the Bragg point is another instance of a CTR. Figure 2a shows the ideal CTR intensities for the two limits of Equation (22) discussed above.

One of the important features of CTRs is that they allow one to measure nonzero scattering intensity over an expanded range of \vec{q} compared with that provided by bulk Bragg scattering. From such extended scattering one can determine the structure factor (or rather $|F(\vec{q})|^2$) throughout the entire Brillouin zone in the q_c direction. Hence, CTRs provide detailed information about the atomic structure of the truncated surface (as well as for thin films and interfaces, as discussed below).

2.4. Surface and Interfacial Effects

2.4.1. Relaxed and Reconstructed Surfaces

Simple models can be used to elucidate the dependence of CTR scattering on structural changes at interfaces. First, we consider a truncated crystal in which the surface layer has a relaxed or distorted structure relative to the bulk. We assume that the lattice of the surface layer is identical to the bulk in the lateral direction (i.e., not reconstructed), but the spacing in the c -direction can change. In this case, we simply modify Equation (21) such that the structure factor of the surface layer differs from the rest of the crystal

$$I(\vec{q}) = \left| \sum_{n_1, n_2=0}^{\infty} e^{i(n_1 q_a a + n_2 q_b b)} \left(F_b(\vec{q}) \sum_{n_3=1-N_c}^{-1} e^{i n_3 q_c c} + F_s(\vec{q}) \right) \right|^2 \quad (24)$$

$F_b(\vec{q})$ is the structure factor of the bulk crystal, and $F_s(\vec{q})$ is the structure factor of the surface layer, which is modified or relaxed relative to the interior of the crystal. To ease the computation, we have changed the origin of the crystal to the surface. Taking $N_c = 1$ leaves only the surface layer present in Equation (24).

For N_c large, the first term in 24 is identical to Equation (23) and the second term gives uniform rods of scattering as in the

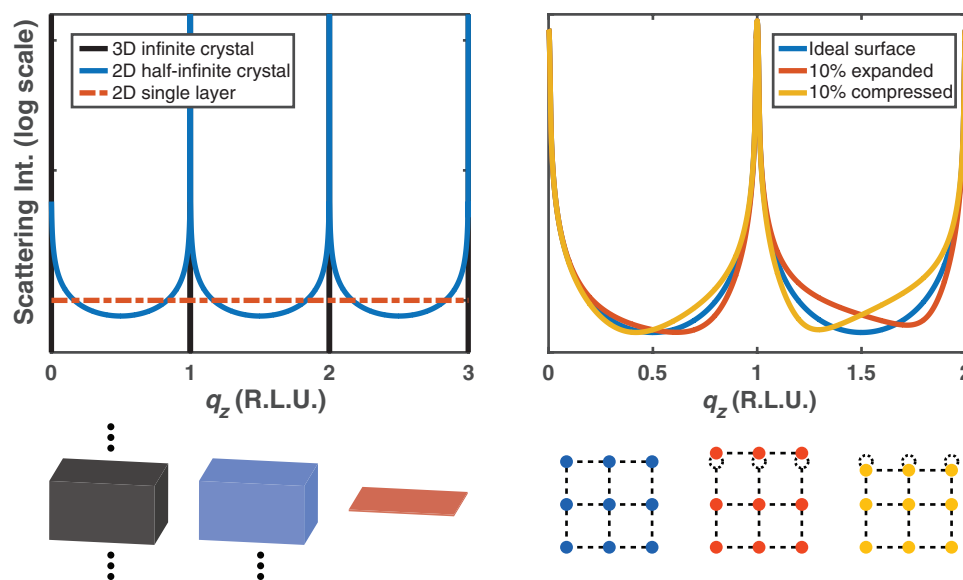


Figure 2. (Left) Ideal scattering from an infinite 3D crystal, a half-infinite layer with a sharp boundary, and a single 2D layer with no thickness. (Right) Changes in the CTR profile for a surface layer with uniform relaxation. The scattering vector is given in reciprocal lattice units (R.L.U.) along the z direction (i.e., in units of L).

2D limit of Equation (22), albeit with different structure factors. The interference of these two terms changes the scattering intensity in a way that depends on the particular forms of the bulk and surface structure factors $F_b(\vec{q})$ and $F_s(\vec{q})$. An example is shown in Figure 2b, demonstrating the differences in scattering intensity for different surface reconstructions. Changes in atomic positions of a few percent of a single atomic layer on the surface of a crystal create measurable differences in the CTR scattering. Considering most crystals with typical atomic spacings of a few angstroms, this model implies that CTR scattering can be sensitive to changes in atomic positions on the picometer-scale in absolute terms.

Another common type of response of a crystal surface or epitaxial layer is to reduce the in-plane symmetry relative to the bulk material. Such a surface reconstruction can be incorporated by allowing the in-plane lattice of the surface layer to differ from the bulk lattice. One can rewrite Equation (24) to accommodate this as follows

$$I(\vec{q}) = \left| F_b(\vec{q}) \sum_{n_1, n_2=0}^{\infty} e^{i(n_1 q_a a + n_2 q_b b)} \sum_{n_3=1-N_c}^{-1} e^{i n_3 q_c c} + F_s(\vec{q}) \sum_{n_1, n_2=0}^{\infty} e^{i(p_1 n_1 q_a a + p_2 n_2 q_b b)} \right|^2 \quad (25)$$

The factors p_1 and p_2 are the relative periodicity of the surface to the bulk along the a and b directions. As before, the CTRs are modulated due to bulk and surface interference for values of \vec{q} corresponding to the in-plane bulk reciprocal lattice vectors h and k (as in Equation (24)). In addition, 2D rods of scattering now appear at fractional values of h and k —in particular, at integer multiples of $h_s = \frac{h}{p_1}$ and $k_s = \frac{k}{p_2}$. Those fractional order rods or superstructure rods that do not coincide with a bulk reciprocal lattice vector purely arise from the reconstructed surface layer and thus can be used to extract information about the surface structure factor $F_s(\vec{q})$.

2.4.2. Epitaxial Thin Films and Multilayers

One can extend the above formalism to account for epitaxial thin films on bulk substrates, which may differ in atomic constituents, unit cell parameters, and lattice periodicity. Assuming first for simplicity that the bulk and thin film share the same crystallographic axes, one can achieve a description of the total system's scattering by allowing the surface region in Equation (25) to encompass more than a single layer. Since multiple film layers are considered, we allow the lattice periodicity along the c direction to differ from that of the bulk substrate. The resulting expression is

$$I(\vec{q}) = \left| F_b(\vec{q}) \sum_{n_1, n_2=0}^{\infty} e^{i(n_1 q_a a + n_2 q_b b)} \sum_{n_3=1-(N_c-l_f)}^{-1} e^{i n_3 q_c c} + F_s(\vec{q}) \sum_{n_1, n_2=0}^{\infty} e^{i(p_1 n_1 q_a a + p_2 n_2 q_b b)} \sum_{n_3=0}^{l_f} e^{i p_3 n_3 c} \right|^2 \quad (26)$$

where p_3 is the relative c -axis periodicity of the film to the bulk, and the origin of the crystal has been moved to the interface between the bulk and film. An example applying the above expression for a film with different in and out-of-plane periodicities is shown in Figure 3. The expression in Equation (26) treats only a single-component film, which can be in- or out-of-registry with respect to the substrate. A film comprised of multiple layers of different atomic constituents and structures can be described in a similar way, by adding additional summation terms with unique structure factors and periodicities for each unique layer.

A crucial consideration in the analysis of thin films is the notion of coherent epitaxy. Depending on growth parameters such as the lattice mismatch between substrate and film, growth temperature, and film thickness, a deposited layer may be constrained to adopt the in-plane lattice of the substrate or it may relax its atomic positions. CTRs are useful tools in differentiating between coherently strained films and relaxed films, since the CTRs arising from the films should be commensurate with the substrate in the former case (i.e., p_2 and p_1 are whole numbers in Equation (26)).

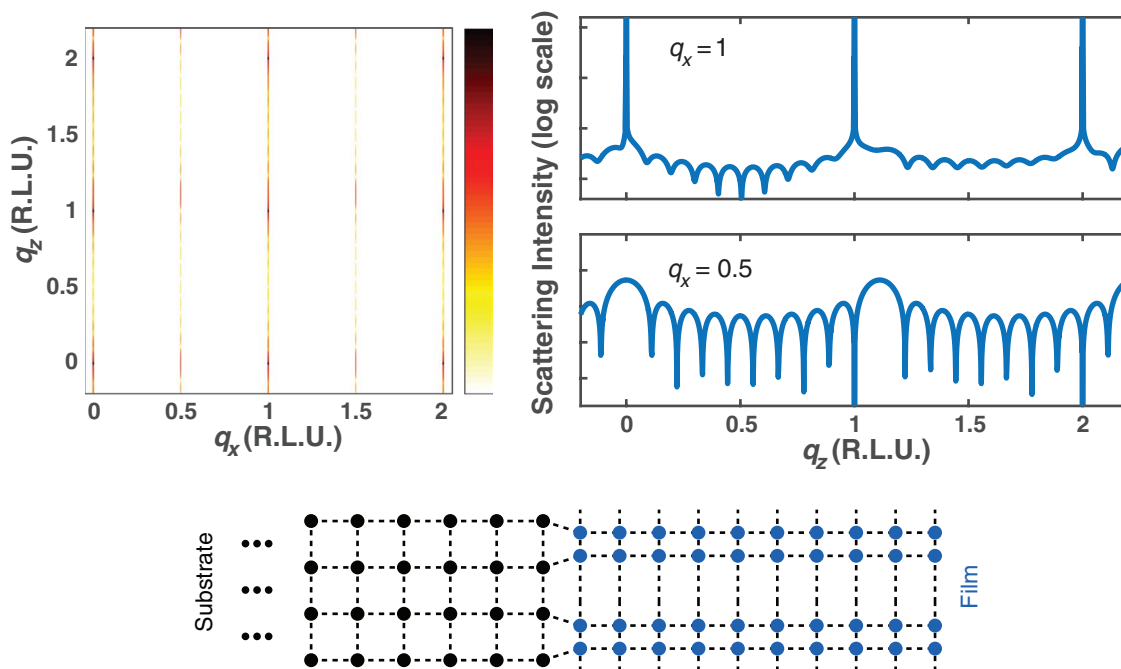


Figure 3. (Left) Reciprocal space map of an epitaxial film upon a half-infinite crystal from Equation (26). (Right) Line cuts showing the integer and half-order superstructure crystal truncation rods. (Bottom inset) Drawing of the simulated film, which is 10 layers thick with double the in-plane lattice constant and 90% of the c -axis lattice constant of the substrate.

2.4.3. Roughness

Another important factor in the analysis of interfaces and surfaces is roughness. A simple and useful model introduced by Robinson^[2] to describe the roughness of a crystal surface is to assume that layers near the surface can have a fractional occupation, β_n : $0 \leq \beta_n \leq 1$, which differs from layer to layer. The expression of the scattering intensity is an extension of Equation (21)

$$I(\vec{q}) = \left| F(\vec{q}) \sum_{n_1, n_2=0}^{\infty} e^{i(n_1 q_x a + n_2 q_y b)} \left(\sum_{n_3=1}^{N_c} e^{i n_3 q_z c} + \sum_{n_3=N_c+1}^{N_s} \beta_{n_3} e^{i n_3 q_z c} \right) \right|^2 \quad (27)$$

Here, we have disregarded relaxation and reconstruction effects and assumed that bulk unit cells occupy the surface at appropriate lattice positions, but with a distribution of site occupancies (fillings) along the c -axis. Taking N_c large, the first term in the parentheses gives the normal crystal truncation rod scattering from a semi-infinite crystal.

One can use Equation (27) to simulate the scattering from any desired roughness model. A common model posits a power law decay of the filling on the surface, such that the fractional occupation of the first surface layer is β , the fractional occupation of the second layer is β^2 , and so on. Then, in the sum in Equation (27), $\beta_{n_s} = \beta^{n_s - N_c}$. The sum can be evaluated in the limit of large n_s , which gives the result

$$I(\vec{q}) = \frac{(1 - \beta)^2}{1 + \beta^2 - 2\beta \cos(q_z c)} I_{\text{CTR}} \quad (28)$$

where I_{CTR} is the result of Equation (22).

The effect of the roughness parameter β is to reduce the intensity of the scattering between the Bragg peaks, while the intensity very close to the Bragg peak is largely unaffected. For larger β , the intensity at the anti-Bragg position is lowered and the intensity fall off as \vec{q} is moved away from the Bragg peak becomes steeper. The intensity reduction can be an order of magnitude or more for relatively rough surfaces ($\beta > 0.5$). One practical consequence is that minimal surface roughness is often a practical requirement to be able to observe the CTR intensity throughout an entire Brillouin zone in an experiment.

The interfacial roughness between a film and a substrate (or any two distinct layers) can be modeled in a way similar to that for the surface roughness formulated above. In particular, fractional occupations are given to each layer close to the interface containing contributions from both potential structures. Such considerations have become useful in the analysis of heterostructured, complex oxide interfaces in which polar discontinuities lead to electronic reconstructions at the interface (e.g., $\text{LaAlO}_3/\text{SrTiO}_3$ (001) and related polar interfaces). Roughness can alleviate or remove the effect of these discontinuities. Recent examples from the literature are highlighted in Section 3.3.

2.5. Experimental Measurement

We turn to some practical aspects of the measurement of crystal truncation rod scattering. In order to extract structural information about surface and interfacial structures from CTR measurements, one must be able to quantify the structure factor magnitude of the entire measured system $|F_{\text{meas}}(\vec{q})|$ accurately relative to that of the bulk substrate alone, $|F_{\text{bulk}}(\vec{q})|$. Then, one

can utilize the models described above and other methods for structure determination that are described in the next section.

The specific experimental techniques employed can vary greatly across the many research labs that carry out CTR measurements. In this section, we briefly discuss some of the common experimental requirements associated with these types of measurements.

2.5.1. X-Ray Sources and Optics

The source and detection requirements for CTR measurements can be understood by considering the simplified case of a truncated crystal (Equation (21)) with $|F(\vec{q})|=1$. Assuming a realistic absorption coefficient of $\mu^{-1} \approx 1\text{--}10\text{ }\mu\text{m}$ at hard X-ray wavelengths and a unit cell size of $c \approx 5\text{ }\text{\AA}$ one finds that the ratio of the intensity of the Bragg peak to the minimum of the CTR at the anti-Bragg point is $\approx 10^7\text{--}10^9$. Thus, one needs to be able to detect very low intensities (at the minimum of the CTR) with a large dynamic range (to access the full CTR information across the Brillouin zone).

In general, uncertainties are reduced and reconstructed atomic positions are more precise when a large region of reciprocal space is sampled. Several CTRs with different in-plane reciprocal lattice vectors are typically measured, and for each CTR, several Brillouin zones along the rod. The values of $|\vec{q}|$ accessible in an experiment are limited by the wavelength of the X-ray radiation, with the maximum value $|\vec{q}|_{\text{max}} = \frac{4\pi}{\lambda}$. As such, hard X-rays with X-ray wavelengths in the range $2\text{--}0.2\text{ }\text{\AA}$ (corresponding to energies in the range $5\text{--}50\text{ keV}$) are usually used.

Typical lab X-ray sources do not have sufficient spectral brightness to resolve details of CTRs at all desired scattering vectors for high-resolution experiments. Hence, CTR measurements were not experimentally widespread until the development of synchrotron X-ray radiation sources with many orders of magnitude higher brightness. High-resolution synchrotron-based CTR measurements are carried out at many beamlines worldwide.^[50–52] The key features of such beamlines are 1) high photon fluxes, 2) monochromatic hard X-ray beams, 3) goniometers with wide angular range, and 4) 2D area detectors. The current state-of-the-art undulator sources at synchrotrons have spectral brightness up to $10^{21}\text{ photons s}^{-1}\text{ mm}^{-2}\text{ mrad}^{-2}/0.1\%$ bandwidth, which experimentally enables extremely low-noise measurements of scattering features from even submonolayer structures.^[53]

Depending on the sample size and the desired angular resolution, a number of optical components may be used in the X-ray experiment. On the incident beam side, focusing optics or slits^[54] can be inserted after a single crystal monochromator^[55] and before the sample to achieve a small footprint on the sample. Incident beam cross-sections less than $1 \times 1\text{ mm}^2$ can be achieved without sacrificing significant incident intensity using Kirkpatrick–Baez focusing mirrors.^[56] For beam-sensitive samples, the balance between beam size and power density on the sample is an important consideration. For the diffracted beam, optics are chosen to improve the limited signal to background ratio in CTR measurements. Extrinsic background due to air scattering, especially at lower X-ray energies, and

scattering from environmental housings can be mitigated by placing a narrow slit on the detector arm as close to the sample as possible. When using 2D detectors (see Section 2.5.3), the scattering from the CTR should ideally occupy as much of the detector area as possible, which requires the detector be placed as far as practical from the sample. To reduce any background arising between the scatter slit and the detector, a beam tube filled with helium is often used. Radial collimators composed of multiple metallic blades can be placed in between the sample and detector to allow for measurements free of extrinsic background at small exit angles. A drawback of such a configuration, however, is that resulting intensity from the intrinsic sources of background (Compton scattering, thermal diffuse scattering, and fluorescence) may become nonuniform over the area of the detector.^[57–59]

2.5.2. Geometry and Sample Conditions

Experimental measurements of CTRs are carried out by measuring the diffracted intensity at various points in reciprocal space. As mentioned above and discussed in Section 2.6.4, the choice of the density and range of measured points is crucial for determining the structure with high resolution. The symmetry of the substrate/bulk determines the number of inequivalent CTRs. To obtain a full 3D reconstruction, rods at all inequivalent in-plane reciprocal lattice vectors $\vec{q}_{\parallel} = (H, K)$ should be measured (often, some equivalent rods are also measured to ensure accuracy). For a given (H, K) , the highest resolution can be obtained by measuring the full range of \vec{q}_{\perp} possible within the constraints of the X-ray wavelength and experimental geometry. The requirements for the density of measured points varies depending upon the thickness of the film/surface region and the complexity of the modeling to be used. As an empirical rule of thumb, a point spacing should be chosen so that the finite thickness and/or superlattice fringes are well resolved (typically with ≈ 10 points per fringe or more). Because of limitations on the dynamic range of the detectors and the dynamical diffraction effects, the regions of \vec{q} close to substrate Bragg peaks are typically omitted in CTR experiments.

Several geometries are used for angular movement and detection in X-ray diffraction experiments. For crystal truncation rods, one wishes to rotate the angles of the crystal axes and detector in such a way as to fix \vec{q}_{\parallel} and follow the scattering along the direction perpendicular to the surface normal. Goniometers most often used for CTR measurements have four to six circles—that is, angular degrees of freedom—associated with rotations of the sample and detector with respect to the incoming beam (an example is shown in **Figure 4**). These goniometers offer the flexibility to access a large angular range, while applying desired orientational constraints (fixed incident angle or exit angles, for example). For surface sensitive experiments, it is useful fix the incident angle when measuring a particular set of (nonspecular) CTRs, so that the penetration depth of the X-rays remains constant in the experiment. As discussed in Section 2.1.5, to enhance the measured diffraction intensity from the surface relative to the bulk, one common choice is to set the incident angle close to the critical angle for total external reflection.

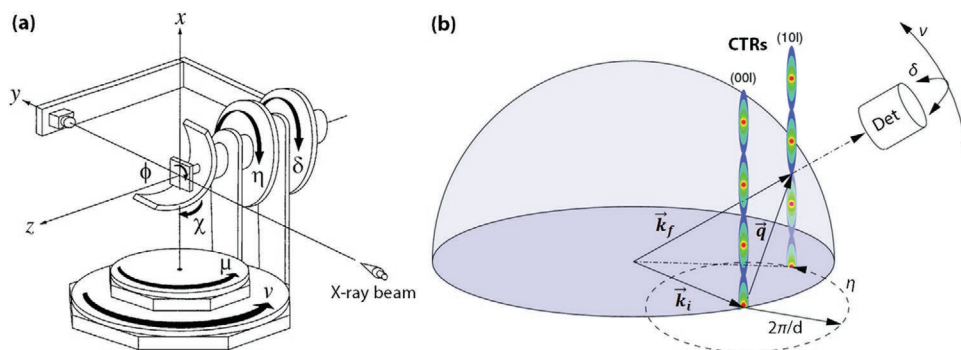


Figure 4. a) Schematic of a six-circle goniometer with four rotational degrees of freedom for the sample orientation and two for the detector, related to (μ, η, χ, ϕ) and (ν, δ) , respectively. The coordinates (x, y, z) represent the laboratory frame, where y is the direction of propagation of the incident X-ray beam. Reproduced with permission.^[60] Copyright 1999, International Union of Crystallography. b) Depiction of a CTR measurement. The scattering vector $\vec{q} = \vec{k}_f - \vec{k}_i$ is scanned along a CTR through the concerted motions of sample and detector angles. Reproduced with permission.^[61] Copyright 2016, International Union of Crystallography.

An important condition to avoid systematic errors is that the sample is positioned properly in the center of rotation (which also intersects the X-ray beam path) and its surface normal is aligned along the goniometer's azimuthal axis. For each type of goniometer, the relationship between the goniometer angles and the scattering vector can be calculated (see, e.g., refs. [58,60,62,63]). The angles can then be translated to the reciprocal lattice of the substrate crystal through the so-called orientation matrix, which is determined by finding the angles associated with two or more Bragg reflections.^[64]

Since CTR experiments do not require any special sample preparation or laboratory conditions, they lend themselves to studies in a variety of sample environments. For many studies of surfaces and thin films, samples can be directly mounted and measured under ambient conditions. Ideally, samples can be mounted inside a helium filled scattering chamber under a beryllium, Kapton, or (for high incident X-ray energies) aluminum dome. This configuration can lower extrinsic sources of background scattering through the use of a scatter slit, as discussed in Section 2.5.1. A chamber/dome must be used in the case of low temperature studies, where samples must be held in high vacuum in order to avoid ice formation. Examples of CTR experiments conducted in other types of environments, including in situ and in operando conditions, are discussed in Section 4.

2.5.3. Detection

To extract definite information about the surface structure factor, $|F_s(\vec{q})|$, one must measure the full intensity of the rod at each value of \vec{q}_\perp . The finite extent and divergence of the incident X-ray beam means that the diffraction peaks will have a corresponding width. Thus, one must ensure that sufficient transverse angular range $\Delta\vec{q}_\perp$ is detected so that the CTR intensity can be accurately measured. In early experiments with conventional point detectors, a common strategy for achieving this was to perform rocking scans with receiving slits large enough to capture all of the diffraction from the CTR as well as measure the background.^[57] Alternative methods that took advantage of special detector configurations were also

devised.^[65] These types of measurements suffer from long data acquisition times.

The advent of pixel-resolved area detectors in the 2000s accelerated the measurement of crystal truncation rods by simultaneously measuring the entire signal and background.^[59,61,66] Such detectors act as cameras that can resolve X-ray photons over a range of angles determined by the detector size, slit size, and the sample-detector distance. A typical modern area detector at a distance of 1 m from the sample could subtend several degrees in each direction with each pixel resolving $\approx 0.01^\circ$. Using such detectors, for a given scattering vector \vec{q}_\perp , the entire transverse range of diffracted CTR intensity can be imaged at once. In addition, background contributions from fluorescence or diffuse scattering can be identified and subtracted so that the absolute intensity associated with the CTR alone can be extracted (see Figure 5). Pixel area detectors are now standard devices used in most surface scattering experiments.

2.5.4. Corrections

In order to accurately compare a structural model or structure determination algorithm to an experimental intensity data set, various corrections must be made before evaluation. In particular, one must correct for, as a function of rotation angles,

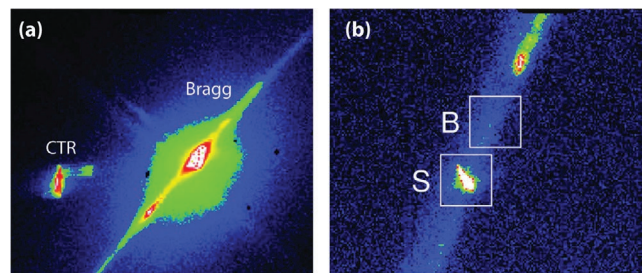


Figure 5. a) Typical image from a pixel area detector close to the Bragg condition. Both the CTR and substrate Bragg peaks are visible. b) Image showing a CTR (S) and background scattering from the sample holder (B), which can be subtracted from S to obtain the corrected signal intensity. Reproduced with permission.^[61] Copyright 2016, International Union of Crystallography.

the footprint of the beam on the sample, the detected spread in $\Delta\vec{q}$, and the polarization factor of the scattered wave.

The beam footprint correction arises from the fact that the projected area of the X-ray beam intercepted by the sample will change as a function of angle, and for very shallow angles, the beam will spill over the edge of the sample. This leads to a correction that scales with $\frac{W \sin \alpha}{h}$, where α is the incident angle, W is the length of the sample along the beam propagation direction, and h is the beam height. In nonspecular geometries, the azimuthal angle of the sample will additionally modify the beam footprint if the sample is not circular. Another correction comes from the fact that the detected region of the CTR along \vec{q}_\perp changes with angle due to the finite spread of the diffraction angle as well as the detector acceptance angle. The detected region becomes smaller for larger values of \vec{q}_\perp by the factor $1/\sin(\beta)$ in simple geometries, where β is the X-ray exit angle relative to the surface.^[58] The scattered intensity also depends on the polarization of the X-ray with respect to the scattering plane, as described in Equation (2). Depending on the X-ray source, the incident beams may be randomly, partially, or fully polarized, and the polarization factor must be calculated accordingly. These corrections can be measured or calculated for specific scattering geometries and beam shapes, and other corrections may be relevant for different experimental set-ups.^[58,61,67]

2.6. Structure Determination

The task of structure determination comprises the extraction of real-space information of atomic positions from a data set of crystal truncation rod intensities. The most basic information can be obtained from utilizing Bragg's law (Equation (20)). Averaged film and substrate lattice parameters are obtained from the measured angular positions of the substrate and film Bragg peaks. The intensities of the film Bragg peaks are significantly smaller than the substrate ones in most cases, and the peaks are usually visible only when the film thickness is large enough and/or when the lattice parameter of the film differs significantly from the bulk.

In this review, we focus on the use of CTR methods beyond characterizing thin film attributes such as thickness and lattice parameters. Below, we point out several of the more common techniques used for structure determination from CTRs which are capable of full atomic reconstruction of film, surface, and interface structures with high spatial resolution.

2.6.1. Model Refinement

The most straightforward and commonly used method for atomic structure determination is to compare X-ray scattering measurements to a structural model whose parameters can be varied and refined. Crystal structure refinement is a well-established discipline and many excellent resources concerning various aspects of its theory and implementation exist.^[68–70] Here, we only mention basic strategies and key aspects specific to its application to CTR analysis of thin films and interfaces.

Model Selection: For bulk crystals, the structural refinement procedure involves assuming a particular crystal symmetry (i.e., space group), lattice parameters, composition, and Debye–Waller factors for each atom within the unit cell. These features comprise the starting model whose X-ray scattering intensity $I_{\text{calc}}(\vec{q})$ can be calculated by Equation (13) and compared to those measured in an experiment $I_{\text{meas}}(\vec{q})$. One may then allow atomic coordinates and lattice parameters to vary until the agreement between I_{calc} and I_{meas} is optimized for the given model.

For an interfacial system, such as an epitaxial thin film, determining an appropriate starting model for structural refinement is a key challenge. Depending on the situation, any of the models discussed in Section 2.3 and extensions thereof may be appropriate. In the most general case, in which the atomic coordinates of each atom in all relevant layers (including film, surface, and interface layers) are to be determined, the number of free parameters can be large. As discussed in Section 2.4, for an epitaxial thin film, the lattice spacing and atomic positions in the direction normal to the interface can differ in each layer of the film. Relaxation and/or reconstructions of the in-plane unit cell can occur. Roughness and chemical intermixing at each interface (including the surface) might be taken into account, in addition to the usual Debye–Waller factors for each atom. Hence, it is crucial to constrain the parameter space and to pick a reasonable starting model so that a unique solution for the structure can be found conforming to given set of measurements.

Several strategies exist for choosing a starting model of an interfacial structure. In the simplest case, one might assume an atomic model in which the thin film retains the in-plane lattice structure of either its equivalent bulk compound or the substrate upon which it is grown. Such an assumption can often be justified if diffraction features arising from the film are observed along all measured substrate CTRs. This coincidence implies that the in-plane lattice of the film is coherent with the substrate. If superstructure rods are also observed, the in-plane scattering vector associated with them can be used to determine the periodicity of in-plane reconstructions of the film relative to the lattice. A unit cell of appropriate size can thus be chosen for the film. Alternatively, one may derive potential starting models from theoretical calculations, such as density functional theory, which can provide information on energetically favorable interfacial and surface reconstructions for the system under study. As discussed below, another possibility is to use the output of a direct phasing algorithm of the measured X-ray diffraction pattern to build an atomic model, which can then be refined. In Section 3, examples of experimental works that utilize all of these approaches are discussed.

Computation: Computationally, the problem of structural refinement is one of optimization in a large, multidimensional parameter space. The quantity to be minimized in the refinement is the so-called crystallographic *R*-factor

$$R = \frac{\sum |I_{\text{calc}} - I_{\text{meas}}|}{\sum |I_{\text{meas}}|} \quad (29)$$

In some fitting procedures, the magnitude of the structure factors, $|F_{\text{calc/meas}}| = \sqrt{I_{\text{calc/meas}}}$, or the log of the intensity may

be compared instead of the intensity, and statistical weighting factors may also be employed to account for measurement uncertainty. Many programs exist dedicated to the task of X-ray crystal structure refinement, making use of different types of optimization algorithms. Among those that are commonly used for crystal truncation rod analysis at present are ROD, GENX, and FIT.^[71,72] These and other tools provide useful features for fitting X-ray data of thin films and heterostructures, such as built-in atomic scattering factors, simple layer models, and means for simulating complex structures.

2.6.2. Direct Methods

The refinement method described above relies on having an accurate starting model of a structure under study containing all of the relevant degrees of freedom of the system. Taking advantage of the unique features of CTRs, a number of methods have been developed to reconstruct an atomic structure from X-ray diffraction data directly, without the need of a known structural model. These direct methods attempt to obtain both the magnitude $|E_c(\vec{q})|$ and phase $\phi_c(\vec{q})$ of the scattered X-ray field $E_c(\vec{q}) = |E_c(\vec{q})|e^{i\phi_c}$, which would allow direct Fourier inversion to obtain the electron density of the material via the relation

$$\rho(r) \propto \frac{1}{(2\pi)^3} \int_{\Omega} E_c(\vec{q}) e^{-i\vec{q} \cdot \vec{r}} d\vec{q} \quad (30)$$

where the integral is taken over all of reciprocal space. Such techniques are also known as phase-retrieval methods.

Direct methods in the purview of crystallography, and especially macromolecular crystallography, are plentiful and well-established. Here, we discuss only a few methods that are specifically designed for surface and interfacial structural determination using X-ray CTR measurements.

The direct methods developed for CTR scattering have fundamental underpinnings in the field of coherent diffraction imaging (CDI), which applies to structures having known constraints. For example, in certain descriptions of input-output methods for image reconstruction using CDI, the unknown image is assumed to be contained within a defined frame. When both the frame and unknown image are uniformly illuminated with coherent light, the phase of the resulting diffracted intensity can be recovered by applying the known constraints in an iterative fashion. The input–output process is applied in such a way that the error in the Fourier domain leads to a reduction of the error in the real space domain (Figure 6). In the context of CTRs, this approach is used for retrieving electron density of interface structures from measured CTR intensities, where the substrate and known film thickness serve as constraints that help recover the phase of the scattered X-rays. An in-depth and comprehensive discussion of the mathematics and history of direct phase retrieval methods can be found in Marks et al.,^[74] along with applications to surface electron diffraction.^[75–78]

For the specific case of thin films or surfaces, the constraints are taken as i) the known substrate electron density, $\rho_s(\vec{r})$; the spatial limits of the unknown surface region, $\rho_u(\vec{r})$, referred to as the support; and, the measured X-ray intensities $I(\vec{q}) = |T(\vec{q})|^2$, where $T(\vec{q})$ is the total scattering amplitude from the entire

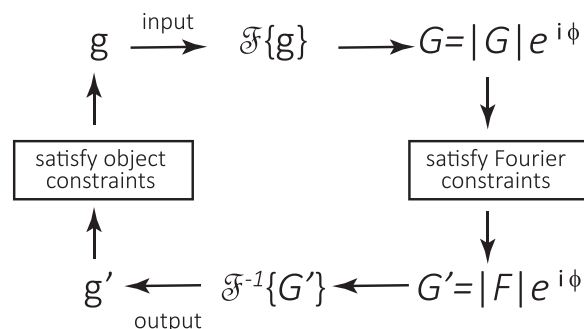


Figure 6. Schematic of process for direct methods. Reproduced with permission.^[73] Copyright 1978, Optical Society of America.

system. Thus, taking $S(\vec{q})$ and $U(\vec{q})$ as the scattering amplitudes for the substrate and surface region, respectively, the relation

$$|T(\vec{q})| = |S(\vec{q}) + U(\vec{q})| \quad (31)$$

must hold for all measured values of \vec{q} . The structure of the truncated substrate crystal is assumed to be completely known; hence, for all scattering vectors \vec{q} , the scattering amplitude (including phase) from the substrate, $S(\vec{q}) = W|S(\vec{q})|e^{i\phi_s(\vec{q})}$, is fully determined and in the best cases based on experimentally determined structure factors. One wishes to determine the scattering amplitude $U(\vec{q})$ from the surface region (including a thin film, for instance), which is unknown. Once determined, one can then retrieve the sought after surface electron density $\rho_u(\vec{r})$ by Fourier inversion of $U(\vec{q})$.

Different phase retrieval schemes may apply additional or modified versions of the constraints described above. They also differ in their optimization and initialization approaches. An initial guess of the phases can be made based on a trial (complex) film scattering amplitude, $U_0(\vec{q})$. This guess might be made based on electron microscopy data or knowledge of the expected film structure from theory. It is also possible to assume a uniform electron density with random phase in the constrained film region and proceed iteratively to derive the real phase and electron density.

Coherent Bragg Rod Analysis (COBRA): The COBRA method, originally developed by Yacoby and co-workers in 2000, relies on the epitaxial relationship between a substrate and an overlayer, for which the atomic structure is to be determined. It has been successfully used over the past several years to determine the complete electron density profile of a variety of complex interfacial systems, including epitaxial thin films, heterostructures, and quantum dots. We briefly sketch the main idea of the method here. More details can be found in refs. [79, 80].

From experiment, the intensities along substrate-defined CTRs are measured and one can rewrite the constraint of Equation (31) as

$$|T(\vec{q})|e^{i\phi_t} = S(\vec{q}) + U(\vec{q}) \quad (32)$$

For an adjacent point along the truncation rod separated by $\Delta\vec{q}$, the same relation must hold. The COBRA method makes the assumption that the phase of $U(\vec{q})$ changes slowly relative to the phase of $S(\vec{q})$, which is valid in the case that the thickness

of the unknown region is small. Then, one can approximate $U(\vec{q} + \Delta\vec{q}) \approx U(\vec{q})$, so that

$$|T(\vec{q} + \Delta\vec{q})| e^{i\phi_2} = S(\vec{q} + \Delta\vec{q}) + U(\vec{q}) \quad (33)$$

Solving Equations (32) and (33) for each pair of measured points provides two solutions for $U(\vec{q})$ as well as the phases ϕ_1 and ϕ_2 . COBRA selects the set of solutions which varies least along the CTR.

In practice, the reference structure may be taken as an initial model of the substrate and film under study. The COBRA procedure then solves for $U(\vec{q})$ and a compatible total scattering amplitude $T_c(\vec{q})$, which can be compared to the measured CTR intensities $I(\vec{q})$. One can then iteratively update the reference structure with the Fourier transform of $T_c(\vec{q})$ and continue the process until convergence of the R -factor (Equation (29)) with $I_{\text{calc}} = |T_c|^2$. Generally, COBRA requires few iterations to reach convergence.

Fourier inversion of the converged $T_c(\vec{q})$ provides an electron density map $\rho(\vec{r})$ of the system with in-plane periodicity defined by the substrate. As discussed in Section 3, analysis of the electron density map can provide picometer-scale structural information on the film as well as the film-substrate interface. Moreover, from the electron densities, the elemental composition can be gleaned as a function of space, from which processes like intermixing between layers and surface segregation of atoms can be identified. This capability mirrors the ability to identify elemental composition using Z -contrast TEM imaging. An example of an electron density map in which both atomic composition and positions may be determined is shown in Figure 7.

Phase and Amplitude Recovery and Diffraction Image Generation Method (PARADIGM): The PARADIGM was originally developed by Saldin and co-workers in 2001. Also building off of a known reference structure and measured CTRs, the algorithm relies on a combination of constraints in real and reciprocal space to iteratively improve an estimation of the electron density of an unknown region (i.e., surface, interface, or film). An advantage of the method is the ability to handle surface structures with different in-plane periodicity from the bulk, and consequently, it has been particularly useful for determining reconstructions of surfaces and sub-monolayer epitaxial films.

One begins with a starting estimate of the unknown electron density film/surface region, $\rho_U^{(n)}(\vec{r})$, and the known scattering amplitude of substrate, $S(\vec{q})$. The algorithm proceeds as follows:

1. The Fourier transform of $\rho_U^{(n)}(\vec{r})$ is taken to obtain an estimate of the scattering amplitude of the unknown region, $U^{(n)}(\vec{q})$.
2. An estimate of the total scattering amplitude is computed by the sum of the unknown and reference scattering amplitudes, $T^{(n)}(\vec{q}) = S(\vec{q}) + U^{(n)}(\vec{q})$, and the phase $\phi_r^{(n)}(\vec{q})$ is determined.
3. A new estimate of the unknown scattering amplitude is computed, $U_b^{(n)}(\vec{q}) = c^{(n)} |T(\vec{q})| e^{i\phi_r^{(n)}} - S(\vec{q})$, where $c^{(n)} = \frac{\sum |T(\vec{q})| |T^{(n)}(\vec{q})|}{\sum I(\vec{q})}$ is a weighting factor.
4. The Fourier transform of $U_b^{(n)}$ gives a new estimate of the electron density of the unknown region $\rho_b^{(n)}$.
5. A support constraint in real-space is applied such that $\rho_U^{(n+1)} = \rho_b^{(n)}$ only in regions where electron density is expected to exist (i.e., thickness of film) and $\rho_U^{(n+1)} = 0$ elsewhere.

The algorithm is then repeated from step (i) with the new electron density $\rho_U^{(n+1)}$ and the procedure above is continued until convergence of, for instance, the R -factor (Equation (29)) or the electron density. The constraint imposed in the last step of the algorithm is one of many possible so-called object domain operations that conditions the data in real space. Other possible constraints are those that enforce positivity or atomicity of the electron density.^[82] From a signal processing viewpoint, one may apply certain real-space constraints as long as the scattering intensity of unknown surface region is oversampled relative to the expected smallest relevant q spacing (related to the inverse of the thickness of the unknown region).

The algorithm can take advantage of information from both CTR and superstructure rods, thus allowing the reconstructed electron density to contain periodicities different from the substrate. In addition, the algorithm can be extended to handle materials with different domains within the probing area of the X-ray, which are otherwise difficult to disentangle since they contribute incoherently to the measured intensities. Notably, the method has been applied to characterize the full 3D, reconstructed and relaxed structure of the Au (110) surface as well as submonolayer Sb/Au (110).^[83] More recently, the approach has been used in

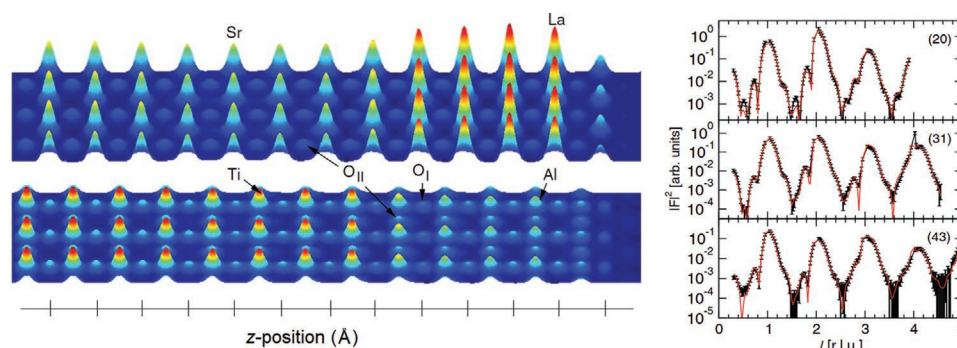


Figure 7. Example of an electron density map output from COBRA, here for the case of a LaAlO_3 film on SrTiO_3 . The top and bottom panels show two different cuts in the x - z plane. Elements can be identified by their relative electron densities. Reproduced with permission.^[81] Copyright 2007, American Physical Society.

combination with others to shed light on topological insulator surfaces and thin films,^[84,85] which is detailed in Section 3.

Difference Map Using the Constraints of Atomicity and Film Shift (DCAF): The final direct method that we discuss here is known as the DCAF, developed in 2008 by Björck and co-workers. As with PARADIGM, this method iteratively applies constraints to converge to a solution for the electron density satisfying certain requirements and consistent with measured scattering data. To do so, it uses a difference map algorithm devised by Elser,^[86–88] which has the key property that the generated solution robustly tends toward the global optimum (rather than a local optimum).

The algorithm formulates the constraints as projections of the unknown surface-region electron density (ρ). Each projection maps an input ρ onto a subspace that fulfills the constraint. We write the projection associated with the real space object domain operations as \hat{P}_R and the reciprocal space constraint of matching measured scattering intensities as \hat{P}_F . In DCAF, the real space operations are threefolds: 1) ρ must be positive; 2) ρ must be composed of atoms of a certain finite extent; and 3) ρ must fill all of the unknown region. The last projection, known as the film shift projection, is unique—it is related to the support constraint of a finite film thickness, but instead of eliminating ρ outside the film region, this operation moves the origin of the unknown region to include bulk unit cells. The difference map is then written as follows

$$\rho_{n+1} = \rho_n + 2\hat{P}_R\hat{P}_F\rho_n - \hat{P}_R\rho_n - \hat{P}_F\rho_n \quad (34)$$

where n represents the current iteration. The difference map error

$$\epsilon_{n+1} = \|\rho_{n+1} - \rho_n\| \quad (35)$$

tracks the convergence of the solution, which ideally reaches zero when a solution is obtained.

Initial results appear to show that the combination of constraints used in DCAF provides consistent and reproducible results, regardless of the random initial phases given to start the algorithm. This feature overcomes a shortcoming of COBRA, which shows some dependence in its final solution on the initial guess for the film structure. Recently, DCAF has been used to perform complete structural analyses of complex oxide heteroepitaxial systems, such as $\text{LaAlO}_3/\text{SrTiO}_3$ and thin films of superconducting $\text{YBa}_2\text{Cu}_3\text{O}_{7-x}$. Some of these cases are highlighted in Section 3.

2.6.3. Hybrid Methods

The direct methods discussed above can provide accurate reconstructions of the real-space electron density from the diffraction data. Often, these outputs are used in conjunction with model refinement procedures to allow for more precise determination of atomic positions. A structural model is built from the direct phasing algorithm by fitting the electron associated with each atom in the output electron density map. This structure is then used as the initial model for structural refinement. This type of hybrid method provides the advantages of parameter

optimization via refinement with a bias-free initial structural model determined by the phase-retrieval methods. As such, hybrid phase retrieval + refinement methods have become the standard bearer for high-resolution interfacial structure determination from CTR scattering.

2.6.4. Resolution, Uncertainty, and Limitations

In order to attain a desired resolution for the real-space structure, the appropriate data sampling in reciprocal space must be chosen. Roughly, in terms of the unit cell spacing of the bulk or substrate d and the measured range of L (in R.L.U.) along a rod, the resolution is given by $r_{\min} \approx \frac{d}{2L_{\max}}$, which represents the distance between reconstructed points in real space. A typical measurement might have $L_{\max} = 5$ and $d \approx 4$ Å, which would give a resolution of ≈ 0.4 Å. By interpolation of the electron density and/or subsequent refinement, the ultimate resolution of the determined structure is typically much smaller than r_{\min} . Similarly, the spacing of data points in reciprocal space Δq must in general be small enough so that the corresponding real-space extent $r_{\max} \approx \frac{2\pi}{\Delta q}$ is much larger than unknown film or surface region to be retrieved. This oversampling condition allows for the application of the support constraints used in the phase retrieval algorithms described above.^[79,89,90] Analogous conditions apply when model refinement alone is employed, wherein the number of measured points should be much larger than the number of degrees of freedom of the model. The resolution in this case is limited by the accuracy of the chosen model and the goodness of the fit, as determined by the R -factor (or variant thereof).^[91]

Determining the uncertainty of the structural determination is an important factor for assessing the reliability of the information extracted from CTR measurements. When fitting experimental data to a parameterized model, one can statistically estimate the error in the refined parameters, such as the atomic positions and occupancies for each layer of a film or heterostructure. An error estimate can be obtained by varying each model parameter until the calculated R -factor deviates from the optimal R -factor by a designated amount.^[72] For example, the range of values corresponding to a 5% variation of the R -factor would provide a confidence interval of two standard deviations for that model parameter. More sophisticated methods may also be used to calculate uncertainty, taking into account the correlations between parameters and systematic errors, for example.^[70,92]

When using direct methods, structural parameters are extracted from the retrieved electron density maps (for example, by fitting the electron density around an atom or taking its centroid to determine its position). Some of the algorithms discussed above can be initialized with random phases for the unknown scattering amplitude. In these cases, the uncertainty can be estimated from the distribution of electron densities acquired for different trial runs (i.e., with different random phase initializations).^[89] An alternative procedure was developed based on comparing electron density maps with simulated experimental noise, which can be applied when random phase initialization is not possible and/or desirable.^[29] It was also

shown that a rough estimate of the accuracy of the retrieved electron density of a surface or thin film may be obtained by including several bulk/substrate unit cells in the analysis and comparing the reconstructed structure deep into the bulk with that of the known structure.^[93]

A survey of recent high-resolution CTR results using model refinement, direct methods, and hybrid approaches shows that the estimated uncertainty in the relative atomic positions (along the surface normal) is generally less than 0.1 Å (10 pm), the uncertainty in the occupancies is on the order of $\approx 5\text{--}10\%$, and bond/tilt angles can be determined with a precision a few degrees.^[1,31,93–100]

It should be noted that, for a full reconstruction of the electron density from CTR data, it is challenging to apply current phase retrieval techniques for more than $\approx 10\text{--}15$ unknown surface or film layers. Therefore, the application of direct methods has been restricted to surface and thin film structures, while larger structures such as periodic superlattices have been analyzed via model refinement.

3. Applications

In this section, we highlight several applications of crystal truncation rod scattering. Since the first experiments measuring CTRs, hundreds of studies have been performed that use the technique in one form or another. We provide an account of some relevant works, restricting ourselves mainly to the subset of experimental studies which used CTR scattering for comprehensive layer-resolved structure determination of a surface or interface.

More detailed discussions in this section focus on relatively recent experiments concerning heteroepitaxial interfaces. In particular, a significant portion of recent CTR experiments relate to the control of complex oxide interfaces and oxide-semiconductor interfaces. Our review follows in large part research developments in this field. We also connect the highlighted research to the broader goals and understanding of picoscale structural manipulation of materials.

3.1. Surface Structures

3.1.1. Metal and Semiconductor Surfaces

Some of the important experiments measuring CTRs from metal and semiconductor surfaces are mentioned in Section 1.1, as much of the work in the 1980s and 1990s focused on these systems for electronic and catalytic applications. The structure and roughness of bare and treated surfaces of technologically important semiconductors were discovered in these works. In such studies, CTR and surface X-ray diffraction play equally important roles, allowing in-plane and out-of-plane structure as well as surface roughness to be determined. Among the most studied systems were the Si (111) and Ge (111) surfaces.^[4–8] Also, simple metal surfaces (such as various terminations of Au, Ag, Pt, and Cu) as well as compound metal surfaces (including Cu_3Au and NiAl) were examined in detail in order to experimentally test elastic, chemical, and thermodynamic models of surface structures.

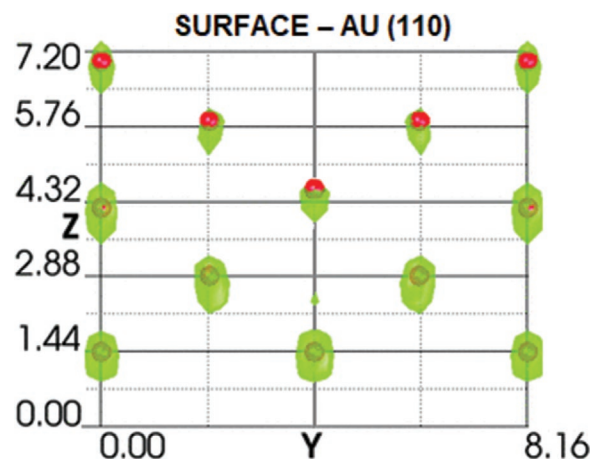


Figure 8. Projected electron density map showing the structure of the first few layers of the Au (110) surface. Isosurfaces of the electron density are shown in green and the atomic positions from refinement using starting positions from PARADIGM are shown as red balls. Both the (2×1) reconstruction of the surface layer and the buckling of the subsurface layer relative to the bulk lattice positions (solid lines) can be observed. Reproduced with permission.^[90] Copyright 2005, American Physical Society.

A more recent study of metal surfaces used the Au(110) surface as a test ground for the PARADIGM phase-retrieval method.^[90] Both bulk and superstructure truncation rods served as inputs to PARADIGM, which could reconstruct a 3D model of the near surface layers. The previously observed (2×1) reconstruction was reproduced, but in addition, a subsurface buckling was directly observed, which was not seen by earlier surface X-ray diffraction work. The electron density map extracted from PARADIGM as well as the subsequent refined surface structure are shown in Figure 8.

3.1.2. Oxide Surfaces

Oxides historically provided a challenge for CTR experiments due to the low atomic scattering factor of oxygen and the difficulty in preparing atomically flat surfaces. As oxides are often used as catalysts in heterogeneous oxidation/reduction reactions, understanding the structure of their surfaces is technologically relevant. Moreover, many oxides serve as substrates for the thin film growth of a great variety of interesting materials, such as high-temperature superconductors. As described in Section 3.3, the physical structure of the substrate is crucial for determining the electronic properties of films—especially ultrathin (i.e., < 5 nm thick) films—grown upon them. Standard electron diffraction techniques for surfaces are often hindered by charging effects due to the insulating and/or polar nature of the surfaces. Thus, CTRs have been crucial in uncovering the surface structures of oxide materials.

After the initial experiments of Andrews and co-workers mentioned in Section 1.1, one of the first meaningful CTR experiments on oxide surfaces studied single crystals of the high-temperature superconducting compound $\text{YBa}_2\text{Cu}_3\text{O}_{7-\delta}$ (YBCO).^[101] Due to the layered nature of its unit cell, along its growth direction YBCO has six possible surface terminations. This study sought to determine the growth termination plane

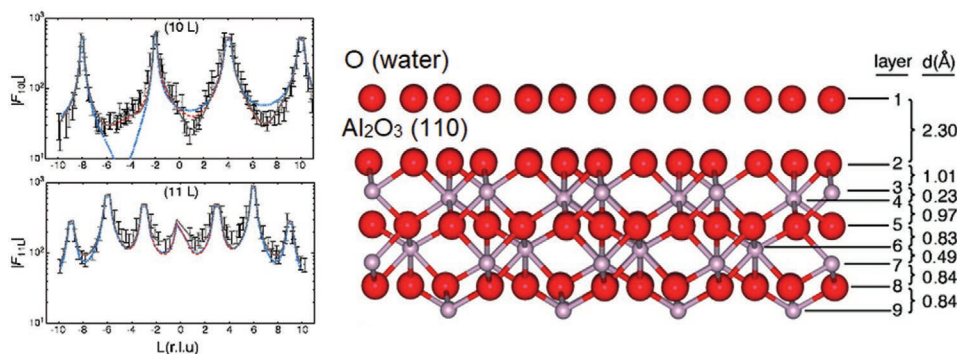


Figure 9. (Left) Example CTRs and fits using (blue dotted) ideal oxygen termination, (red dashed) relaxed surface, and (black solid) relaxed surface with oxygen overlayer representing adsorbed water. The overlayer is needed to properly fit all CTRs. (Right) Best fit structure including the overlayer, showing picometer-scale distortions. Reproduced with permission.^[112] Copyright 2000, AAAS.

by measuring two different CTRs over a very large range of q_{\perp} (or L). A primarily Y-terminated surface was found to fit the data well, and the experiment showed the feasibility of using CTRs to accurately discriminate between different surface terminations of oxide materials. Local probes such as STM require pristine surfaces and typically must be performed in situ to accurately determine surface termination, so CTR scattering offers an advantage in this regard, if sufficient accuracy can be obtained.

TiO₂: The surface of TiO₂ has been used as a model system in surface science over the past few decades and has been heavily studied due to its appeal for catalysis and optical applications.^[102] Charlton et al. provided an important early experimental measurement of the out-of-plane relaxations of rutile TiO₂ (110)–1×1 surfaces using CTR scattering and model refinement.^[103] They measured five CTRs, each up to values of $L = 5$, and found a characteristic rumpling of the surface titanium planes, with the direction and magnitude of the Ti displacement relative to the bulk dictated by the oxygen coordination of the Ti ion. Interestingly, the same group found that a submonolayer-thick Cu overlayer seems to remove the Ti displacements.^[104] However, the bare surface model of ref. [103] conflicted with later low-energy electron diffraction^[105] and ion scattering^[106] studies, in particular with the position of the oxygen bridging the top two planes. It appears that recent CTR measurements and re-analyses^[107,108] resolved the discrepancy, corroborating the later measurements. A 2 × 1 reconstruction of the rutile TiO₂ surface also exists, and CTR studies found that it behaves similarly to the (001) surface.^[109,110] The structural results provide an important benchmark for ab initio calculations, which are extensively used in the study of chemical reactions involving rutile TiO₂ surfaces.

MgO: The MgO (001) surface is another that has attracted much attention since the early 2000s, largely due to its use as an inert and stable substrate. Some of the attraction might be attributed to the availability of an experimentally determined structural model of the clean surface, which was determined by CTR scattering to have a $\sqrt{2} \times \sqrt{2}$ reconstruction and <1% of relaxation and rumpling distortions.^[111] The CTR data determined structural deviations with a precision on the order of 1 pm, which was the highest experimental precision at the time.

Al₂O₃: The surfaces of Al₂O₃ have been studied for use as a thin film growth substrate and as a model for geochemical processes. The bare (0001) surface was found to have a single Al termination with large oscillatory relaxations as a function of depth, agreeing with theoretical predictions. As Al₂O₃ is often utilized in aqueous conditions, Eng et al. compared the bare surface structure prepared under vacuum with that of a hydrated surface.^[112] The surface model of hydrated Al₂O₃ (0001) determined from CTR measurements found an oxygen terminated surface and a significant contraction of the double Al layer just below the surface. A useful observation from this work is that fitting the measured CTRs requires inclusion of an extra oxygen overlayer above the crystal surface (see Figure 9). This layer represents the influence of adsorbed water. To affect the CTR scattering profile, the adsorbed layer must be at least partially ordered.

A similar comparison of bare and hydrated conditions was carried out for the Al₂O₃ ($\bar{1}\bar{1}02$) surface, which has a different coordination of Al ions.^[113] On this surface, a model with an oxygen-terminated surface, but without Al in the second layer, fit the data best, with no inclusion of an adsorbed overlayer necessary. Instead, it is presumed that hydroxyl groups would exist at available bonding sites on the surface. These experiments demonstrate the sensitivity of CTR scattering to the surface environment and show that the technique can be used to look at ordering of adsorbed layers.

SrTiO₃: SrTiO₃ is one of the most widely used substrates for epitaxial growth of complex oxide materials, which are discussed in Section 3.3. Consequently, its surface structure has been the subject of much study in order to shed light on growth mechanisms and interfacial characteristics of epitaxial thin films. The first crystal truncation rod measurements reported in 2000 considered the (1 × 1) surface of SrTiO₃ (001) and fit data to a model with a mixed SrO and TiO₂ termination.^[114] The results most notably found no relaxation of surface Ti for the TiO₂ termination, which was consistent with earlier ion scattering data, but disagreed with density functional theory calculations. It became clear from a plethora of experimental and theoretical studies that the manner in which the surface was prepared dictated, in large part, the surface structure.

In 2007, Herger et al. used CTR measurements to solve the structure of the SrTiO₃ (001) surface that had been processed

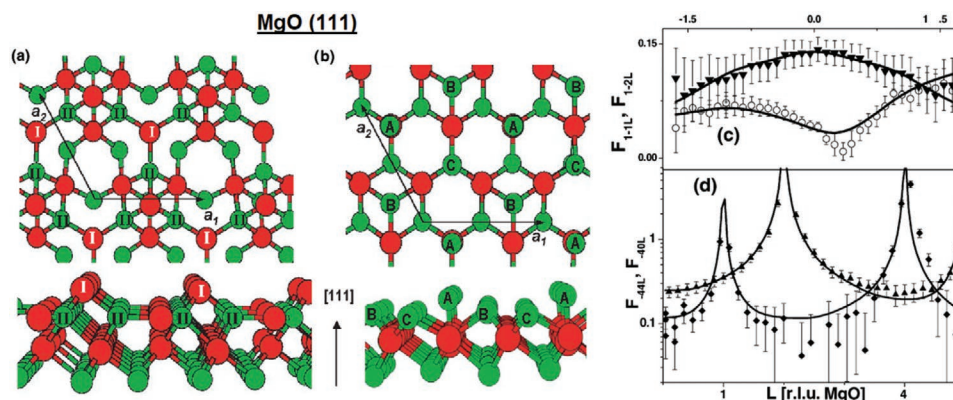


Figure 10. a) Top and side views of the (2×2) O-terminated octopolar reconstruction and b) an alternative (2×2) Mg-rich surface reconstruction of the MgO (111) surface. Oxygen is displayed in red and Mg in green. c,d) Experimental CTR measurements (symbols) along with fits (solid lines) assuming a mixed occupation of the surface reconstructions from (a) and (b). Reproduced with permission.^[119] Copyright 2004, American Physical Society.

using a widely used method to achieve complete TiO_2 termination.^[115,116] From a structural refinement, they found that the surface exhibits a mixture of (1×1) domains with (2×1) and (2×2) reconstructions. Most significantly, their model requires a double TiO_2 termination, that is an extra, bulk-like TiO_2 layer immediately below the surface. Importantly, in their structural refinement, they tested many models that had been proposed for the TiO_2 surface and used electron densities determined directly from the PARADIGM phase-retrieval algorithm to corroborate the existence of a double TiO_2 layer. When the surface was heated in vacuum to simulate typical epitaxial growth conditions, their analysis revealed that only the (1×1) surface is present, but the double TiO_2 termination remains. These results have significant implications in the context of emergent interfacial phenomena in oxide systems (see, for instance, Section 3.3.4).

Polar Surfaces: Some of the most widely studied surface structures are those terminating polar crystal planes. For these surfaces, the layers along the surface normal carry alternating formal charge, leading to an electric potential that grows with the number of layers. For a bulk crystal, the potential diverges. To compensate, such surfaces are subject to a variety of reconstructions and relaxations, the determination of which bears significant fundamental and practical interest since many common oxide substrate/catalyst terminations lead to polar surfaces. We refer the reader to seminal reviews by Noguera^[117] and Henrich and Cox^[118] for a more thorough discussion of the subject.

CTR scattering has helped to determine the structure of several relevant polar surfaces and shed light on new stabilization mechanisms. For example, for the polar (111) surface of rocksalt-type oxides, an octopolar surface reconstruction proposed by Wolf^[120] for NaCl (111) was thought to alleviate the polar instability. The reconstruction consists of a (2×2) surface with 25% occupation of the topmost layer and 75% occupation of the subsurface layer. In NiO (111), observations of (2×2) surface structures by low-energy electron diffraction were attributed to the octopolar reconstruction, while results on MgO (111) appeared to conflict with this model. CTR investigations on these surfaces were carried out in different thermodynamic environments^[119,121,122] and found that the

octopolar reconstruction only appears under certain conditions. By fitting to models and comparing with theory, it was found that the type of termination layer (O or metal) depends on the annealing temperature and pressure, and other (2×2) configurations may coexist with the octopolar reconstruction—in particular metal-rich surface structures under reducing conditions (see Figure 10). The discovered surface structures challenge simple models of the polar reconstruction, and impact their reactivity as well as their suitability as epitaxial substrates.

In the case of the polar ZnO (0001) surface, conflicting accounts of the surface structures measured by CTR scattering have been reported. This crystal cut leads to Zn- and O-terminations on opposite crystal faces. Wander et al.^[123] performed model fitting of CTR profiles to establish that the O-terminated surface does not reconstruct and only experiences relaxations along the surface normal. The stabilization mechanism, suggested by first-principles theory, instead consists of an electron transfer between the two surfaces, which creates metallic surface states. Schlepütz et al., on the other hand, found a (1×1) oxygen overlayer on the Zn-terminated surface with no significant relaxations, even in cases where metal/metal-oxide contacts were deposited.^[124] The discrepancy may be related to the different preparation methods or the different terminations studied, but identifying the presence of metallic surface layers has important consequences for electronic applications of these crystals.

Oxide substrates used in the epitaxial growth of functional materials are commonly chosen based on lattice matching. In some cases, the appropriate substrate is polar along the relevant growth direction. Both the terminating layer and any compensating surface structures are important to identify in order to optimize epitaxy. Two common oxide substrates with polar surfaces, LaAlO_3 (001) and DyScO_3 (110), have been studied by CTR scattering in order to understand the surface under growth conditions.^[125,126] For LaAlO_3 , CTR fitting determined that the surface is AlO_2 -terminated from room temperature up to high temperature (670 K), with no lateral reconstruction reported but with a temperature-dependent buckling of the surface oxygen atoms. For DyScO_3 , when the surface is prepared by selective etching, an almost fully occupied (1×1) ScO_2 -terminated surface is achieved, as determined by CTR

fitting and confirmed by electron diffraction and mass spectroscopy. In both cases, the observed surface structures do not compensate the polarity; thus, it is likely that extrinsic factors, such as adsorbates or surface oxygen vacancies, which were not detected, play a decisive role.

3.2. Metal and Semiconductor Interfaces

We turn our focus to applications of CTR scattering in heteroepitaxial systems. These studies concern the structural and chemical modifications that occur at the interface between a film and a substrate and throughout a film during and after its growth. Some of the many experiments that have been carried out on metal and semiconductor interfaces are first briefly presented.

3.2.1. Epitaxial Films on Si

Robinson, Tung, and Feidenhans'l carried out one of the first CTR studies of a heteroepitaxial film, analyzing the interface between NiSi_2 and Si (111).^[127] Owing to the crystals' well-matched lattices, this system provides a clean model interface. In addition, the lattice match means the respective Bragg peaks for the film and substrate are nearly identical, enhancing the interference in the scattered intensity. They used a simple kinematic model (as in Section 2.3) to fit the CTR around the (111) Bragg peak, from which they were able to extract the slight deviations in the out-of-plane spacing between the film, the substrate, and the interface with a precision of $<0.5\%$ or ≈ 1 pm. This experiment demonstrated that the interference between film and substrate in CTRs allowed for precise determination of interfacial structure and compared favorably with the most sensitive surface probes at the time.

Since this work, a number of interfacial structures of metallic and semiconducting films on Si have been studied using similar methods. Some of the relevant systems include Cu,^[128] Ag,^[129,130] CaF_2 ,^[131,132] Ge,^[133] AlN,^[134] FeSi,^[135] on Si (111); GaAs,^[136] amorphous-Si/Ge layers,^[137] and Ge quantum dots on Si (100)^[94,138]; and, quantum wires of Au on Si (557).^[139] It is worth mentioning that, among these, the studies by Walker et al.^[128] and Tweet et al.^[140] were among the first to use anomalous CTR scattering to identify the energy-dependent scattering from specific surface species as a means to extract atomic positions in an interfacial system. Recently, Shirasawa and colleagues have studied in situ grown heterostructures of Bi,^[141] Bi/ Bi_2Te_3 , and Cu-doped Bi_2Te_3 on Si (111) by CTR scattering.^[84,85,141] These structures are variants of topological insulators, which are a class of materials that have generated much interest due to their symmetry-protected surface states and other unique electronic properties.

3.2.2. III–V Heterostructures

Starting with the work of Lucas et al. in 1998 on GaAs/InAlAs/InP,^[142] a number of experiments using techniques related to CTR scattering have been used to study growth processes in III–V heterostructures. A majority of such works used

conventional thin film diffraction and CTR-like methods to characterize lattice parameters and roughness of various types of heterostructures grown under different conditions (primarily using vapor phase deposition).^[143–153]

The initial application of the COBRA algorithm by Yacoby and co-workers^[79] pertained to the AlAs/GaAs (001) interface, and several early applications focused on other III–V hetero-interfaces, including InAs/GaSb (001)^[154] and GaAs/InGaAs/InP (001).^[155] Moreover, CTR scattering has been extensively used to study the structure and composition of III–V nanostructures and quantum dots.^[156,157] From COBRA analysis, the composition profile as well as the shape of dots could be extracted, providing important insights into dot formation and interdiffusion.^[158–160]

3.3. Oxide Interfaces

The large body of literature using CTR techniques to study oxide interfaces as well as oxide–semiconductor interfaces is highlighted in detail. Over the past 10–15 years, the study of the functional properties of complex oxide thin films, heterostructures and interfaces has burgeoned. The discovery of emergent properties nonexistent in bulk form and the potential for new technologies exploiting this behavior have fueled the quest to understand, harness, and engineer oxide interfaces. It has generally been understood that the versatility of complex oxides stems from a strong coupling of electronic/magnetic and structural degrees of freedom. Most of the research has centered on transition metal oxides, in which the coupling is related to the fact that that bonding between transition metal d and oxygen p orbitals controls electronic structure at the relevant energy scales. The atomic structure, which in large part dictates the bonding between atoms, is thus a crucial factor in determining the resulting electronic and magnetic properties.

These arguments are especially relevant at the epitaxial interfaces between oxides, since large structural deformations away from bulk structures may occur. When probing ultrathin layers, the effect at the interface can dominate the observed properties. Hence, interfacial structure determination in composite oxide systems has been a driving force in the discovery, understanding, and control of their interesting functional properties. Exploiting interfacial mechanisms for specific functional behavior is a cornerstone of the emerging field of picoscale engineering.

High-resolution structural determinations using CTRs have helped identify and elucidate paradigms for understanding the behavior of complex oxide films and heterostructures, including the influence of polarization discontinuities and octahedral connectivity. In the following, we consider a number of oxide thin film and heterostructure systems, in which CTR scattering plays a significant role in elucidating and/or engineering the electronic or magnetic behavior. We pay particular attention to modern experiments that utilize CTRs for complete interfacial structural determination. Especially in cases where direct methods are used, the full utility of CTR experiments can be appreciated.

As a starting point for understanding, most of the systems discussed below share a similar perovskite-like structure, with

an ABO_3 chemical formula, as shown in Figure 11a. The ideal perovskite structure is cubic, and the functional unit is a BO_6 octahedron. It is often useful to describe the structure of materials in this class as a deformed perovskite with a superstructure of octahedral tilts and/or rotations. More detailed discussions for specific materials are categorized according to their functionalities in the remainder of this section.

3.3.1. Ferroelectrics

Two of the most studied ferroelectrics are the oxides BaTiO_3 and PbTiO_3 . They display prototypical ferroelectric behavior, and the alloyed version of these compounds, $(\text{Ba,Sr})\text{TiO}_3$ and $(\text{Pb,Zr})\text{TiO}_3$, are used in commercial ferroelectric memories.^[161] It was shown that the ferroelectric properties of these compounds are affected significantly when they are grown in ultrathin layers; most notably, the ferroelectric polarization is reduced or

suppressed entirely due to the depolarization field.^[162,163] At the same time, the mechanical and electrical boundary conditions imposed by the substrate and any electrodes may enhance or weaken the ferroelectric polarization.^[164] Ferroelectrics also readily form domain structures that may be influenced by the interface. The polarization of the ferroelectric film manifests in the relative out-of-plane displacements of the cations and oxygen anions in the unit cell, and thus it can be probed structurally via X-rays and CTR scattering. Thompson and co-workers showed that the polarization direction of a ferroelectric film can be determined from the CTR profile arising from the interference of the film and substrate scattering.^[165] An isolated ferroelectric would show no such change in shape due to the symmetry of two polarization directions.

The first measurements of the interfacial structure of ferroelectric films, shown in Figure 11, were carried out by Fong et al.^[166] They studied PbTiO_3 films grown on SrTiO_3 (001) substrates by metalorganic chemical vapor deposition (MOCVD) with different thicknesses. Measurements of CTRs were analyzed using COBRA to obtain electron density maps (EDMs) of the film and interface. It was found that films down to 4 unit cells (uc) thick were monodomain with polarization pointing away from the substrate, with a fairly large extracted average polarization value of $\geq 50 \mu\text{C cm}^{-2}$ (compared to $76 \mu\text{C cm}^{-2}$ for bulk PbTiO_3). The polarization, though, appeared to be reduced in layers close to the substrate. These results pointed out that the depolarization field must be screened via some mechanism at the interface and free surface to allow a stable polarization to develop. From the CTR measurements, large apical oxygen displacements were found at the substrate-film interface, which were posited as a possible mechanism for such screening. At elevated temperatures ($\approx 450 \text{ K}$), films developed so-called stripe domains whose polarizations differed by 180° , so that the total film polarization is zero. The stripe domains lead to characteristic in-plane diffuse scattering (i.e. along $q_{\parallel} = H$ or K). Generally, such an in-plane structure leads to a folded COBRA reconstruction, where the EDMs from each domain are superimposed upon each other. By fitting the EDM, however, the authors were able to extract the atomic positions from each domain. In a follow up study, it was found that adsorbed ionic species could compensate the depolarization field on the free surface and, in combination with a conducting substrate, allow a stable monodomain polarization to form in ultrathin films.^[167] This stable polarization persisted down to 3 uc in thickness, even at elevated temperatures where stripe domains formed on insulating substrates.

In BaTiO_3 films, the situation is found to be quite different. Even at 10 uc thick, COBRA analysis by Yacoby et al. shows that BaTiO_3 films grown on SrTiO_3 are not in a monodomain state.^[168] The inclusion of metallic electrodes to help screen depolarization fields did not seem to affect the domain structure; however, it was found that in that it helped improve the epitaxy of thick films grown with an island morphology.^[169] An alternative interfacial mechanism was found in a COBRA study by Kumah et al. to be effective in allowing a polar monodomain BaTiO_3 film to develop.^[170] A buffer structure of 1 uc $\text{LaTiO}_3/3 \text{ uc LaAlO}_3$ was grown between a 4 uc BaTiO_3 film and SrTiO_3 (001) substrate. A polarization mismatch occurs at the $\text{BaTiO}_3/\text{LaTiO}_3$ interface in the stacking of charged planes

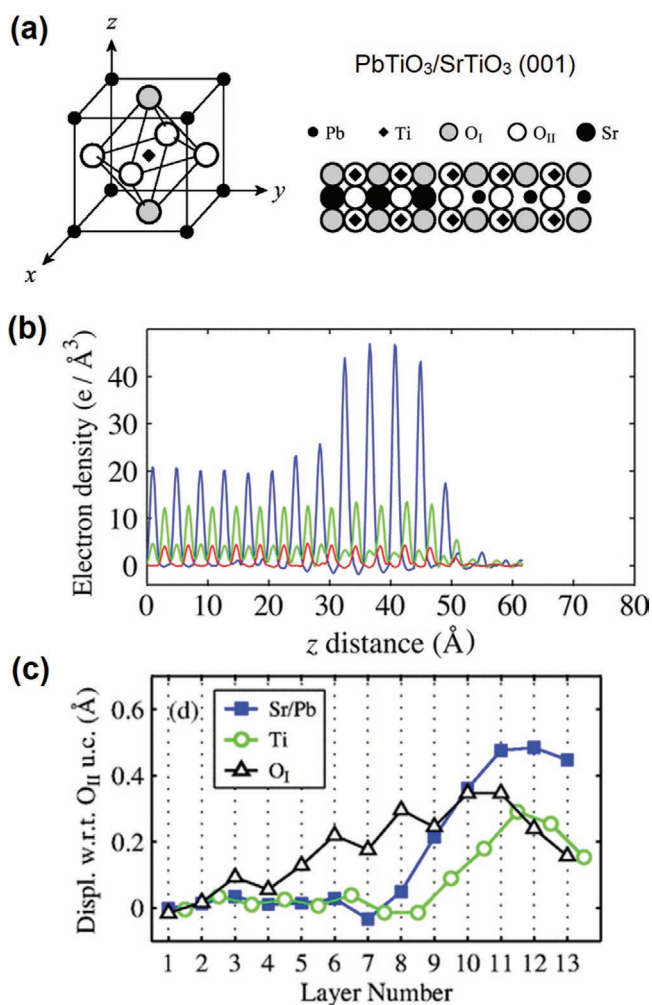


Figure 11. a) Schematic of PbTiO_3 unit cell and structure of film grown on SrTiO_3 ; b) Electron density profile along the z direction from COBRA analysis of CTRs; c) Relative displacements of atoms along the z direction. The O_I displacements on the substrate side of the interface may compensate the ferroelectric polarization of the thin film. Reproduced with permission.^[166] Copyright 2005, American Physical Society.

along the (001) direction. This is analogous to the polarization mismatch leading to the 2D electron gas at the $\text{LaAlO}_3/\text{SrTiO}_3$ surface, which is discussed in 3.3.2. Rather than a charge reconstruction, however, Kumah et al. found that La^{3+} intermixes into the BaTiO_3 film. Such intermixing electrically dopes the BaTiO_3 and relieves strain. This intermixing leads to polar displacements that evolve from zero at the interface to twice that of bulk BaTiO_3 at the surface, resulting in a monodomain state. Importantly, though, the directionality of the displacement is fixed, so the polarization in this type of structure is not switchable in the traditional sense.

These in-depth structural studies by CTR measurements on ferroelectric thin films have elucidated structural effects leading to polarization suppression and identified pathways to engineer stable, ferroelectric structures.

3.3.2. Polar Interfaces

Much of the interest in oxide interfaces springs from the 2004 discovery of a 2D electron gas (2DEG) at the interface between the two wide band gap insulators, LaAlO_3 and SrTiO_3 .^[171] The 2DEG forms above a critical thickness of 3–4 LaAlO_3 uc. Subsequently, superconductivity was discovered at temperatures below ≈ 200 mK^[172] and ferromagnetism develops despite both materials being nonmagnetic.^[173] It was eventually found that 2DEGs can emerge at several related oxide interfaces.^[174]

A prevailing model to explain the interfacial 2DEG is the so-called polar catastrophe, related to the discussion of polar surfaces in Section 3.1.2. For an (001) interface between SrTiO_3 and LaAlO_3 , the stacking along the growth direction leads to a polarization discontinuity between the SrTiO_3 and LaAlO_3 . As a result, an unbounded potential could grow with each subsequent LaAlO_3 unit cell. To alleviate this “catastrophic” situation, an electronic reconstruction may occur above a critical thickness that effectively transfers charge from the surface to the interfacial layer, thereby doping and forming a conducting 2DEG at the interface. This simplistic picture has been highly debated, and many other factors have been found to be important—notably, oxygen vacancies, ionic intermixing, and structural distortions. CTR experiments measure out-of-plane polar displacements of the film and interfacial region, and with suitable analysis, can also provide information on layer-resolved intermixing. Thus, such experiments have been crucial in the understanding of these systems over the last decade.

Willmott et al. provided the first detailed X-ray structural analysis of the $\text{LaAlO}_3/\text{SrTiO}_3$ interface.^[81] They combined COBRA and model refinement of the COBRA-derived structure to study a 5 uc thick film of LaAlO_3 , which is above the critical thickness for 2DEG formation. They found that the lattice spacing between planes increases at the interface and becomes shorter at the LaAlO_3 surface with respect to the bulk. COBRA also allowed for identification of intermixing of La and Sr cations within 1–2 uc at the interface, which forms a metallic (La,Sr) TiO_3 layer between SrTiO_3 and LaAlO_3 . The enlarged unit cell size of (La,Sr) TiO_3 versus SrTiO_3 could explain the stretched interfacial *c*-axis lattice constant. Moreover, DFT calculations show that the inclusion of a LaTiO_3 monolayer between SrTiO_3 and LaAlO_3 (to model the intermixing) provides metallic inter-

facial states with stretched interfacial unit cells as observed in experiment, while no such stretching exists without the monolayer. This intermixed structural model was confirmed by COBRA analysis in varying growth conditions^[175] as well as with analysis using the DCAF phase-retrieval algorithm.^[89] Intermixing was also found via anomalous CTR scattering on a single uc LaAlO_3 film on SrTiO_3 .^[48] It was posited that the intermixing may be driven by the polar catastrophe scenario.

In addition to the intermixing effect, other structural features were found from systematic CTR measurements of different thicknesses of LaAlO_3 on SrTiO_3 and different interface configurations. Pauli et al. measured CTRs for thicknesses from 2 to 5 uc and analyzed them with DCAF to obtain a starting model for structural refinement.^[176] Besides intermixing, significant buckling of the planes in LaAlO_3 were discovered that depend on the layer thickness. This buckling is a manifestation of polar displacements of the ions in response to the electric field in the film, where positively charged cations move toward the surface and the negatively charged oxygen ions move away. The amount of buckling is reduced for the 5 uc film thickness when the 2DEG is formed. Apparently, when charge is transferred to the interface and the polar discontinuity becomes partly screened, the film is less polarized and less buckling is observed. This notion was largely confirmed by measurements of the *c*-axis lattice expansion as a function of thickness, which was interpreted as an electrostrictive effect.^[177]

One of the interesting aspects of the observation of the polar distortions in LaAlO_3 on SrTiO_3 is that it can explain the observed critical thickness of 4 uc. Without the distortions, the potential due to the polar stacking in LaAlO_3 would lead to the expectation of charge transfer within 2–3 uc, while the buckling reduces the potential build-up per layer, leading to a 4 uc critical thickness. Other pertinent structural results concern the difference between SrO/AlO_2 interfaces, which are insulating, and TiO_2/LaO interfaces, which are metallic. Yamamoto et al. used COBRA to show that the intermixed and polarized regions are narrower in the SrO/AlO_2 case, which can partly explain the lack of electronic reconstruction in this system.^[178] Results from this study are shown in **Figure 12**. Most recently, superstructure peaks were measured on LaAlO_3 on SrTiO_3 in addition to COBRA analysis of the integer order CTRs. From these measurements, Fister et al. were able to determine the pattern and magnitude of octahedral tilts, which appear to be coupled to the polar displacements in the LaAlO_3 .^[179] The significance of the octahedral rotations on the 2DEG formation has yet to be understood.

The $\text{LaAlO}_3/\text{SrTiO}_3$ system is one in which layer resolved structural information, as determined in pristine samples by CTR experiments, provided significant insights into the physics driving the relevant electronic property—in this case, 2DEG formation. The motifs discussed here, including the development and influence of polar distortions, apply to many other systems examined below.

3.3.3. Strongly Correlated Oxides

One of the most important areas of modern condensed matter research to which CTR measurements have contributed

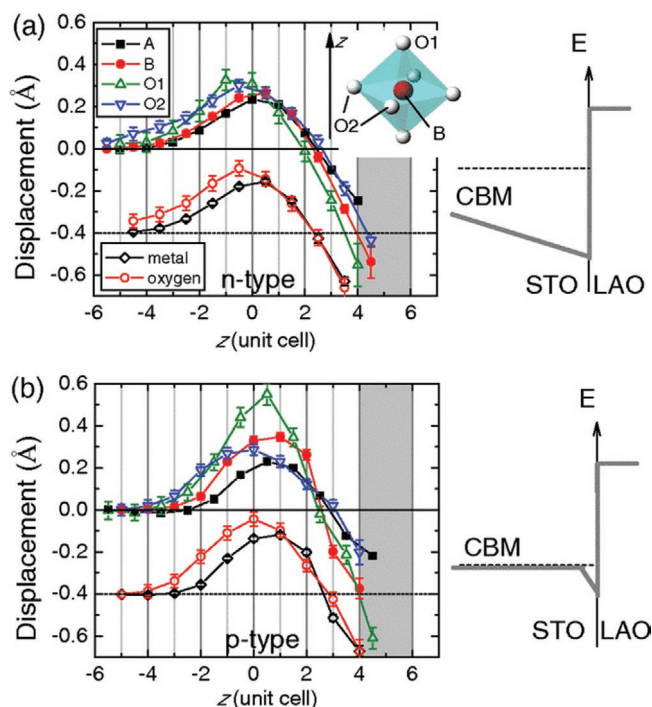


Figure 12. a) Displacements of atoms in a 5 uc thick LaAlO_3 film on SrTiO_3 (001) with a TiO_2/LaO interface. The average displacement of the metal and oxygen sites is shifted down. On the right is a schematic of the band energy as a function of z as determined from the polar displacements. b) Same as (a) but for an SrO/AlO_2 interface. Reproduced with permission.^[178] Copyright 2011, American Physical Society.

has been in the study of so-called strongly correlated materials, of which complex oxides play an important role. These materials in general possess bulk phase diagrams displaying many ordered states as a function of some internal or external parameter—for instance chemical doping, pressure, or magnetic field.^[180] Their phase diagrams exhibit some of the most fascinating and intensely studied phenomena over the last few decades, among them high-temperature superconductivity, colossal magnetoresistance, and the metal-insulator transition.

Correlated oxides can now be routinely grown epitaxially using methods such as pulsed laser deposition, magnetron sputtering, and molecular beam epitaxy. Single-component thin films have been shown to exhibit different properties from the bulk due to dimensional or interfacial considerations. Moreover, researchers have developed techniques to build heterostructures comprising stacks of multiple oxides (correlated or noncorrelated) with atomic layer precision. These heterostructures have many degrees of freedom in their design, such as layer composition, thickness, and stacking order, which lead to different macroscopic and microscopic properties. Understanding the mechanisms at work at correlated oxide interfaces is an important ongoing research challenge that may allow for tailored engineering of specific material functionalities in the future. CTR scattering has emerged as a vital and useful tool in this quest, since slight structural deformations can have a large impact on electronic behavior in correlated oxides. We highlight in the following CTR work that has helped elucidate physical

principles at correlated oxide interfaces, classified according to well-studied material families.

Manganites: Rare-earth, doped manganites exhibit colossal magnetoresistance as well as various magnetic, charge, and orbital ordering patterns depending on the doping level. For bulk ferromagnetic metallic compounds, it was found that ultrathin films below a certain thickness became insulating with suppressed magnetic order.^[181,182] The concept of a “dead layer” at the interface was proposed to explain this effect, in which an inert buffer layer forms between the substrate and the portion of the film that displays bulk-like behavior. The purported dead layer essentially represents an interfacial region of the film that experiences some chemical, structural, and/or electronic distortions that modify the properties of the film. High-resolution CTR experiments were crucial to developing an understanding of the dead layer formation and its effect on the properties of manganite films.

In $\text{La}_{1-x}\text{Sr}_x\text{MnO}_3$ (LSMO), with $x = \frac{1}{3}$, the critical thickness above which one observes ferromagnetic and metallic behavior in the film is ≈ 7 uc. Herger et al. measured CTRs and performed COBRA analysis of LSMO films grown on SrTiO_3 (001) substrates with thicknesses varying from 1 to 9 uc.^[183] The films were measured in situ in the growth chamber directly after growth to avoid contamination from adsorbates in the atmosphere. A number of important observations were made from the layer-resolved measurements. It was found that the c -axis of the LSMO is expanded for the first 3–4 interfacial layers, contrary to the expected contraction due to the tensile strain of the SrTiO_3 substrate. In addition, it was found that the nominal film stoichiometry is reached only after a transition region of several layers with mixed occupancy, which could be explained on both electrostatic and thermodynamic grounds. Finally, an enhancement of Sr occupation at the surface layer appears for each film thickness. Later analysis of the 3 uc LSMO film with the DCAF phase retrieval algorithm agreed quantitatively with the aforementioned COBRA analysis (to within ≈ 2 –3 pm in the c -axis parameters).^[89]

To describe the critical thickness from the layer-resolved structure and occupancies, one can extract an effective parameter describing the electronic hopping between adjacent sites (t), which controls the conduction and magnetic exchange in manganites. In transition metal oxides, the electronic bandwidth (W) of the hybridized transition metal (M) 3d–O 2p band is proportional to t and is related to the atomic structure as follows

$$W \propto \frac{\cos\left(\frac{\pi - \phi}{2}\right)}{d_{\text{MO}}^{7/2}} \quad (36)$$

where ϕ is the M–O–M bond angle and d_{MO} is the M–O bond distance. Herger et al. computed this quantity for each MnO_2 layer in their CTR-derived structures and compared it to that obtained from bulk LSMO (Figure 13). They find that, due to the interface and surface changes in structure and occupancy, the average W reaches the bulk value between a thickness of 6 and 9 uc. This result provides a structural explanation of the observed dead layer effect in manganite thin films, with a critical thickness in agreement with electrical measurements.

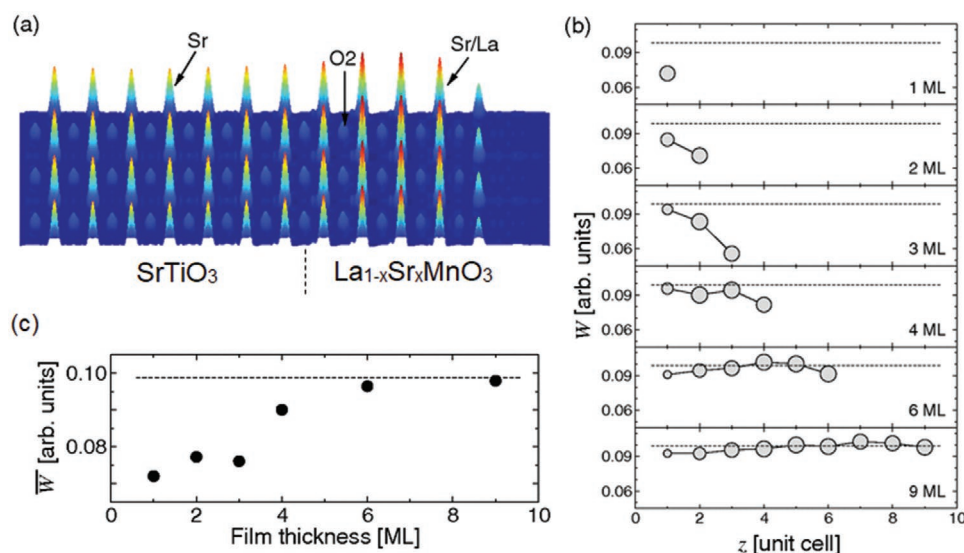


Figure 13. a) COBRA-derived electron density map of a 4 uc La_{1-x}Sr_xMnO₃ ($x = \frac{1}{3}$) film on SrTiO₃ (001). b) Layer-resolved bandwidth, W , from Equation (36) for LSMO films of different thickness grown on SrTiO₃. The size of the circles is related to the Mn occupancy of a layer, which gives the weight of that layer to the averaged value shown in (c). Structural parameters and occupancies are determined from the COBRA analysis of each film. Reproduced with permission.^[183] Copyright 2008, American Physical Society.

Recent measurements by Koohfar et al. on 10 uc films of LSMO with $x = 0.2$ show similar interfacial features;^[96] in addition, the polar nature of the LSMO/STO interface was investigated in more detail. A planar buckling (relative displacement between cation and oxygen) was observed, and the nonzero polar displacements coincide with the c -axis expansion at the surface and interface. Thus, despite the smaller polar discontinuity with respect to LaAlO₃/SrTiO₃ (see Section 3.3.2), both intermixing and polar distortions coexist as screening mechanisms. Moreover, the polar distortions drive the reduced bandwidth observed in LSMO/SrTiO₃, and hence may be a key factor in the dead layer effect. These reconstructions could be suppressed at LSMO/La_{1-x}Cr_xO₃ interfaces with $x = 0.3$, and such structures were found to allow ferromagnetic ordering down to LSMO layer thicknesses of 2 uc.

Heterostructures and Superlattices: Multilayered heterostructures and superlattices composed of multiple different oxide layers offer more knobs to tune functional properties due to the presence of multiple interfaces whose influences can be tuned by choosing layer thicknesses, compositions, and stacking sequences. Such structures can be synthesized with atomically precise interfaces using current growth techniques. Interfacial effects may have different influences from those of single component films grown on substrates because reconstructions may propagate and interact across multiple interfaces.

The electronic and magnetic properties in superlattices of various types have been extensively studied, and the atomic structure is most often studied via STEM imaging. As mentioned in Section 2.6.4, direct methods to retrieve structures from CTR measurements are restricted to generally 10 or so atomic layers and thus cannot be effectively used for superlattices, which can be composed of hundreds of atomic layers. Instead, heterostructures with fewer superlattice repeat units can be analyzed, or analyses based on model refinement alone are used.

For instance, a Pr_{0.5}Ca_{0.5}MnO₃/La_{0.5}Sr_{0.5}MnO₃ (PCMO/LSMO) bilayer was studied using COBRA in order to understand the peculiar magnetic behavior of PCMO/LSMO superlattices.^[184] Bulk PCMO is an antiferromagnetic insulator at this doping level and LSMO is a ferromagnetic metal; however, the magnetization of PCMO/LSMO superlattices does not scale linearly with the LSMO layer fraction. COBRA results demonstrated that the two closest interfacial layers experience intermixing, which could explain the observed magnetization behavior.

A different motif was studied in La_{0.7}Sr_{0.3}MnO₃/Eu_{0.7}Sr_{0.3}MnO₃ (LSMO/ESMO) superlattices by Moon et al.^[185] In bulk form, LSMO and ESMO have different tilting patterns of their oxygen octahedra, which account for their different physical properties. They tracked superstructure (half-order) peaks in CTRs from these superlattices to see how oxygen octahedral tilting/rotation patterns propagate across interfaces when the thicknesses of the layers are changed. In conjunction with STEM imaging, they were able to show that the tilt patterns extend across interfaces on a scale of 4 uc. Thus, the thickness of each layer in the superlattice can be used to control the relative influence of each tilt pattern on the macroscopic magnetization. The coupling of oxygen octahedral rotations across interfaces is an emerging route to tailoring materials properties, distinct from chemical or strain effects previously exploited.

Cuprates: The discovery of high-temperature superconductivity in cuprates served as a major impetus for the intense research on complex oxides and other correlated electron materials over the past 30 years. Part of this activity entails the study of epitaxial cuprate films, pursued with the aim of understanding and controlling superconductivity. The superconducting properties have been found to vary significantly based on the substrate, thickness, and growth conditions. Moreover,

some theoretical studies and bulk experimental analyses correlate the apical Cu–O distance to superconductivity.^[186,187] In these respects, detailed studies concerning the structure of epitaxial cuprate interfaces via high-resolution CTR experiments are extremely valuable.

The structure of ultrathin $\text{YBa}_2\text{Cu}_3\text{O}_{7-\delta}$ (YBCO) films grown on two different oxide substrates (SrTiO_3 and $(\text{La},\text{Sr})(\text{Al},\text{Ta})\text{O}_3$) was studied by Schlepütz et al. using the DCAF phase-retrieval method in combination with model refinement.^[188] As noted in their paper, such an analysis is exceedingly difficult due to the large number of atom positions to be determined (over 80) to fully characterize the interface and the 3–4 uc of YBCO film. Both substrates impart tensile strain and the films featured reduced superconducting transition temperatures (T_c) compared to the bulk (43 K on SrTiO_3 , 68 on $(\text{La},\text{Sr})(\text{Al},\text{Ta})\text{O}_3$, and 91 K in bulk). Structurally, the main results showed that on both substrates the structure of the YBCO film is bulk-like with a slight dilation of the c -axis at the interface and contraction at the surface of <1%. Determination of the relative contraction between the two substrates was not possible within the experimental accuracy (± 4 pm for this experiment). The observed c -axis modifications reflect changes in the apical Cu–O bond length and may be related to the reduced T_c in the films. More definitively, this study established the bulk-like nature of the film structure and growth sequence of planes at the YBCO/substrate interface, which informs future theoretical work. An interesting note is that for this system, COBRA analysis could not be used due to ambiguity in the substrate surface termination and growth layer sequence.

Films of a different cuprate, $\text{La}_{2-x}\text{Sr}_x\text{CuO}_4$ (LSCO), were examined by Zhou et al. and later Yacoby et al.^[189,190] These films are grown on $(\text{La},\text{Sr})\text{AlO}_4$ substrates, which impart a compressive strain; they can be made metallic, insulating or

superconducting based on the doping level x . The experiments of Zhou et al. concern metal–insulator bilayers, in which interfacial superconductivity was previously found, arising due to the modulation of carrier density.^[191] Their analysis combined COBRA with DCAF and focused on the apical Cu–O bond distance (c_a), which as mentioned above, may influence the strength of the superconductivity. They found that c_a steadily increases from the metal–insulator interface to the surface of the insulating layer by $\approx 10\%$. In single-phase metallic or superconducting films, no such elongation is observed. This elongation may result from ionic screening of the interfacial charge density, analogous to the effect found at the surface of polar insulators (LaAlO_3 and LSMO, see Section 3.3.2). Interestingly, the superconducting region close to the interface in the metal–insulator bilayer has a similar value of c_a as the single-phase superconducting film and a correspondingly comparable T_c . The observation lends support to the correlation between c_a and T_c . Hence, it was speculated that if the c_a elongation near the surface in the metal–insulator bilayer can be imparted closer to the superconducting interface, T_c might be enhanced.

Yacoby et al.'s work concerned the distribution of Sr dopants in LSCO bilayers and single-phase films.^[189] Due to the low concentration of Sr and low contrast between doped and undoped layers, they utilized a variant of COBRA deemed energy-differential COBRA. This method consists of measuring the diffraction intensities at two energies, one close and one far from the Sr K -shell absorption edge (≈ 16.1 keV). A complete data set in the nonresonant condition is used to fit the structural model, and the differential signal between the two energies, as shown in **Figure 14**, allows for determination of the Sr occupancy in each layer. This method improved the determination of site occupancy significantly. The LSCO structure consists of a single CuO_2 plane surrounded by $(\text{La},\text{Sr})\text{O}$ layers, which

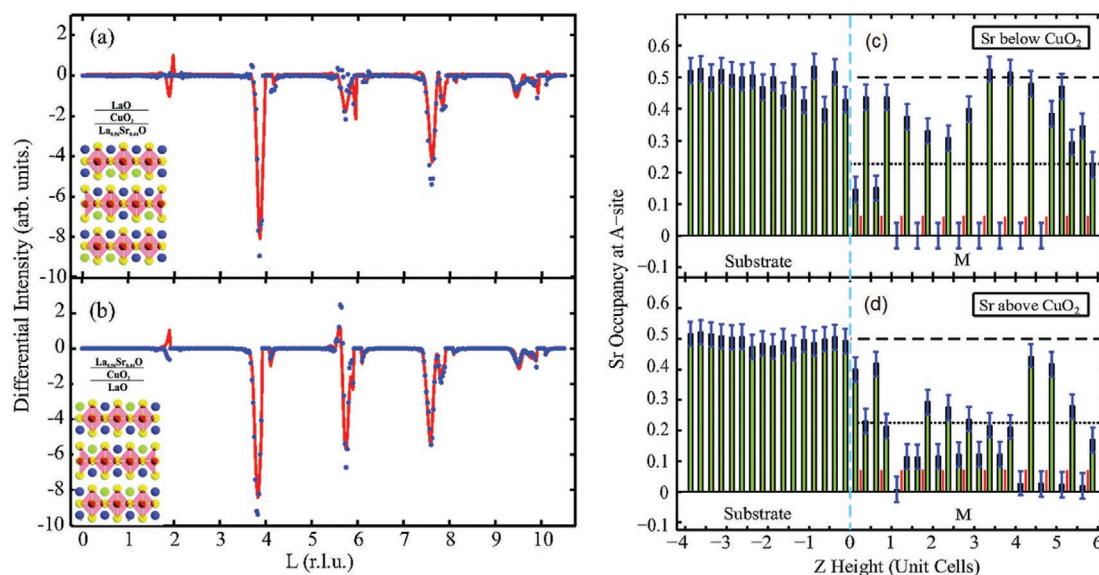


Figure 14. a,b) Differential CTR signal for $\text{La}_{2-x}\text{Sr}_x\text{CuO}_4$ grown on $(\text{La},\text{Sr})\text{AlO}_4$ (001) for two different growth sequences, as shown in the insets. a) All Sr dopants are deposited below the CuO_2 layer and b) all Sr dopants are deposited above the CuO_2 layer. The signal shown as blue circles shows the difference between the CTR intensity measured above and below the Sr K absorption edge, and the red lines are fits using the differential COBRA method. c,d) Sr occupancy as a function of layer for the two cases in (a) and (b) with the CuO_2 position shown as a red line segment. Reproduced with permission.^[189] Copyright 2013, American Physical Society.

nominally would have equal concentrations of Sr. Surprisingly, Yacoby et al.'s analysis found that in all samples, regardless of desired growth sequence, the Sr concentration was higher above the CuO_2 (closer to the surface) than below (closer to the substrate). The result implies a breaking of inversion symmetry in the film, which may arise from charge discontinuities at the substrate and/or surface. This phenomenon could be present in other types of doped films.

Nickelates: Rare-earth nickelates, like other classes of correlated oxides, exhibit metal–insulator and paramagnetic–antiferromagnetic phase transitions. In thin film form, their conductivity and phase transition temperatures have been found to be highly tunable via, for instance, strain, and thickness.^[192] In addition, due to their similarity to superconducting cuprate materials, some theorists proposed the possibility of inducing high-temperature superconductivity by modifying electronic structure in nickelate superlattices.^[193] These developments sparked significant research over the last decade concerning control over electronic properties in nickelate heterostructures. Perhaps more so than any other recent system, high-resolution structural measurements have made clear the intimate structure–property relationship at nickelate interfaces, which have served as models for understanding many other complex oxides.

One of the important initial discoveries concerning nickelate interfaces was the observation of a thickness-dependent transition from metallic to insulating behavior in ultrathin LaNiO_3 films, with a critical thickness of 3–5 uc.^[194,195] Based on electrical characterization, the transition was originally attributed primarily to a dimensional crossover from 3D to 2D. Not until later crystal truncation rod measurements by Kumah et al. did the driving role of structural deformations become evident.^[196–198] In these experiments, CTRs of a series of LaNiO_3 films of varying thickness grown on LaAlO_3 (001) were measured and analyzed using COBRA with subsequent model refinement. LaNiO_3 has a polar stacking along the [001] direction of charged $(\text{NiO}_2)^-$ and $(\text{LaO})^+$ planes. As in the other polar systems discussed earlier, its surface (in this case, NiO_2 layer

termination) was found to exhibit large out-of-plane displacements ($\approx 0.2 \text{ \AA}$) between the Ni and O ions. The surface polar displacements persist for all film thicknesses, and the screening length over which the displacements fall to zero is between 3–5 uc, matching the critical thickness for metallic conduction. A structural explanation of the thickness-dependent metal–insulator transition was thus concluded as follows: The polar displacements cause Ni–O–Ni bond angle distortions resulting in reduced bandwidth (see Equation (36)) for layers closest to the surface. Hence, the surface layers are insulating, while the undistorted layers farther than 3–5 uc from the surface have bulk-like structure and are metallic. Films with thickness greater than the screening length have at least one undistorted layer and exhibit metallic conduction. This picture was verified by an experiment in which the surface polar discontinuity was eliminated by the deposition of a capping layer of LaAlO_3 on a 3 uc LaNiO_3 film. CTR measurements confirmed that polar distortions were eliminated in all LaNiO_3 layers, and the heterostructure indeed displayed metallic conduction.

Naively, one might expect that upon changing the surface termination of the film from $(\text{NiO}_2)^-$ to $(\text{LaO})^+$, the sign of the polar displacements would simply reverse, leaving the magnitude of the bond distortions and the electrical conductivity unchanged. Kumah et al. also showed this scenario not to be the case in nickelates using CTR measurements and COBRA analysis.^[198] The results are shown in in **Figure 15**, revealing that, in the case of LaO termination, while the sign of the polar displacements does reverse, they are present only in the LaO layers, while for NiO_2 termination, both LaO and NiO_2 layers distort. As the electrical properties are dominated by the Ni–O bonding, it was found that LaO-terminated films are metallic even for thicknesses of 3–4 uc. The layer resolved structure determined from the CTR measurements agreed quantitatively with DFT calculations, which could provide a microscopic explanation for this unexpected effect based on the relative bond stiffness and mechanical forces acting on each layer. In addition, X-ray absorption spectroscopy verified the increased Ni–O orbital hybridization for LaO-terminated surfaces compared to

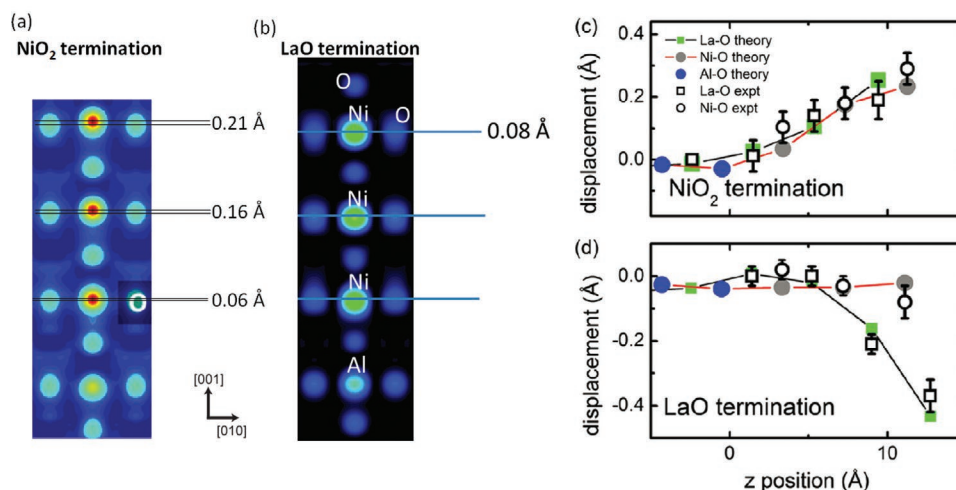


Figure 15. (Left) Cuts through COBRA-derived EDMs for 3 uc LaNiO_3 films on LaAlO_3 (001) with a) NiO_2 and b) LaO terminations. Polar Ni–O displacements are labeled. a,b) Reproduced with permission.^[196] Copyright 2013, American Physical Society. (Right) Extracted values of polar displacements from refined fits and DFT for (c) NiO_2 and (d) LaO terminations. c,d) Reproduced with permission.^[198] Copyright 2014, American Physical Society.

NiO₂-terminated surfaces, validating the basis of the metallicity. The rare coexistence of metallic conduction and polar ionic displacements over the film thickness places ultrathin LaO-terminated LaNiO₃ in the category of polar metals. Films of NdNiO₃ grown on LaAlO₃ (111) were also identified as polar metals in the work of Kim et al., which attributed the polar displacements to substrate-induced constraints using COBRA and scanning transmission electron microscopy.^[31]

Based on empirical notions of high-temperature superconductivity, a main objective for research concerning interfacial control of nickelates has been to achieve orbital degeneracy breaking—in particular, between the d orbitals of e_g symmetry (d_{x²-y²} and d_{3z²-r²}), which have identical energies in bulk nickelates because of octahedral symmetry. In this simplest case, to realize this symmetry breaking, the structure must distort such that planar and apical Ni–O bond lengths differ appreciably. Several early efforts showed that epitaxial strain alone was not sufficient. Aided by high-resolution CTR analysis, two alternative interfacial structural engineering routes were demonstrated to attain substantial symmetry breaking. In the first, Nelson-Cheeseman et al. studied LaSrNiO₄ films grown on LaSrAlO₄ substrates with different layer compositions.^[199] They compared structures in which the (La,Sr)O planes are ordered (e.g., LaO/NiO₂/SrO) with an alloyed structure (La_{0.5}Sr_{0.5}/NiO₂/La_{0.5}Sr_{0.5}). Due to the different charge of the (LaO)⁺ and (SrO)⁰ planes, the ordered and alloyed structures create polar and nonpolar electrostatic environments around the Ni layer, respectively. COBRA analysis revealed that in the ordered case, the apical Ni–O bond length asymmetrically deforms near the surface, lengthening toward the LaO layer and contracting toward the SrO layer. The maximum bond length change was found to be >≈10%. In the alloyed structure, no apical bond length modifications were observed. In another experiment, an asymmetric environment was designed using a three-component heterostructure composed of LaTiO₃, LaNiO₃, and LaAlO₃.^[200] In this case, the LaTiO₃ transfers an electron unidirectionally to the LaNiO₃ layer due to an electronegativity mismatch. This transfer produces a polar field pointing toward the Ni, stretching the apical Ni–O bond. From the electron density map extracted by the COBRA analyzed CTR measurements, bond length stretching up to ≈15% was found. X-ray absorption measurements of the three-component heterostructure detected a ≈50% change in orbital occupation associated with the symmetry breaking, closely approaching the electronic structure of superconducting cuprates.

These and other high-resolution structural measurements on nickelate systems have provided significant insight on the interfacial control of electronic structure. In this respect, the corroboration of experimental and DFT-calculated structures has allowed researchers to tie macroscopic behavior to microscopic mechanisms. In addition, the pliability of nickelate structural and electronic properties has afforded nickelates a place as a model for substantiating methods of control and characterization generally applicable to other epitaxial oxide systems. For instance, besides the examples discussed above, May et al. used LaNiO₃ thin films on different substrates to establish a consistent and now often used procedure for quantifying octahedral rotations based on the measurement of half-order Bragg reflections.^[201]

Cobaltates: In addition to their unique electronic and magnetic states, complex transition metal oxides have also been explored for their catalytic properties. One main catalytic opportunity for these materials is to improve the efficiency of oxidation and reduction reactions, which are used in a number of energy storage and conversion applications.^[203,204] Cobaltates in the family of (La,Sr)CoO_{3-δ} (LSCO), in particular, have been used in fuel cells, and it has been observed that the catalytic activity for oxygen reduction is increased by orders of magnitude in thin films and heterostructures compared to bulk crystals.^[205] Recent high-resolution CTR measurements have helped to elucidate chemical and structural mechanisms in these films that affect their electrochemical properties.

Feng et al. measured CTRs in perovskite (La,Sr)CoO_{3-δ} films grown on SrTiO₃, as well as heterostructures of the Ruddlesden–Popper variant (La,Sr)₂CoO_{4-δ} with the perovskite (La,Sr)CoO_{3-δ} grown on SrTiO₃.^[202,206] In both cases, the researchers used the energy-differential COBRA method to analyze the data, as had been exploited in earlier experiments on cuprates (see Section 3.3.3). The energies were chosen around the Sr K edge in order to provide sensitivity to the Sr occupation. In the single-component LSCO films (see **Figure 16**), they found pronounced Sr segregation toward the surface, in which the first 2–4 uc closest to the interface are nearly devoid of Sr, for two measured samples with different nominal doping concentrations (20% and 40% Sr). In addition, from the extracted electron density maps, apical oxygen displacements toward the surface as well as oxygen octahedral rotations were detected. These effects could be driven by a combination of substrate constraints and an internal polar field, which, as discussed in previous examples, develops due to the polar discontinuity between (La,Sr)CoO₃ and the substrate/vacuum. The oxygen distortions and the enhanced occupation of Sr ions toward the surface, which changes the oxidation state of the surface layers and influences oxygen ion transport, may pertain to the observed changes in surface chemistry in thin films versus bulk. In systems with islands of (La,Sr)₂CoO_{4-δ} deposited on (La,Sr)CoO_{3-δ}, even further enhancement of oxygen reduction activity had been reported relative to single-component films. COBRA analysis of epitaxial (La,Sr)₂CoO_{4-δ}/(La,Sr)CoO_{3-δ} heterostructures revealed segregation of Sr in the (La,Sr)CoO_{3-δ} layers toward the interface, as well as Sr segregation within the (La,Sr)₂CoO_{4-δ} toward the interface and film surface. Again, the Sr enhancement at the interface and surface provides a potential explanation for the observed catalytic behavior.

3.3.4. Oxide–Semiconductor Interfaces

For decades, complex oxide materials have been considered potential replacements for conventional gate dielectrics in semiconductor-based technologies. Advantages of complex oxides for this purpose include lower power consumption, continued transistor performance gains, and potential nonvolatile operation. A key aspect in the development of such technologies is the ability to reliably integrate them on widely used semiconductor templates, such as silicon and germanium.^[207]

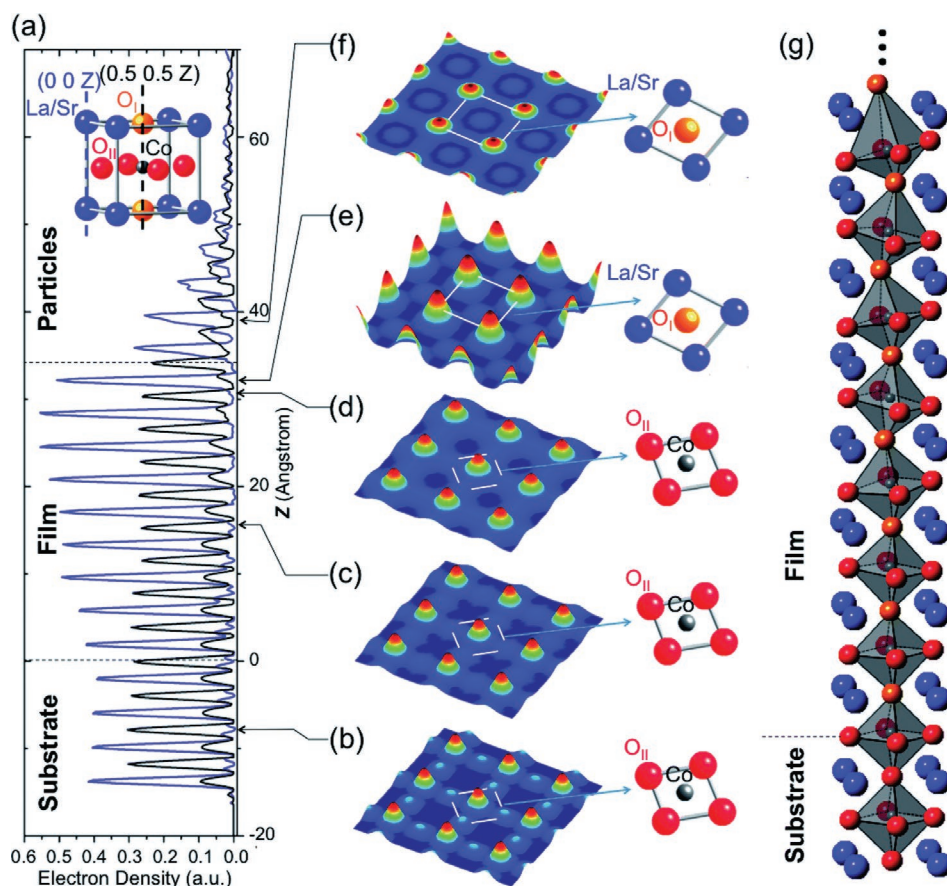


Figure 16. a) COBRA-derived electron density of a (La,Sr)CoO_{3-δ} film on SrTiO₃. The cuts along *z* shown in blue and black are taken through the lines in the unit cell shown in the inset. b–f) In-plane electron density maps at various planes along *z* indicated by the black arrows along with model structural units for reference. The diffuse oxygen regions in (c) and (d) are indicative of octahedral tilting. g) Crystal structure model displaying the octahedral rotations inferred from the electron density map. Reproduced with permission.^[202] Copyright 2014, Royal Society of Chemistry.

The first reported epitaxial growth of SrTiO₃ on Si by molecular beam epitaxy demonstrated the importance of careful engineering of the interface structure in obtaining crystalline, atomically clean oxide films.^[208] The growth requires the initial deposition of a submonolayer (ML) Sr template on Si ($\frac{1}{2}$ coverage) with subsequent oxidation and further oxide film deposition. This procedure was used to grow SrTiO₃ films on Si, as well as BaO, BaTiO₃, LaAlO₃, and others. Devices made from such films display intriguing dielectric responses; however, optimizing device performance necessitates understanding the precise structure of these buried interfaces, which can be accessed with CTR measurements and analysis.

The earliest such investigation was carried out on the BaO/Si(001) interface by Segal et al.^[209] In situ reflection high-energy electron diffraction (RHEED) indicated a 2×1 periodic reconstruction associated with the $\frac{1}{2}$ ML Sr template during growth.^[210] CTRs at half-order reciprocal lattice positions with respect to Si (i.e., along $(\frac{1}{2}, \frac{1}{2}, L)$ rods) were observed, showing that the interface maintained this reconstruction after growth. In oxide/semiconductor systems, dozens of models of the interface have been proposed theoretically. Rather than performing structural refinement, the CTR measurements of BaO/Si were

compared directly to several proposed models whose structures were calculated by DFT. Agreement was found with a model that includes the $\frac{1}{2}$ ML Sr as well as a layer of oxygen, which bonds to the Si surface.

Interestingly, for the growth of SrTiO₃/Si (001), no 2×1 reconstruction of the interface was detected in CTR experiments, although such patterns appear in RHEED during growth.^[212] With the commensurate 1×1 interface, SrTiO₃ films coherently strained to Si display out-of-plane polar distortions, similar to those discussed for polar oxide–oxide interfaces. In each layer of SrTiO₃, apical O ions displace toward the interface and Ti ions displace toward the surface. The magnitude and direction of the polar displacement at the interface is consistent across films with different surface polarizations and terminations, indicating that the polarization in SrTiO₃ is primarily set by the interfacial structure. DFT calculations agree with this interpretation, in which charge transfer between the interfacial Sr layer and the first TiO₂ plane creates an interfacial dipole.^[213] These measurements helped to resolve debate regarding the existence of ferroelectricity in SrTiO₃/Si. Similar polar structures were recently observed at the Zr-doped SrTiO₃/Ge interface by means of CTR measurements.^[214]

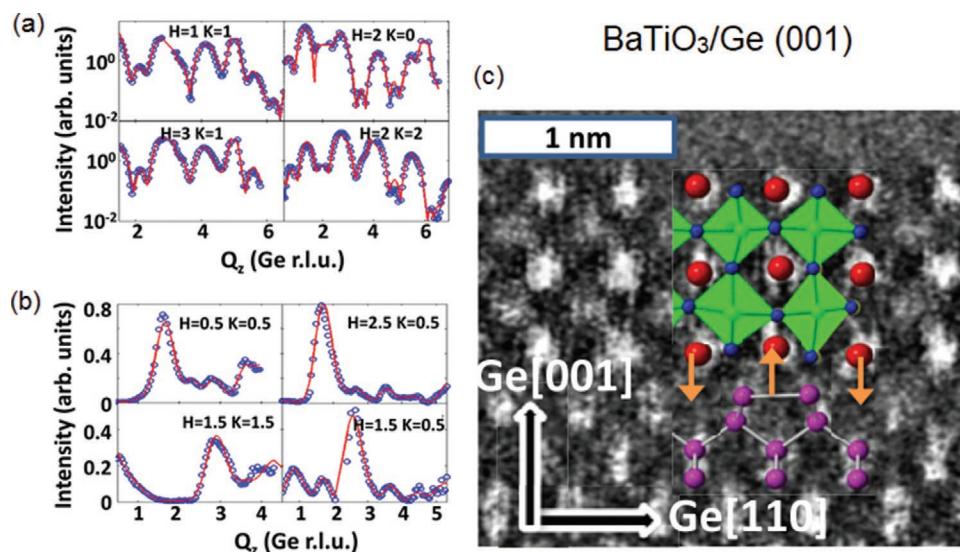


Figure 17. a) Integer- and b) half-order CTRs for 2.5 uc BaTiO₃ grown on Ge (001) by molecular beam epitaxy. Measured data shown in blue circles and fits from a refinement of the COBRA model are shown as red lines. c) The structural model of the interface from the CTR measurements superimposed on a TEM image, showing good agreement. From the structural model, rumpling of interfacial Ba and a breathing distortion of the TiO₆ octahedra can be seen. Reproduced with permission.^[211] Copyright 2016, American Physical Society.

The interface structure between BaTiO₃ and Ge (001) was also determined by CTR analysis using COBRA electron densities as a starting model for refinement (see Figure 17).^[211] This system, in comparison with the SrTiO₃/Si system, has the appeal of consisting of a well-known ferroelectric with a widely used semiconductor substrate, which could be the basis of nonvolatile capacitors and transistors. In growing this structure, $\frac{1}{2}$ ML of Ba was used instead of Sr as a template layer before growing the rest of the structure. Half-order CTRs were observed in this system, depending on the specific growth conditions, which arise from a dimerization of Ge atoms at the interface. Further, the 2×1 structure of the Ge surface appears to drive distinctive distortions in the interfacial BaTiO₃ layers: the analysis reveals out-of-plane displacements of the interfacial Ba, which are accompanied by a so-called “breathing mode” distortion of the adjacent TiO₆ layer. The breathing mode in this case refers to a compression and elongation of Ti–O bonds with a 2×1 periodicity. The resulting structure has polarization components pointing both in- and out-of-plane. Both STEM imaging and DFT calculations agree with the structure extracted from the CTR analysis, providing important corroboration for this unique interfacial structure. The structural accordance with DFT is especially valuable, as a constructive interpretation was provided by DFT calculations. According to the calculations, the observed interfacial BaTiO₃ distortion corresponds mainly to a soft phonon mode of the bulk crystal, which is evidently stabilized by the 2×1 reconstruction of the Ge at the interface. This interpretation hints at the possibility of using substrates that can stabilize soft modes present in a material’s bulk phonon spectrum to obtain particular structural distortions in epitaxial layers.

Another oxide–semiconductor system studied by high-resolution CTR methods is the epitaxial interface between GaAs (100) and Gd₂O₃, which is used as a passivation layer for the

semiconductor. The system provided an early application of the COBRA algorithm, and Yacoby et al. used it to show that the Gd₂O₃ film is significantly modified relative to the bulk due to the substrate.^[80,215,216] Gd₂O₃ assumes the in-plane atomic positions of the GaAs coherently within the first few layers and modifies its stacking order to match the GaAs. The results may help to explain the efficacy of Gd₂O₃ as a passivation layer.

The study and control over oxide–semiconductor interfaces is still an active field of research. The advantages provided by the interface sensitivity and resolution of CTR measurements suggest that this technique will remain useful as technological applications of these heterostructures mature.

Chalcogenide–Oxide: While differing from the oxide on semiconductor works above, interfaces between chalcogenides and oxides, especially the FeSe/oxide interface, have attracted much attention since the report of superconductivity in single-unit-cell FeSe grown on SrTiO₃ (001) with T_c as high as 100 K.^[217,218] Bulk FeSe undergoes a superconducting transition at 8 K, but signatures of enhanced superconductivity have been observed in single-unit-cell FeSe on SrTiO₃, TiO₂,^[219] and BaTiO₃.^[220] substrates. The critical role of the interface, rather than simple strain, for example, has been established in several experiments; however, the physical mechanism providing the elevated T_c remains under debate. Interfacial electron–phonon coupling, charge transfer, oxygen vacancies, and other scenarios have been presented as potential driving forces.

A CTR experiment was recently performed that contributed information about the interface that had not been earlier observed by scanning tunneling microscopy and electron diffraction methods. Zou et al. measured CTRs from single-unit-cell FeSe on SrTiO₃ (001) grown under various conditions.^[221] They analyzed the data by modeling the interface with different interfacial structures. The key result is that under conditions which yield superconducting samples, a double TiO₂ layer at

the interface is present, rather than the expected stoichiometric single TiO_2 . This termination is also found by cross-section scanning transmission electron microscopy.^[222] The double TiO_2 termination leads to a reconstruction of the interfacial layer of SrTiO_3 with a $\sqrt{13} \times \sqrt{13}$ periodicity, which is observed as superstructure peaks in the X-ray diffraction. DFT calculations point out that stronger electron transfer between the SrTiO_3 and the FeSe is present when the SrTiO_3 has a double TiO_2 termination rather than the usual single TiO_2 layer termination. This electron transfer may help explain the enhanced superconductivity. The determination of this interface structure also provides a known starting point for future theoretical explorations of this system.

4. Conclusion

As seen from the applications highlighted in Section 3, CTRs provide a unique view of interfacial structures that complements and supplements alternative techniques and theories. It can also be integrated together with first-principles theory to support interpretations of electronic, magnetic, or chemical phenomena. New ways to exploit CTRs and new applications for CTR-based techniques are in constant development. To conclude this review, we first summarize and draw attention to overarching themes related to the use of CTRs in contemporary research on surfaces, interfaces, thin films, and heterostructures. We then consider an outlook with extensions of CTRs that have not been touched on in this review, as well as emerging trends for future experiments.

4.1. Themes

In terms of modern applications of CTR scattering that are presented in this review, the overarching themes may be delineated by the information extracted from CTRs and utilized in a given experiment. Generally, the use of CTR scattering is in determining the position and type of each atom near a surface or an interface as a function of layer. To re-emphasize the point made in the review, since the atomic positions at an interface or surface region can have significant deviations from the crystal structure of the bulk, the ability to map the atomic positions in a layer-by-layer fashion is crucial to understanding physical and chemical properties related to the interface. Measurement of CTR scattering, in contrast to the usual Bragg peak intensities, allows one to access this layer-dependent information due to the interference of the scattered waves from the bulk and the surface/interfacial region. However, from full reconstructions of the system (such as when direct methods are used to create electron density maps), the amount of extracted data is vast, and key features must be identified.

Unexpectedly, one of the most powerful uses of CTRs has been in determining the occupancy of atoms in a given layer based on the integrated electron density. As mentioned earlier, this ability mirrors that provided by Z-contrast TEM imaging. This type of analysis has often been exploited to visualize segregation of elements near surfaces and interfaces. The segregation is generally the response to chemical or electronic driving

forces, such as the polarization catastrophe discussed in Section 3.3.2. It is also a useful feedback for optimizing growth conditions when stoichiometry or doping distribution needs to be optimized. Moreover, the occupancy can itself shed light on the electronic or chemical behavior of the system, as in the case of the transition metal occupancy in a typical transition metal oxide (see, e.g., Section 3.3.3).

Structurally, many of the common uses of maps provided by CTR analysis have been related to the polar distortions of an interfacial system. The relative z-axis displacement of positive and negative ions in each layer provides a measure of the layer polarization. This type of polar distortion influences the system through the electronic bandwidth (as described in Equation (36)), the orbital polarization if symmetry is broken, and magnetism via super/double-exchange mechanisms. The polarization may also be related to the layer-resolved c-axis unit size, which has been useful for ferroelectric thin films. Again, these polar distortions may arise due to electrostatic changes at boundaries (i.e., surfaces/interfaces). Lateral reconstructions—including dimerization, polyhedral tilts/rotations, and breathing distortions—are other useful motifs discerned from CTR measurements when using superstructure rods in addition to integer-order rods. Such symmetry-breaking reconstructions may lead to significant changes in electronic structure, such as metal–insulator or magnetic transitions. The themes discussed above are summarized in Figure 18.

As a final note, we underscore that due to the relationship between structural parameters and functional properties, CTR scattering fits perfectly into current efforts to engineer materials properties on the atomic scale. Many studies mentioned in this review push in this direction by comparing, for instance, structural changes as a function of film thickness or interface composition. With the ultimate goal of being able to design systems with certain functionalities—be it high-temperature superconductivity, magnetoelectricity, switchable catalysis, or anything else—CTR characterization generally works in conjunction with both theory (to relate structural themes to electronic/magnetic structure) and synthesis (to optimize materials growth). The structural distortions occurring in interfacial systems are typically fractions of angstroms; as such, the term picoscale engineering has been applied to this endeavor.^[1]

4.2. Outlook

While large experimental facilities and complex data analysis techniques are still required to perform and extract the most detailed information from crystal truncation rod scattering measurements, the variety of applications discussed in Section 3 demonstrates that such experiments are beginning to become standard tools for the high-resolution study of surfaces, thin films, and interface structures, in the same manner as electron microscopy and scanning probe techniques like TEM and STM. CTR methods continue to be developed and applied to a wider range of systems and problems. These advancements can be divided into two directions. One is aimed toward extending the applicability of the CTR technique to new regimes—time-scales, environments, and materials. The other broad category

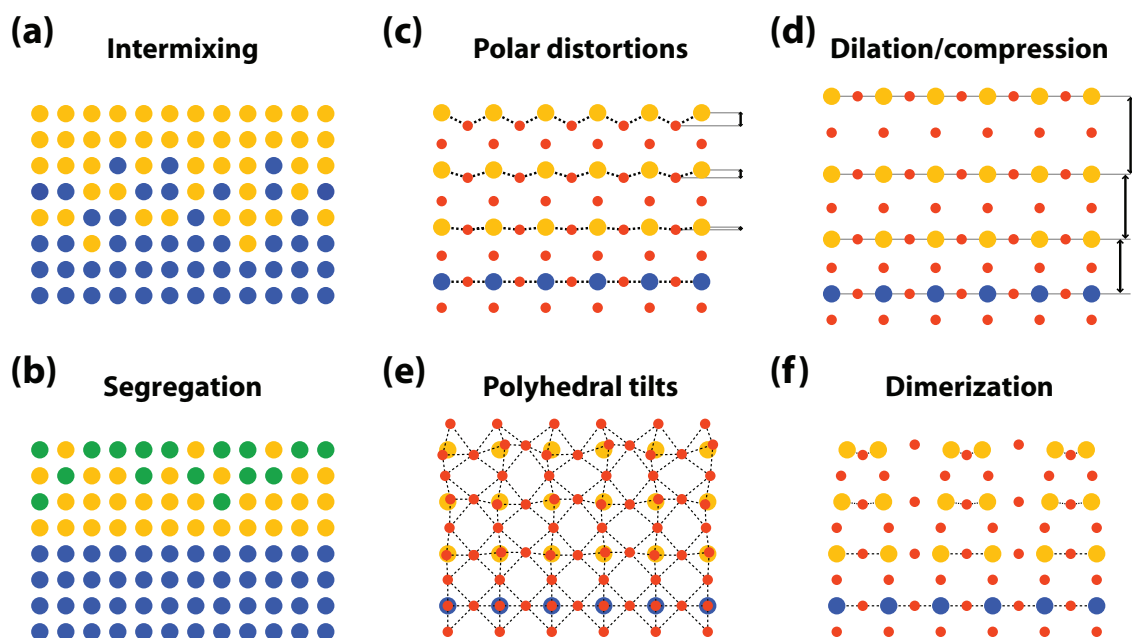


Figure 18. Themes of structural and chemical behavior at surfaces/interfaces extracted from CTR analysis. a,b) Features discernable from analysis of site occupancy. c–f) Types of features observable from analysis of layer-resolved atomic positions. While each type of reconstruction/relaxation is displayed separately, several may be present simultaneously in a real system.

is related to expanding the capabilities of CTR methods by combining it with other techniques, allowing new information to be extracted. We discuss some recent progress in these areas here and draw attention to potential future applications.

The push toward observing phenomena at ultrafast time scales has become an overarching theme in many areas of science. It has been found that ultrashort (sub-picosecond) laser pulses can be used to stimulate materials into nonequilibrium phases whose dynamics can reveal much about the underlying interactions governing these systems.^[224,225] In addition, one can control macroscopic electronic and magnetic properties by driving materials into hidden phases with tailored light pulses.^[226,227] By using ultrashort, intense X-ray pulses from free electron laser sources, one can perform diffraction experiments to probe structural changes on femtosecond time scales;^[228,229] however, such studies have been for the most part applied to bulk materials in which a handful of Bragg reflections are measured. Applying CTR scattering in this context could serve as a powerful tool to understand light-induced dynamics on surfaces, ultrathin layers, and buried interfaces. In the past few years, this prospect has been slowly becoming reality. Coherent diffraction imaging techniques can be used to measure laser-induced dynamics from a single diffraction peak,^[230] and these methods have been extended to reconstruct 1D spatiotemporal magnetization dynamics in a thin film by applying time-based constraints to resonant magnetic scattering data.^[231] In addition, the first femtosecond surface X-ray diffraction experiments were recently carried out on a monolayer chalcogenide, from which both in-plane and out-of-plane structure could be modeled^[223] (see **Figure 19**). Obtaining detailed enough time-resolved CTR measurements to extract, for instance, high-resolution electron density maps remains a challenge; some difficulties include long acquisition times and maintaining laser and X-ray alignment

during CTR mapping. Yet, these obstacles may be soon overcome with the continual development of new detectors, sources, and analyses for ultrafast X-ray diffraction.

For applications of functional materials, it is important to move beyond artificially pristine laboratory environments toward studying them under operational conditions. Furthermore, observing processes during growth may aid in optimizing the fabrication of films and heterostructures for particular behaviors. In situ and in operando CTR experiments have thus become extremely valuable from both a scientific and technological perspective.^[234] In situ growth studies of metals and semiconductors using CTR scattering have a long history since the first measurements of Ge homoepitaxy via MBE by Vlieg et al.^[235] Homo- and heteroepitaxial MBE growth,^[236–240] as well as metal-organic vapor phase epitaxy (MOVPE) growth,^[241–244] have been observed, leading to important basic insights into layer formation and morphology. Growth facilities built at synchrotron beamlines have enabled similar studies of complex oxide growth by MOVPE,^[245,246] PLD,^[247–250] and more recently, MBE,^[232,251–253] revealing, for example, the tendency for certain layered structures to re-arrange during growth^[233,254] and the conditions under which oxygen defect structures are stabilized^[100,255] (see **Figure 20**). In addition to growth, in situ CTR measurements in heterogeneous environments have been carried out on crystalline-gas^[256] and crystalline-liquid interfaces,^[257–272] often relevant for geological and mineralogical studies. Interfacial structures have even been measured in operando during ferroelectric switching^[245,273,274] and during various chemical processes, including electrochemical deposition,^[275–277] electrolytic and catalytic adsorption,^[47,278–282] oxidation/reduction reactions,^[99,279,283–286] and solid oxide fuel cell operation.^[287] These examples leverage the ability of CTR scattering to probe atomic structures of surfaces and buried interfaces nondestructively

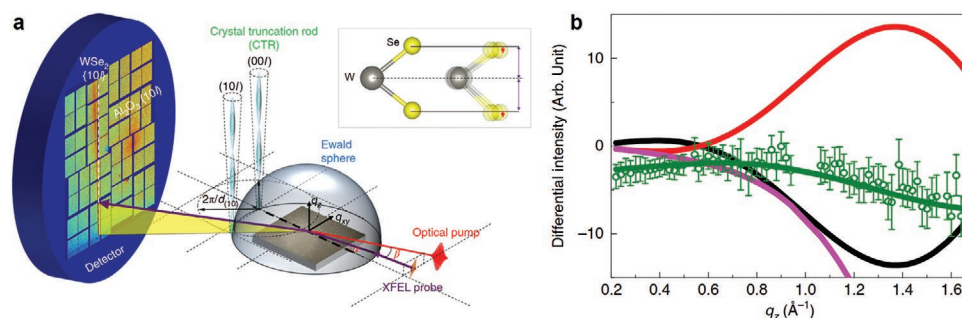


Figure 19. a) Schematic of ultrafast CTR measurement of monolayer WSe₂ on sapphire. b) Differential CTR intensity along the (10L) rod from 5 to 10 ps, subtracted from the static CTR. Solid lines are model calculations. The dynamical structure of the green curve is schematically shown in the inset. Reproduced with permission.^[223] Copyright 2019, Nature Research.

with high resolution and often element specificity. A primary limitation is the time for acquiring high quality CTR data, which, if sped up, would make the technique suitable for more active and dynamical processes. Promising recent approaches use high-energy diffraction^[288] or simultaneous multiwavelength detection^[289] to improve CTR acquisition times.

Over the past decade, several new or upgraded facilities dedicated to soft ($\approx 0.1\text{--}1\text{ keV}$) and “tender” energy X-rays ($\approx 1\text{--}10\text{ keV}$) have spurred a flurry of experiments involving transition metal compounds, especially correlated materials (as discussed in Section 3.3.3. Resonant scattering from magnetic or charge order provides insights into the phase behavior of these materials and can be combined with spectroscopy to inform the site, element, and valence configuration.^[290] Measuring magnetic structures at surfaces by combining resonant and CTR scattering was proposed in the 1990s,^[291] and early experiments focused on elements with valence f electrons,^[292–294] which typically have relatively high energy M-edge transitions. For transition metals, the valence L-edge transitions are usually in the soft X-ray regime, for which allowed scattering vectors are limited and measuring CTRs over a wide range of q_{\parallel} is not

possible. Nevertheless, many recent experiments have deduced layer-resolved magnetic, charge, and orbital order, mainly in thick films and superlattice structures, thanks to a combination of resonant reflectometry and electronic structure modeling. Extending this capability to surfaces and ultrathin layers by incorporating CTR analysis remains a challenge for the future. The development of energy-discriminating 2D detectors would aid in this endeavor by decoupling the fluorescence background from scattered X-rays—a limitation also for non-resonant CTR scattering experiments.

Another important technical advance is the increased spatial coherence of the X-ray sources featured at free electron laser and next-generation synchrotron facilities. As a result, the application of coherent diffraction techniques to image complex structures in materials, such as domain patterns and strain profiles, has burgeoned over the last several years.^[295] These techniques are also beginning to be employed in conjunction with CTR scattering.^[296] Machine learning methods provide new opportunities for model development and data fitting in conventional X-ray and CTR scattering.^[297,298] Building on recent work in image reconstruction^[299] and inverse optical design

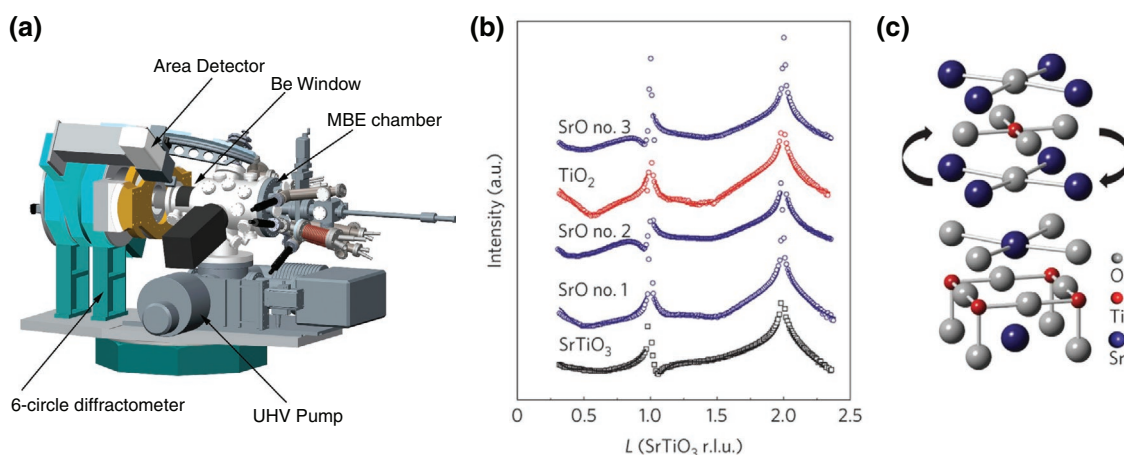


Figure 20. a) Schematic of in situ X-ray scattering MBE growth chamber at the Advanced Photon Source, Beamline 33ID. Reproduced with permission.^[232] Copyright 2016, American Institute of Physics. b) In situ (00L) CTR measurements during layer-by-layer growth of Sr_2TiO_4 . CTR after final SrO layer looks identical to that after the initial double SrO layers, indicating an unintended double SrO layer termination. c) Atomic structure of intended growth sequence and proposed layer rearrangement leading to a double SrO surface termination. b,c) Reproduced with permission.^[233] Copyright 2014, Nature Research.

methods,^[300] deep learning neural networks could be applied in the future to perform phase retrieval from measured CTRs.

Although the CTR technique has a long history, its applications continue to grow, and its ubiquitous use among chemists, physicists, materials scientists, and surface scientists is a testament to its utility and versatility. As new materials are discovered and investigated, CTR scattering will play an integral role in their understanding. The rapidly growing fields of topological and 2D materials, for instance, are ideally studied by these techniques because of the relevance of surface states and the atomic scale thicknesses, respectively. As discussed in the review, there are many systems and problems for which X-ray crystal truncation rod scattering is a uniquely suited tool. It remains a standard for probing atomic and chemical structure of surfaces and interfaces, and as research pushes the spatial and temporal limits of our understanding of materials, CTR scattering will be an invaluable resource for scientific and technological innovation.

Acknowledgements

A.S.D. acknowledges fellowship support from the Alexander von Humboldt Foundation. F.J.W. and C.H.A. acknowledge support for work on this review by the U.S. Department of Energy, Office of Science, Office of Basic Energy Sciences under Award No. DE-SC0019211. F.J.W. also acknowledges helpful discussions over the years with Eliot Specht, Gene Ice, Cullie Sparks, Zhan Zhang, Hawoong Hong, Chris Schlepütz, Jon Tischler, and Paul Zschack. This article is part of the *Advanced Materials Interfaces* Hall of Fame article series, which highlights the work of top interface and surface scientists.

Conflict of Interest

The authors declare no conflict of interest.

Keywords

atomic structure, crystal truncation rod scattering, oxide interfaces, X-ray diffraction

Received: October 21, 2019

Revised: January 21, 2020

Published online: February 20, 2020

- [1] S. Ismail-Beigi, F. J. Walker, A. S. Disa, K. M. Rabe, C. H. Ahn, *Nat. Rev. Mater.* **2017**, 2, 17060.
- [2] I. K. Robinson, *Phys. Rev. B* **1986**, 33, 3830.
- [3] S. R. Andrews, R. A. Cowley, *J. Phys. C: Solid State Phys.* **1985**, 18, 6427.
- [4] Y. Kashiwara, K. Kawamura, N. Kashiwagura, J. Harada, *Jpn. J. Appl. Phys.* **1987**, 26, L1029.
- [5] N. Kashiwagura, Y. Kashiwara, M. Sakata, J. Harada, S. W. Wilkins, A. W. Stevenson, *Jpn. J. Appl. Phys.* **1987**, 26, L2026.
- [6] Q. Shen, J. M. Blakely, M. J. Bedzyk, K. D. Finkelstein, *Phys. Rev. B* **1989**, 40, 3480.
- [7] R. G. van Silfhout, J. F. van der Veen, C. Norris, J. E. Macdonald, *Faraday Discuss. Chem. Soc.* **1990**, 89, 169.
- [8] I. K. Robinson, W. K. Waskiewicz, R. T. Tung, J. Bohr, *Phys. Rev. Lett.* **1986**, 57, 2714.
- [9] G. A. Held, J. L. Jordan-Sweet, P. M. Horn, A. Mak, R. J. Birgeneau, *Phys. Rev. Lett.* **1987**, 59, 2075.
- [10] K. G. Huang, D. Gibbs, D. M. Zehner, A. R. Sandy, S. G. J. Mochrie, *Phys. Rev. Lett.* **1990**, 65, 3313.
- [11] A. R. Sandy, S. G. J. Mochrie, D. M. Zehner, G. Grübel, K. G. Huang, D. Gibbs, *Phys. Rev. Lett.* **1992**, 68, 2192.
- [12] A. R. Sandy, S. G. J. Mochrie, D. M. Zehner, K. G. Huang, D. Gibbs, *Phys. Rev. B* **1991**, 43, 4667.
- [13] X. Torrelles, F. Wendler, O. Bikondoa, H. Isern, W. Moritz, G. R. Castro, *Surf. Sci.* **2001**, 487, 97.
- [14] H. Reichert, P. Eng, H. Dosch, I. Robinson, *Phys. Rev. Lett.* **1995**, 74, 2006.
- [15] R. Feidenhans'l, *Surf. Sci. Rep.* **1989**, 10, 105.
- [16] I. K. Robinson, D. J. Tweet, *Rep. Prog. Phys.* **1992**, 55, 599.
- [17] P. L. Cowan, *Phys. Rev. B* **1985**, 32, 5437.
- [18] P. L. Cowan, S. Brennan, T. Jach, M. J. Bedzyk, G. Materlik, *Phys. Rev. Lett.* **1986**, 57, 2399.
- [19] S. Dietrich, H. Wagner, *Z. Phys. B: Condens. Matter* **1984**, 56, 207.
- [20] P. Eisenberger, W. C. Marra, *Phys. Rev. Lett.* **1981**, 46, 1081.
- [21] W. C. Marra, P. Eisenberger, A. Y. Cho, *J. Appl. Phys.* **1979**, 50, 6927.
- [22] G. H. Vineyard, *Phys. Rev. B* **1982**, 26, 4146.
- [23] J. Bohr, R. Feidenhans'l, M. Nielsen, M. Toney, R. L. Johnson, I. K. Robinson, *Phys. Rev. Lett.* **1985**, 54, 1275.
- [24] R. Feidenhans'l, J. S. Pedersen, M. Nielsen, F. Grey, R. L. Johnson, *Surf. Sci.* **1986**, 178, 927.
- [25] M. D. Foster, *Crit. Rev. Anal. Chem.* **2006**, 24, 179.
- [26] P. H. Fuoss, L. J. Norton, S. Brennan, A. Fischer-Colbrie, *Phys. Rev. Lett.* **1988**, 60, 600.
- [27] W. C. Marra, P. H. Fuoss, P. E. Eisenberger, *Phys. Rev. Lett.* **1982**, 49, 1169.
- [28] R. Feidenhans'l, F. Grey, R. L. Johnson, S. G. J. Mochrie, J. Bohr, M. Nielsen, *Phys. Rev. B* **1990**, 41, 5420.
- [29] H. Zhou, R. Pindak, R. Clarke, D. M. Steinberg, Y. Yacoby, *J. Phys. D: Appl. Phys.* **2012**, 45, 195302.
- [30] A. B. Yankovich, B. Berkels, W. Dahmen, P. Binev, S. I. Sanchez, S. A. Bradley, A. Li, I. Szlufarska, P. M. Voyles, *Nat. Commun.* **2014**, 5, 4415.
- [31] T. H. Kim, D. Puggioni, Y. Yuan, L. Xie, H. Zhou, N. Campbell, P. J. Ryan, Y. Choi, J. W. Kim, J. R. Patzner, S. Ryu, J. P. Podkaminer, J. Irwin, Y. Ma, C. J. Fennie, M. S. Rzechowski, X. Q. Pan, V. Gopalan, J. M. Rondinelli, C. B. Eom, *Nature* **2016**, 533, 68.
- [32] Z. Liao, M. Huijben, Z. Zhong, N. Gauquelin, S. Macke, R. J. Green, S. Van Aert, J. Verbeeck, G. Van Tendeloo, K. Held, G. A. Sawatzky, G. Koster, G. Rijnders, *Nat. Mater.* **2016**, 15, 425.
- [33] D. Yi, C. L. Flint, P. P. Balakrishnan, K. Mahalingam, B. Urwin, A. Vailionis, A. T. N'Diaye, P. Shafer, E. Arenholz, Y. Choi, K. H. Stone, J.-H. Chu, B. M. Howe, J. Liu, I. R. Fisher, Y. Suzuki, *Phys. Rev. Lett.* **2017**, 119, 077201.
- [34] J. Als-Nielsen, D. McMorrow, *Elements of Modern X-ray Physics*, 2nd ed., Wiley, Hoboken **2011**.
- [35] B. L. Henke, E. M. Gullikson, J. C. Davis, *At. Data Nucl. Data Tables* **1993**, 54, 181.
- [36] R. Colella, *Phys. Rev. B* **1991**, 43, 13827.
- [37] T. S. Gau, S. L. Chang, *Acta Crystallogr., Sect. A: Found. Crystallogr.* **1995**, 51, 920.
- [38] V. Holý, P. F. Fewster, *J. Appl. Crystallogr.* **2008**, 41, 18.
- [39] V. M. Kaganer, *Phys. Rev. B* **2007**, 75, 245425.
- [40] T. Takahashi, S. Nakatani, *Surf. Sci.* **1995**, 326, 347.
- [41] H. Dosch, *Phys. Rev. B* **1987**, 35, 2137.
- [42] G. Renaud, R. Lazzari, F. Leroy, *Surf. Sci. Rep.* **2009**, 64, 255.
- [43] *Resonant Anomalous X-ray Scattering: Theory and Applications* (Eds: G. Materlik, C. J. Sparks, K. Fischer), North-Holland, Amsterdam **1994**.

- [44] J.-L. Hodeau, V. Favre-Nicolin, S. Bos, H. Renevier, E. Lorenzo, J.-F. Berar, *Chem. Rev.* **2001**, 101, 1843.
- [45] E. D. Specht, F. J. Walker, *Phys. Rev. B* **1993**, 47, 13743.
- [46] C. Park, P. A. Fenter, *J. Appl. Crystallogr.* **2007**, 40, 290.
- [47] A. Menzel, K.-C. Chang, V. Komanicky, H. You, Y. S. Chu, Y. V. Tolmachev, J. J. Rehr, *Radiat. Phys. Chem.* **2006**, 75, 1651.
- [48] V. Vonk, *J. Appl. Crystallogr.* **2011**, 44, 1217.
- [49] S. A. Pauli, S. J. Leake, M. Björck, P. R. Willmott, *J. Phys.: Condens. Matter* **2012**, 24, 305002.
- [50] B. D. Patterson, C. Brönnimann, D. Maden, F. Gozzo, A. Groso, B. Schmitt, M. Stamparoni, P. R. Willmott, *Nucl. Instrum. Methods Phys. Res., Sect. B* **2005**, 238, 224.
- [51] O. H. Seeck, C. Deiter, K. Pflaum, F. Bertam, A. Beerlink, H. Franz, J. Horbach, H. Schulte-Schrepping, B. M. Murphy, M. Greve, O. Magnussen, *J. Synchrotron Radiat.* **2011**, 19, 30.
- [52] O. Sakata, Y. Furukawa, S. Goto, T. Mochizuki, T. Uruga, K. Takeshita, H. Ohashi, T. Ohata, T. Matsushita, S. Takahashi, H. Tajiri, T. Ishikawa, M. Nakamura, M. Ito, K. Sumitani, T. Takahashi, T. Shimura, A. Saito, M. Takahasi, *Surf. Rev. Lett.* **2012**, 10, 543.
- [53] D. H. Bilderback, P. Elleaume, E. Weckert, *J. Phys. B: At., Mol. Opt. Phys.* **2005**, 38, S773.
- [54] A. C. Thompson, D. T. Attwood, E. M. Gullikson, J. B. Howells, J. B. Kortright, A. L. Robinson, J. H. Underwood, K.-J. Kim, J. Kirz, I. Lindau, P. Pianetta, H. Winick, G. P. Williams, J. H. Scofield, *X-Ray Data Booklet*, 2nd ed., Lawrence Berkeley National Laboratory, Berkeley **2001**.
- [55] Y. Shvyd'ko, *X-Ray Optics: High-Energy-Resolution Applications*, Vol. 98, Springer, Heidelberg **2013**.
- [56] G. E. Ice, *X-Ray Spectrom.* **1997**, 26, 315.
- [57] E. D. Specht, F. J. Walker, *J. Appl. Crystallogr.* **1993**, 26, 166.
- [58] E. Vlieg, *J. Appl. Crystallogr.* **1997**, 30, 532.
- [59] P. Fenter, J. G. Catalano, C. Park, Z. Zhang, *J. Synchrotron Radiat.* **2006**, 13, 293.
- [60] H. You, *J. Appl. Crystallogr.* **1999**, 32, 614.
- [61] C. M. Schlepütz, R. Herger, P. R. Willmott, B. D. Patterson, O. Bunk, C. Brönnimann, B. Henrich, G. Hülsen, E. F. Eikenberry, *Acta Crystallogr., Sect. A: Found. Crystallogr.* **2005**, 61, 418.
- [62] G. Thorkildsen, R. H. Mathiesen, H. B. Larsen, *J. Appl. Crystallogr.* **1999**, 32, 943.
- [63] C. M. Schlepütz, S. O. Mariager, S. A. Pauli, R. Feidenhans'l, P. R. Willmott, *J. Appl. Crystallogr.* **2010**, 44, 73.
- [64] W. R. Busing, H. A. Levy, *Acta Crystallogr.* **1967**, 22, 457.
- [65] T. Shimura, J. Harada, *J. Appl. Crystallogr.* **1993**, 26, 151.
- [66] J. Drnec, T. Zhou, S. Pintea, W. Onderwaater, E. Vlieg, G. Renaud, R. Felici, *J. Appl. Crystallogr.* **2014**, 47, 365.
- [67] A. Gibaud, G. Vignaud, S. K. Sinha, *Acta Crystallogr., Sect. A: Found. Crystallogr.* **1993**, 49, 642.
- [68] G. N. Murshudov, A. A. Vagin, E. J. Dodson, *Acta Crystallogr., Sect. D: Biol. Crystallogr.* **1997**, 53, 240.
- [69] E. Prince, Ed., *International Tables for Crystallography, Volume C: Mathematical, Physical and Chemical Tables*, 3rd ed., Wiley, Dordrecht **2004**.
- [70] D. Watkin, *J. Appl. Crystallogr.* **2008**, 41, 491.
- [71] E. Vlieg, *J. Appl. Crystallogr.* **2000**, 33, 401.
- [72] M. Björck, G. Andersson, *J. Appl. Crystallogr.* **2007**, 40, 1174.
- [73] J. R. Fienup, *Opt. Lett.* **1978**, 3, 27.
- [74] L. D. Marks, W. Sinkler, E. Landree, *Acta Crystallogr., Sect. A: Found. Crystallogr.* **1999**, 55, 601.
- [75] L. D. Marks, E. Bengu, C. Collazo-Davila, D. Grozea, E. Landree, C. Leslie, W. Sinkler, *Surf. Rev. Lett.* **1998**, 05, 1087.
- [76] L. D. Marks, *Phys. Rev. B* **1999**, 60, 2771.
- [77] L. D. Marks, N. Erdman, A. Subramanian, *J. Phys.: Condens. Matter* **2001**, 13, 10677.
- [78] N. Erdman, K. R. Poeppelmeier, M. Asta, O. Warschkow, D. E. Ellis, L. D. Marks, *Nature* **2002**, 419, 55.
- [79] Y. Yacoby, R. Pindak, R. MacHarrie, L. Pfeiffer, L. Berman, R. Clarke, *J. Phys.: Condens. Matter* **2000**, 12, 3929.
- [80] Y. Yacoby, M. Sowwan, E. Stern, J. O. Cross, D. Brewre, R. Pindak, J. Pitney, E. M. Dufresne, R. Clarke, *Nat. Mater.* **2002**, 1, 99.
- [81] P. R. Willmott, S. A. Pauli, R. Herger, C. M. Schlepütz, D. Martoccia, B. D. Patterson, B. Delley, R. Clarke, D. Kumah, C. Cionca, Y. Yacoby, *Phys. Rev. Lett.* **2007**, 99, 155502.
- [82] D. K. Saldin, V. L. Shneerson, R. Fung, *Phys. B* **2003**, 336, 16.
- [83] R. Fung, V. L. Shneerson, P. F. Lyman, S. S. Parihar, H. T. Johnson-Steigleman, D. K. Saldin, *Acta Crystallogr., Sect. A: Found. Crystallogr.* **2007**, 63, 239.
- [84] T. Shirasawa, M. Sugiki, T. Hirahara, M. Aitani, T. Shirai, S. Hasegawa, T. Takahashi, *Phys. Rev. B* **2014**, 89, 195311.
- [85] T. Shirasawa, J. Tsunoda, T. Hirahara, T. Takahashi, *Phys. Rev. B* **2013**, 87, 075449.
- [86] V. Elser, *Acta Crystallogr., Sect. A: Found. Crystallogr.* **2003**, 59, 201.
- [87] V. Elser, *J. Phys. A: Math. Gen.* **2003**, 36, 2995.
- [88] V. Elser, *J. Opt. Soc. Am. A* **2003**, 20, 40.
- [89] M. Björck, C. M. Schlepütz, S. A. Pauli, D. Martoccia, R. Herger, P. R. Willmott, *J. Phys.: Condens. Matter* **2008**, 20, 445006.
- [90] P. F. Lyman, V. L. Shneerson, R. Fung, R. J. Harder, E. D. Lu, S. S. Parihar, D. K. Saldin, *Phys. Rev. B* **2005**, 71, 081402.
- [91] A. T. Brünger, *Nature* **1992**, 355, 472.
- [92] S. Geller, *Acta Crystallogr.* **1967**, 14, 1026.
- [93] Y. Yuan, Y. Lu, G. Stone, K. Wang, C. M. Brooks, D. G. Schlom, S. B. Sinnott, H. Zhou, V. Gopalan, *Nat. Commun.* **2018**, 9, 5220.
- [94] M. Brehm, H. Groiss, G. Bauer, D. Gerthsen, R. Clarke, Y. Paltiel, Y. Yacoby, *Nanotechnology* **2015**, 26, 485702.
- [95] L. Horák, D. Krieger, J. Liu, C. Frontera, X. Marti, V. Holý, *J. Appl. Crystallogr.* **2017**, 50, 385.
- [96] S. Koohfar, A. S. Disa, M. S. J. Marshall, F. J. Walker, C. H. Ahn, D. P. Kumah, *Phys. Rev. B* **2017**, 96, 024108.
- [97] S. Koohfar, A. B. Georgescu, A. N. Penn, J. M. LeBeau, E. Arenholz, D. P. Kumah, *npj Quantum Mater.* **2019**, 4, 1.
- [98] H. Lee, N. Campbell, J. Lee, T. J. Asel, T. R. Paudel, H. Zhou, J. W. Lee, B. Noesges, J. Seo, B. Park, L. J. Brillson, S. H. Oh, E. Y. Tsybal, M. S. Rzechowski, C. B. Eom, *Nat. Mater.* **2018**, 17, 231.
- [99] Y. Liu, A. Barbour, V. Komanicky, H. You, *J. Phys. Chem. C* **2016**, 120, 16174.
- [100] I. C. Tung, G. Luo, J. H. Lee, S. H. Chang, J. Moyer, H. Hong, M. J. Bedzyk, H. Zhou, D. Morgan, D. D. Fong, J. W. Freeland, *Phys. Rev. Mater.* **2017**, 1, 053404.
- [101] H. You, U. Welp, G. W. Crabtree, Y. Fang, S. K. Sinha, J. D. Axe, X. Jiang, S. C. Moss, *Phys. Rev. B* **1992**, 45, 5107.
- [102] U. Diebold, *Surf. Sci. Rep.* **2003**, 48, 53.
- [103] G. Charlton, P. B. Howes, C. L. Nicklin, P. Steadman, J. S. G. Taylor, C. A. Muryn, S. P. Harte, J. Mercer, R. McGrath, D. Norman, T. S. Turner, G. Thornton, *Phys. Rev. Lett.* **1997**, 78, 495.
- [104] G. Charlton, P. B. Howes, C. A. Muryn, H. Raza, N. Jones, J. S. G. Taylor, C. Norris, R. McGrath, D. Norman, T. S. Turner, G. Thornton, *Phys. Rev. B* **2000**, 61, 16117.
- [105] R. Lindsay, A. Wander, A. Ernst, B. Montanari, G. Thornton, N. M. Harrison, *Phys. Rev. Lett.* **2005**, 94, 246102.
- [106] G. S. Parkinson, M. A. Muñoz Márquez, P. D. Quinn, M. J. Gladys, R. E. Tanner, D. P. Woodruff, P. Bailey, T. C. Q. Noakes, *Phys. Rev. B* **2006**, 73, 245409.
- [107] W. Busayaporn, X. Torrelles, A. Wander, S. Tomic', A. Ernst, B. Montanari, N. M. Harrison, O. Bikondoa, I. Jourard, J. Zegenhagen, G. Cabailh, G. Thornton, R. Lindsay, *Phys. Rev. B* **2010**, 81, 153404.
- [108] G. Cabailh, X. Torrelles, R. Lindsay, O. Bikondoa, I. Jourard, J. Zegenhagen, G. Thornton, *Phys. Rev. B* **2007**, 75, 241403.
- [109] X.-Q. Gong, N. Khorshidi, A. Stierle, V. Vonk, C. Ellinger, H. Dosch, H. Cheng, A. Selloni, Y. He, O. Dulub, U. Diebold, *Surf. Sci.* **2009**, 603, 138.

- [110] X. Torrelles, G. Cabailh, R. Lindsay, O. Bikondoa, J. Roy, J. Zegenhagen, G. Teobaldi, W. A. Hofer, G. Thornton, *Phys. Rev. Lett.* **2008**, *101*, 185501.
- [111] O. Robach, G. Renaud, A. Barbier, *Surf. Sci.* **1998**, *401*, 227.
- [112] P. J. Eng, T. P. Trainor, G. E. Brown, G. A. Waychunas, M. Newville, S. R. Sutton, M. L. Rivers, *Science* **2000**, *288*, 1029.
- [113] T. P. Trainor, P. J. Eng, G. E. Brown, I. K. Robinson, M. D. Santis, *Surf. Sci.* **2002**, *496*, 238.
- [114] G. Charlton, S. Brennan, C. A. Muryn, R. McGrath, D. Norman, T. S. Turner, G. Thornton, *Surf. Sci.* **2000**, *457*, L376.
- [115] R. Herger, P. R. Willmott, O. Bunk, C. M. Schlepütz, B. D. Patterson, B. Delley, *Phys. Rev. Lett.* **2007**, *98*, 076102.
- [116] R. Herger, P. R. Willmott, O. Bunk, C. M. Schlepütz, B. D. Patterson, B. Delley, V. L. Shneerson, P. F. Lyman, D. K. Saldin, *Phys. Rev. B* **2007**, *76*, 195435.
- [117] C. Noguera, *J. Phys.: Condens. Matter* **2000**, *12*, R367.
- [118] V. E. Henrich, P. A. Cox, *The Surface Science of Metal Oxides*, Cambridge University Press, Cambridge, New York **1994**.
- [119] F. Finocchi, A. Barbier, J. Jupille, C. Noguera, *Phys. Rev. Lett.* **2004**, *92*, 136101.
- [120] D. Wolf, *Phys. Rev. Lett.* **1992**, *68*, 3315.
- [121] A. Barbier, C. Mocuta, H. Kuhlbeck, K. F. Peters, B. Richter, G. Renaud, *Phys. Rev. Lett.* **2000**, *84*, 2897.
- [122] A. Barbier, C. Mocuta, G. Renaud, *Phys. Rev. B* **2000**, *62*, 16056.
- [123] A. Wander, F. Schedin, P. Steadman, A. Norris, R. McGrath, T. S. Turner, G. Thornton, N. M. Harrison, *Phys. Rev. Lett.* **2001**, *86*, 3811.
- [124] C. M. Schlepütz, Y. Yang, N. S. Hussein, R. Heinhold, H.-S. Kim, M. W. Allen, S. M. Durbin, R. Clarke, *J. Phys.: Condens. Matter* **2012**, *24*, 095007.
- [125] R. Francis, S. Moss, A. Jacobson, *Phys. Rev. B* **2001**, *64*, 235425.
- [126] J. E. Kleibecker, B. Kuiper, S. Harkema, D. H. A. Blank, G. Koster, G. Rijnders, P. Tinnemans, E. Vlieg, P. B. Rossen, W. Siemons, G. Portale, J. Ravichandran, J. M. Szeplieniec, R. Ramesh, *Phys. Rev. B* **2012**, *85*, 165413.
- [127] I. K. Robinson, R. T. Tung, R. Feidenhans'l, *Phys. Rev. B* **1988**, *38*, 3632.
- [128] F. Walker, E. Specht, R. McKee, *Phys. Rev. Lett.* **1991**, *67*, 2818.
- [129] H. Hong, R. D. Aburano, D. S. Lin, H. Chen, T. C. Chiang, P. Zschack, E. D. Specht, *Phys. Rev. Lett.* **1992**, *68*, 507.
- [130] K. Sumitani, K. Masuzawa, T. Hoshino, S. Nakatani, T. Takahashi, H. Tajiri, K. Akimoto, H. Sugiyama, X.-W. Zhang, H. Kawata, *Appl. Surf. Sci.* **2006**, *252*, 5288.
- [131] C. A. Lucas, D. Loretto, *Appl. Phys. Lett.* **1992**, *60*, 2071.
- [132] G. C. L. Wong, C. A. Lucas, D. Loretto, A. P. Payne, P. H. Fuoss, *Phys. Rev. Lett.* **1994**, *73*, 991.
- [133] Z. Kovats, M. Rauscher, H. Metzger, J. Peisl, R. Paniago, H.-D. Pfannes, J. Schulze, I. Eisele, F. Boscherini, S. Ferrer, *Phys. Rev. B* **2000**, *62*, 8223.
- [134] H. C. Kang, D. Y. Noh, *J. Appl. Phys.* **2005**, *98*, 044908.
- [135] T. Takahashi, T. Shirasawa, K. Sekiguchi, W. Voegeli, *e-J. Surf. Sci. Nanotechnol.* **2009**, *7*, 525.
- [136] E. D. Specht, G. E. Ice, C. J. Peters, C. J. Sparks, N. Lucas, X. M. Zhu, R. Moret, H. Morkoç, *Phys. Rev. B* **1991**, *43*, 12425.
- [137] K. Sumitani, T. Takahashi, S. Nakatani, A. Nojima, O. Sakata, Y. Yoda, S. Koh, T. Irisawa, Y. Shiraki, *Jpn. J. Appl. Phys.* **2003**, *42*, L189.
- [138] Y. Yacoby, N. Elfassy, S. K. Ray, R. K. Singha, S. Das, E. Cohen, S. Yochelis, R. Clarke, Y. Paltiel, *J. Nanopart. Res.* **2013**, *15*, 1608.
- [139] I. K. Robinson, P. A. Bennett, F. J. Himpsel, *Phys. Rev. Lett.* **2002**, *88*, 096104.
- [140] D. J. Tweet, K. Akimoto, T. Tatsumi, I. Hirose, J. Mizuki, J. Matsui, *Phys. Rev. Lett.* **1992**, *69*, 2236.
- [141] T. Shirasawa, M. Ohyama, W. Voegeli, T. Takahashi, *Phys. Rev. B* **2011**, *84*, 075411.
- [142] C. A. Lucas, P. D. Hatton, S. Bates, T. W. Ryan, S. Miles, B. K. Tanner, *J. Appl. Phys.* **1988**, *63*, 1936.
- [143] G. Ju, Y. Honda, M. Tabuchi, Y. Takeda, H. Amano, *J. Appl. Phys.* **2014**, *115*, 094906.
- [144] C. Ryang Wie, *Mater. Sci. Eng., R* **1994**, *13*, 1.
- [145] M. Tabuchi, K. Fujibayashi, N. Yamada, K. Hagiwara, A. Kobashi, T. Iguchi, Y. Takeda, H. Kamei, *J. Cryst. Growth* **1998**, *186*, 48.
- [146] M. Tabuchi, K. Fujibayashi, N. Yamada, Y. Takeda, H. Kamei, *J. Appl. Phys.* **1997**, *81*, 112.
- [147] M. Tabuchi, Y. Takeda, *J. Cryst. Growth* **2007**, *298*, 12.
- [148] M. Tabuchi, M. Araki, Y. Takeda, *Jpn. J. Appl. Phys.* **2002**, *41*, 1090.
- [149] M. Tabuchi, N. Matsumoto, Y. Takeda, T. Tetsuya, H. Amano, I. Akasaki, *J. Cryst. Growth* **1998**, *189–190*, 291.
- [150] M. Tabuchi, Y. Takeda, N. Matsumoto, H. Amano, I. Akasaki, *Jpn. J. Appl. Phys.* **1999**, *38*, 281.
- [151] M. Tabuchi, Y. Takeda, Y. Sakuraba, T. Kumamoto, K. Fujibayashi, I. Takahashi, J. Harada, H. Kamei, *J. Cryst. Growth* **1995**, *146*, 148.
- [152] Y. Takeda, K. Fujita, N. Matsubara, N. Yamada, S. Ichiki, M. Tabuchi, Y. Fujiwara, *J. Appl. Phys.* **1997**, *82*, 635.
- [153] Y. Takeda, Y. Sakuraba, K. Fujibayashi, M. Tabuchi, T. Kumamoto, I. Takahashi, J. Harada, H. Kamei, *Appl. Phys. Lett.* **1995**, *66*, 332.
- [154] C. N. Cionca, D. A. Walko, Y. Yacoby, C. Dorin, J. Mirecki Millunchick, R. Clarke, *Phys. Rev. B* **2007**, *75*, 115306.
- [155] D. P. Kumah, A. Ripoan, C. N. Cionca, N. S. Hussein, R. Clarke, J. Y. Lee, J. M. Millunchick, Y. Yacoby, C. M. Schlepütz, M. Björck, P. R. Willmott, *Appl. Phys. Lett.* **2008**, *93*, 081910.
- [156] C. N. Cionca, A. Ripoan, D. P. Kumah, N. S. Hussein, D. A. Walko, Y. Yacoby, J. M. Millunchick, R. Clarke, *Appl. Phys. Lett.* **2008**, *92*, 151914.
- [157] E. Cohen, N. Elfassy, G. Koplovitz, S. Yochelis, S. Shusterman, D. P. Kumah, Y. Yacoby, R. Clarke, Y. Paltiel, *Sensors* **2011**, *11*, 10624.
- [158] E. Cohen, S. Yochelis, O. Westreich, S. Shusterman, D. P. Kumah, R. Clarke, Y. Yacoby, Y. Paltiel, *Appl. Phys. Lett.* **2011**, *98*, 243115.
- [159] D. P. Kumah, J. H. Wu, N. S. Hussein, V. D. Dasika, R. S. Goldman, Y. Yacoby, R. Clarke, *Appl. Phys. Lett.* **2011**, *98*, 021903.
- [160] D. P. Kumah, S. Shusterman, Y. Paltiel, Y. Yacoby, R. Clarke, *Nat. Nanotechnol.* **2009**, *4*, 835.
- [161] J. F. Scott, *Science* **2007**, *315*, 954.
- [162] J. Junquera, P. Ghosez, *Nature* **2003**, *422*, 506.
- [163] T. Tybell, C. H. Ahn, J. M. Triscone, *Appl. Phys. Lett.* **1999**, *75*, 856.
- [164] K. J. Choi, *Science* **2004**, *306*, 1005.
- [165] C. Thompson, C. M. Foster, J. A. Eastman, G. B. Stephenson, *Appl. Phys. Lett.* **1997**, *71*, 3516.
- [166] D. D. Fong, C. Cionca, Y. Yacoby, G. B. Stephenson, J. A. Eastman, P. H. Fuoss, S. K. Streiffer, C. Thompson, R. Clarke, R. Pindak, E. A. Stern, *Phys. Rev. B* **2005**, *71*, 144112.
- [167] D. D. Fong, A. M. Kolpak, J. A. Eastman, S. K. Streiffer, P. H. Fuoss, G. B. Stephenson, C. Thompson, D. M. Kim, K. J. Choi, C. B. Eom, I. Grinberg, A. M. Rappe, *Phys. Rev. Lett.* **2006**, *96*, 127601.
- [168] Y. Yacoby, Y. Girshberg, E. A. Stern, R. Clarke, *Phys. Rev. B* **2006**, *74*, 104113.
- [169] Y. Yacoby, C. Brooks, D. Schlom, J. O. Cross, D. A. Walko, C. N. Cionca, N. S. Hussein, A. Ripoan, R. Clarke, *Phys. Rev. B* **2008**, *77*, 195426.
- [170] D. P. Kumah, Y. Yacoby, S. A. Pauli, P. R. Willmott, R. Clarke, *APL Mater.* **2013**, *1*, 062107.
- [171] A. Ohtomo, H. Y. Hwang, *Nature* **2004**, *427*, 423.
- [172] N. Reyren, S. Thiel, A. D. Caviglia, L. F. Kourkoutis, G. Hammerl, C. Richter, C. W. Schneider, T. Kopp, A. S. Ruetschi, D. Jaccard, M. Gabay, D. A. Muller, J. M. Triscone, J. Mannhart, *Science* **2007**, *317*, 1196.
- [173] A. Brinkman, M. Huijben, M. van Zalk, J. Huijben, U. Zeitler, J. C. Maan, W. G. van der Wiel, G. Rijnders, D. H. A. Blank, H. Hilgenkamp, *Nat. Mater.* **2007**, *6*, 493.

- [174] S. Stemmer, S. James Allen, *Annu. Rev. Mater. Res.* **2014**, *44*, 151.
- [175] Y. Wakabayashi, Y. Yamasaki, C. Bell, Y. Hikita, H. Y. Hwang, T. Kimura, *J. Phys.: Conf. Ser.* **2011**, *320*, 012074.
- [176] S. A. Pauli, S. J. Leake, B. Delley, M. Björck, C. W. Schneider, C. M. Schlepütz, D. Martoccia, S. Paetel, J. Mannhart, P. R. Willmott, *Phys. Rev. Lett.* **2011**, *106*, 036101.
- [177] C. Cancellieri, D. Fontaine, S. Gariglio, N. Reyren, A. D. Caviglia, A. Fête, S. J. Leake, S. A. Pauli, P. R. Willmott, M. Stengel, P. Ghosez, J. M. Triscone, *Phys. Rev. Lett.* **2011**, *107*, 056102.
- [178] R. Yamamoto, C. Bell, Y. Hikita, H. Y. Hwang, H. Nakamura, T. Kimura, Y. Wakabayashi, *Phys. Rev. Lett.* **2011**, *107*, 036104.
- [179] T. T. Fister, H. Zhou, Z. Luo, S. S. A. Seo, S. O. Hruszkewycz, D. L. Proffitt, J. A. Eastman, P. H. Fuoss, P. M. Baldo, H. N. Lee, D. D. Fong, *APL Mater.* **2014**, *2*, 021102.
- [180] E. Dagotto, *Science* **2005**, *309*, 257.
- [181] M. Huijben, L. W. Martin, Y. H. Chu, M. B. Holcomb, P. Yu, G. Rijnders, D. H. A. Blank, R. Ramesh, *Phys. Rev. B* **2008**, *78*, 094413.
- [182] J. Z. Sun, D. W. Abraham, R. A. Rao, C. B. Eom, *Appl. Phys. Lett.* **1999**, *74*, 3017.
- [183] R. Herger, P. R. Willmott, C. M. Schlepütz, M. Björck, S. A. Pauli, D. Martoccia, B. D. Patterson, D. Kumah, R. Clarke, Y. Yacoby, M. Döbeli, *Phys. Rev. B* **2008**, *77*, 085401.
- [184] Y. Yamasaki, D. Okuyama, M. Nakamura, T.-h. Arima, M. Kawasaki, Y. Tokura, T. Kimura, Y. Wakabayashi, *J. Phys. Soc. Jpn.* **2011**, *80*, 073601.
- [185] E. J. Moon, R. Colby, Q. Wang, E. Karapetrova, C. M. Schlepütz, M. R. Fitzsimmons, S. J. May, *Nat. Commun.* **2014**, *5*, 5710.
- [186] Y. Ohta, T. Tohyama, S. Maekawa, *Phys. Rev. B* **1991**, *43*, 2968.
- [187] E. Pavarini, I. Dasgupta, T. Saha-Dasgupta, O. Jepsen, O. K. Andersen, *Phys. Rev. Lett.* **2001**, *87*, 047003.
- [188] C. M. Schlepütz, M. Björck, E. Koller, S. A. Pauli, D. Martoccia, O. Fischer, P. R. Willmott, *Phys. Rev. B* **2010**, *81*, 174520.
- [189] Y. Yacoby, H. Zhou, R. Pindak, I. Božović, *Phys. Rev. B* **2013**, *87*, 014108.
- [190] H. Zhou, Y. Yacoby, V. Y. Butko, G. Logvenov, I. Bozovic, R. Pindak, *Proc. Natl. Acad. Sci. USA* **2010**, *107*, 8103.
- [191] A. Gozar, G. Logvenov, L. F. Kourkoutis, A. T. Bollinger, L. A. Giannuzzi, D. A. Muller, I. Bozovic, *Nature* **2008**, *455*, 782.
- [192] S. Catalano, M. Gibert, J. Fowlie, J. Íñiguez, J. M. Triscone, J. Kreisel, *Rep. Prog. Phys.* **2018**, *81*, 046501.
- [193] J. Chaloupka, G. Khaliullin, *Phys. Rev. Lett.* **2008**, *100*, 016404.
- [194] R. Scherwitzl, S. Gariglio, M. Gabay, P. Zubko, M. Gibert, J. M. Triscone, *Phys. Rev. Lett.* **2011**, *106*, 246403.
- [195] J. Son, P. Moetaek, J. M. LeBeau, D. Ouellette, L. Balents, S. J. Allen, S. Stemmer, *Appl. Phys. Lett.* **2010**, *96*, 062114.
- [196] H. Chen, D. P. Kumah, A. S. Disa, F. J. Walker, C. H. Ahn, S. Ismail-Beigi, *Phys. Rev. Lett.* **2013**, *110*, 186402.
- [197] D. P. Kumah, A. S. Disa, J. H. Ngai, H. Chen, A. Malashevich, J. W. Reiner, S. Ismail-Beigi, F. J. Walker, C. H. Ahn, *Adv. Mater.* **2014**, *26*, 1935.
- [198] D. P. Kumah, A. Malashevich, A. S. Disa, D. A. Arena, F. J. Walker, S. Ismail-Beigi, C. H. Ahn, *Phys. Rev. Appl.* **2014**, *2*, 054004.
- [199] B. B. Nelson-Cheeseman, H. Zhou, P. V. Balachandran, G. Fabbri, J. Hoffman, D. Haskel, J. M. Rondinelli, A. Bhattacharya, *Adv. Funct. Mater.* **2014**, *24*, 6884.
- [200] A. S. Disa, D. P. Kumah, A. Malashevich, H. Chen, D. A. Arena, E. D. Specht, S. Ismail-Beigi, F. J. Walker, C. H. Ahn, *Phys. Rev. Lett.* **2015**, *114*, 026801.
- [201] S. J. May, J. W. Kim, J. M. Rondinelli, E. Karapetrova, N. A. Spaldin, A. Bhattacharya, P. J. Ryan, *Phys. Rev. B* **2010**, *82*, 014110.
- [202] Z. Feng, Y. Yacoby, W. T. Hong, H. Zhou, M. D. Biegalski, H. M. Christen, Y. Shao-Horn, *Energy Environ. Sci.* **2014**, *7*, 1166.
- [203] H. Jeon, W. S. Choi, M. D. Biegalski, C. M. Folkman, I. C. Tung, D. D. Fong, J. W. Freeland, D. Shin, H. Ohta, M. F. Chisholm, H. N. Lee, *Nat. Mater.* **2013**, *12*, 1057.
- [204] J. Suntivich, H. A. Gasteiger, N. Yabuuchi, H. Nakanishi, J. B. Goodenough, Y. Shao-Horn, *Nat. Chem.* **2011**, *3*, 546.
- [205] G. J. la O', S.-J. Ahn, E. Crumlin, Y. Orikasa, M. Biegalski, H. Christen, Y. Shao-Horn, *Angew. Chem., Int. Ed.* **2010**, *49*, 5344.
- [206] Z. Feng, Y. Yacoby, M. J. Gadre, Y.-L. Lee, W. T. Hong, H. Zhou, M. D. Biegalski, H. M. Christen, S. B. Adler, D. Morgan, Y. Shao-Horn, *J. Phys. Chem. Lett.* **2014**, *5*, 1027.
- [207] J. W. Reiner, A. M. Kolpak, Y. Segal, K. F. Garrity, S. Ismail-Beigi, C. H. Ahn, F. J. Walker, *Adv. Mater.* **2010**, *22*, 2919.
- [208] R. A. McKee, F. J. Walker, M. F. Chisholm, *Phys. Rev. Lett.* **1998**, *81*, 3014.
- [209] Y. Segal, J. W. Reiner, A. M. Kolpak, Z. Zhang, S. Ismail-Beigi, C. H. Ahn, F. J. Walker, *Phys. Rev. Lett.* **2009**, *102*, 116101.
- [210] J. W. Reiner, Y. Segal, K. F. Garrity, H. Hong, S. Ismail-Beigi, C. H. Ahn, F. J. Walker, *J. Vac. Sci. Technol., B: Microelectron. Nanometer Struct.-Process., Meas., Phenom.* **2009**, *27*, 2015.
- [211] D. P. Kumah, M. Dogan, J. H. Ngai, D. Qiu, Z. Zhang, D. Su, E. D. Specht, S. Ismail-Beigi, C. H. Ahn, F. J. Walker, *Phys. Rev. Lett.* **2016**, *116*, 106101.
- [212] D. P. Kumah, J. W. Reiner, Y. Segal, A. M. Kolpak, Z. Zhang, D. Su, Y. Zhu, M. S. Sawicki, C. C. Broadbridge, C. H. Ahn, F. J. Walker, *Appl. Phys. Lett.* **2010**, *97*, 251902.
- [213] A. M. Kolpak, F. J. Walker, J. W. Reiner, Y. Segal, D. Su, M. S. Sawicki, C. C. Broadbridge, Z. Zhang, Y. Zhu, C. H. Ahn, S. Ismail-Beigi, *Phys. Rev. Lett.* **2010**, *105*, 217601.
- [214] T. Chen, K. Ahmadi-Majlan, Z. H. Lim, Z. Zhang, J. H. Ngai, A. F. Kemper, D. P. Kumah, *Appl. Phys. Lett.* **2018**, *113*, 201601.
- [215] M. Sowwan, Y. Yacoby, J. Pitney, R. MacHarrie, M. Hong, J. Cross, D. A. Walko, R. Clarke, R. Pindak, E. A. Stern, *Phys. Rev. B* **2002**, *66*, 205311.
- [216] Y. Yacoby, M. Sowwan, E. Stern, J. Cross, D. Brewster, R. Pindak, J. Pitney, E. B. Dufresne, R. Clarke, *Phys. B* **2003**, *336*, 39.
- [217] J.-F. Ge, Z.-L. Liu, C. Liu, C.-L. Gao, D. Qian, Q.-K. Xue, Y. Liu, J.-F. Jia, *Nat. Mater.* **2014**, *14*, 285.
- [218] Q.-Y. Wang, Z. Li, W.-H. Zhang, Z.-C. Zhang, J.-S. Zhang, W. Li, H. Ding, Y.-B. Ou, P. Deng, K. Chang, J. Wen, C.-L. Song, K. He, J.-F. Jia, S.-H. Ji, Y.-Y. Wang, L.-L. Wang, X. Chen, X.-C. Ma, Q.-K. Xue, *Chin. Phys. Lett.* **2012**, *29*, 037402.
- [219] H. Ding, Y.-F. Lv, K. Zhao, W.-L. Wang, L. Wang, C.-L. Song, X. Chen, X.-C. Ma, Q.-K. Xue, *Phys. Rev. Lett.* **2016**, *117*, 067001.
- [220] R. Peng, H. C. Xu, S. Y. Tan, H. Y. Cao, M. Xia, X. P. Shen, Z. C. Huang, C. H. P. Wen, Q. Song, T. Zhang, B. P. Xie, X. G. Gong, D. L. Feng, *Nat. Commun.* **2014**, *5*, 5044.
- [221] K. Zou, S. Mandal, S. D. Albright, R. Peng, Y. Pu, D. Kumah, C. Lau, G. H. Simon, O. E. Dagdeviren, X. He, I. Božović, U. D. Schwarz, E. I. Altman, D. Feng, F. J. Walker, S. Ismail-Beigi, C. H. Ahn, *Phys. Rev. B* **2016**, *93*, 180506.
- [222] F. Li, Q. Zhang, C. Tang, C. Liu, J. Shi, C. Nie, G. Zhou, Z. Li, W. Zhang, C.-L. Song, K. He, S. Ji, S. Zhang, L. Gu, L. Wang, X.-C. Ma, Q.-K. Xue, *2D Mater.* **2016**, *3*, 024002.
- [223] I. C. Tung, A. Krishnamoorthy, S. Sadasivam, H. Zhou, Q. Zhang, K. L. Seyler, G. Clark, E. M. Mannebach, C. Nyby, F. Ernst, D. Zhu, J. M. Glowina, M. E. Kozina, S. Song, S. Nelson, H. Kumazoe, F. Shimojo, R. K. Kalia, P. Vashishta, P. Darancet, T. F. Heinz, A. Nakano, X. Xu, A. M. Lindenberg, H. Wen, *Nat. Photonics* **2019**, *13*, 425.
- [224] R. D. Averitt, A. J. Taylor, *J. Phys.: Condens. Matter* **2002**, *14*, R1357.
- [225] J. Shah, *Ultrafast Spectroscopy of Semiconductors and Semiconductor Nanostructures*, 2nd ed., Springer Series in Solid-State Sciences, Springer Verlag, New York **1999**.
- [226] D. Nicoletti, A. Cavalleri, *Adv. Opt. Photonics* **2016**, *8*, 401.
- [227] J. Zhang, R. D. Averitt, *Annu. Rev. Mater. Res.* **2014**, *44*, 19.

- [228] M. Buzzi, M. Först, A. Cavalleri, *Philos. Trans. R. Soc., A* **2019**, 377, 20170478.
- [229] M. Buzzi, M. Först, R. Mankowsky, A. Cavalleri, *Nat. Rev. Mater.* **2018**, 3, 299.
- [230] J. N. Clark, L. Beitra, G. Xiong, A. Higginbotham, D. M. Fritz, H. T. Lemke, D. Zhu, M. Chollet, G. J. Williams, M. Messerschmidt, B. Abbey, R. J. Harder, A. M. Korsunsky, J. S. Wark, I. K. Robinson, *Science* **2013**, 341, 56.
- [231] K. R. Beyerlein, *Proc. Natl. Acad. Sci. USA* **2018**, 115, 2044.
- [232] J. H. Lee, I. C. Tung, S. H. Chang, A. Bhattacharya, D. D. Fong, J. W. Freeland, H. Hong, *Rev. Sci. Instrum.* **2016**, 87, 013901.
- [233] J. H. Lee, G. Luo, I. C. Tung, S. H. Chang, Z. Luo, M. Malshe, M. Gadre, A. Bhattacharya, S. M. Nakhmanson, J. A. Eastman, H. Hong, J. Jellinek, D. Morgan, D. D. Fong, J. W. Freeland, *Nat. Mater.* **2014**, 13, 879.
- [234] D. D. Fong, C. A. Lucas, M. I. Richard, M. F. Toney, *MRS Bull.* **2011**, 35, 504.
- [235] E. Vlieg, A. W. D. van der Gon, J. F. van der Veen, J. E. Macdonald, C. Norris, *Phys. Rev. Lett.* **1988**, 61, 2241.
- [236] S. A. de Vries, W. J. Huisman, P. Goedtkindt, M. J. Zwanenburg, S. L. Bennett, I. K. Robinson, E. Vlieg, *Surf. Sci.* **1998**, 414, 159.
- [237] B. Jenichen, V. M. Kaganer, R. Shayduk, W. Braun, A. Trampert, *Phys. Status Solidi A* **2009**, 206, 1740.
- [238] V. M. Kaganer, B. Jenichen, R. Shayduk, W. Braun, *Phys. Rev. B* **2008**, 77, 125325.
- [239] G. Renaud, O. Robach, A. Barbier, *Faraday Discuss.* **1999**, 114, 157.
- [240] H. A. van der Vegt, J. Alvarez, X. Torrelles, S. Ferrer, E. Vlieg, *Phys. Rev. B* **1995**, 52, 17443.
- [241] P. H. Fuoss, D. W. Kisker, F. J. Lamelas, G. B. Stephenson, P. Imperatori, S. Brennan, *Phys. Rev. Lett.* **1992**, 69, 2791.
- [242] P. Fuoss, D. Kisker, G. Renaud, K. Tokuda, S. Brennan, J. Kahn, *Phys. Rev. Lett.* **1989**, 63, 2389.
- [243] D. W. Kisker, G. B. Stephenson, P. H. Fuoss, F. J. Lamelas, S. Brennan, P. Imperatori, *J. Cryst. Growth* **1992**, 124, 1.
- [244] D. W. Kisker, G. B. Stephenson, J. Tersoff, P. H. Fuoss, S. Brennan, *J. Cryst. Growth* **1996**, 163, 54.
- [245] D. D. Fong, C. Thompson, *Annu. Rev. Mater. Res.* **2006**, 36, 431.
- [246] G. B. Stephenson, D. D. Fong, M. V. Ramana Murty, S. K. Streiffer, J. A. Eastman, O. Auciello, P. H. Fuoss, A. Munkholm, M. E. M. Aanerud, C. Thompson, *Phys. B* **2003**, 336, 81.
- [247] J. D. Brock, J. D. Ferguson, Y. Kim, H.-Q. Wang, A. R. Woll, *Mater. Sci. Eng., A* **2010**, 528, 72.
- [248] J. D. Brock, J. D. Ferguson, A. R. Woll, *Metall. Mater. Trans. A* **2009**, 41, 1162.
- [249] G. Eres, J. Z. Tischler, M. Yoon, B. C. Larson, C. M. Rouleau, D. H. Lowndes, P. Zschack, *Appl. Phys. Lett.* **2002**, 80, 3379.
- [250] P. R. Willmott, C. M. Schlepütz, B. D. Patterson, R. Herger, M. Lange, D. Meister, D. Maden, C. Brönnimann, E. F. Eikenberry, G. Hülsen, A. Al-Adwan, *Appl. Surf. Sci.* **2005**, 247, 188.
- [251] T. K. Andersen, S. Cook, E. Benda, H. Hong, L. D. Marks, D. D. Fong, *Rev. Sci. Instrum.* **2018**, 89, 033905.
- [252] E. Annese, J. E. dos Santos, G. L. M. P. Rodrigues, A. S. Rocha, H. R. de Moraes, J. C. Cezar, *J. Synchrotron Radiat.* **2018**, 25, 1658.
- [253] H. Hong, T. C. Chiang, *Nucl. Instrum. Methods Phys. Res., Sect. A* **2007**, 572, 942.
- [254] S. Cook, K. Letchworth-Weaver, I. C. Tung, T. K. Andersen, H. Hong, L. D. Marks, D. D. Fong, *Sci. Adv.* **2019**, 5, eaav0764.
- [255] T. K. Andersen, S. Cook, G. Wan, H. Hong, L. D. Marks, D. D. Fong, *ACS Appl. Mater. Interfaces* **2018**, 10, 5949.
- [256] S. C. Petitto, K. S. Tanwar, S. K. Ghose, P. J. Eng, T. P. Trainor, *Surf. Sci.* **2010**, 604, 1082.
- [257] J. G. Catalano, C. Park, P. Fenter, Z. Zhang, *Geochim. Cosmochim. Acta* **2008**, 72, 1986.
- [258] R. P. Chiarello, N. C. Sturchio, *Geochim. Cosmochim. Acta* **1995**, 59, 4557.
- [259] Y. S. Chu, T. E. Lister, W. G. Cullen, H. You, Z. Nagy, *Phys. Rev. Lett.* **2001**, 86, 3364.
- [260] S. A. de Vries, P. Goedtkindt, S. L. Bennett, W. J. Huisman, M. J. Zwanenburg, D. M. Smilgies, J. J. De Yoreo, W. J. P. van Enckevort, P. Bennema, E. Vlieg, *Phys. Rev. Lett.* **1998**, 80, 2229.
- [261] S. A. de Vries, P. Goedtkindt, W. J. Huisman, M. J. Zwanenburg, R. Feidenhans'l, S. L. Bennett, D. M. Smilgies, A. Stierle, J. J. De Yoreo, W. J. P. van Enckevort, P. Bennema, E. Vlieg, *J. Cryst. Growth* **1999**, 205, 202.
- [262] P. Fenter, C. Park, N. C. Sturchio, *Geochim. Cosmochim. Acta* **2008**, 72, 1848.
- [263] P. Fenter, N. C. Sturchio, *Prog. Surf. Sci.* **2004**, 77, 171.
- [264] P. Geissbühler, P. Fenter, E. DiMasi, G. Srajer, L. B. Sorensen, N. C. Sturchio, *Surf. Sci.* **2004**, 573, 191.
- [265] T. E. Lister, Y. V. Tolmachev, Y. Chu, W. G. Cullen, H. You, R. Yonco, Z. Nagy, *J. Electroanal. Chem.* **2003**, 554–555, 71.
- [266] C. Park, P. A. Fenter, K. L. Nagy, N. C. Sturchio, *Phys. Rev. Lett.* **2006**, 97, 016101.
- [267] C. Park, P. A. Fenter, N. C. Sturchio, J. R. Regalbuto, *Phys. Rev. Lett.* **2005**, 94, 076104.
- [268] M. F. Reedijk, J. Arsic, F. F. A. Hollander, S. A. de Vries, E. Vlieg, *Phys. Rev. Lett.* **2003**, 90, 066103.
- [269] M. G. Samant, M. F. Toney, G. L. Borges, L. Blum, O. R. Melroy, *J. Phys. Chem.* **1988**, 92, 220.
- [270] M. L. Schlegel, K. L. Nagy, P. Fenter, L. Cheng, N. C. Sturchio, S. D. Jacobsen, *Geochim. Cosmochim. Acta* **2006**, 70, 3549.
- [271] M. L. Schlegel, K. L. Nagy, P. Fenter, N. C. Sturchio, *Geochim. Cosmochim. Acta* **2002**, 66, 3037.
- [272] N. C. Sturchio, R. P. Chiarello, L. Cheng, P. F. Lyman, M. J. Bedzyk, Y. Qian, H. You, D. Yee, P. Geissbühler, L. B. Sorensen, Y. Liang, D. R. Baer, *Geochim. Cosmochim. Acta* **1997**, 61, 251.
- [273] K. S. Lee, Y. K. Kim, S. Baik, J. Kim, I. I. S. Jung, *Appl. Phys. Lett.* **2001**, 79, 2444.
- [274] E. Zolotayabko, J. P. Quintana, B. H. Hoerman, B. W. Wessels, *Appl. Phys. Lett.* **2002**, 80, 3159.
- [275] O. R. Melroy, M. F. Toney, G. L. Borges, M. G. Samant, J. B. Kortright, P. N. Ross, L. Blum, *J. Electroanal. Chem. Interfacial Electrochem.* **1989**, 258, 403.
- [276] R. J. Randler, D. M. Kolb, B. M. Ocko, I. K. Robinson, *Surf. Sci.* **2000**, 447, 187.
- [277] M. F. Toney, J. G. Gordon, M. G. Samant, G. L. Borges, O. R. Melroy, L.-S. Kau, D. G. Wiesler, D. Yee, L. B. Sorensen, *Phys. Rev. B* **1990**, 42, 5594.
- [278] G. M. Bommarito, D. Acevedo, H. D. Abruna, *J. Phys. Chem.* **1992**, 96, 3416.
- [279] C. A. Lucas, N. M. Marković, P. N. Ross, *Surf. Sci.* **1999**, 425, L381.
- [280] A. Menzel, Y. V. Tolmachev, K. C. Chang, V. Komanicky, Y. S. Chu, J. J. Rehr, H. You, *Europhys. Lett.* **2006**, 74, 1032.
- [281] I. M. Tidswell, N. M. Marković, P. N. Ross, *Phys. Rev. Lett.* **1993**, 71, 1601.
- [282] C. Vericat, M. E. Vela, G. A. Andreassen, R. C. Salvarezza, F. Borgatti, R. Felici, T. L. Lee, F. Renner, J. Zegenhagen, J. A. Martín-Gago, *Phys. Rev. Lett.* **2003**, 90, 075506.
- [283] Y. S. Chu, H. You, J. A. Tanzer, T. E. Lister, Z. Nagy, *Phys. Rev. Lett.* **1999**, 83, 552.
- [284] E. Lundgren, J. Gustafson, A. Mikkelsen, J. N. Andersen, A. Stierle, H. Dosch, M. Todorova, J. Rogal, K. Reuter, M. Scheffler, *Phys. Rev. Lett.* **2004**, 92, 046101.
- [285] Z. Nagy, H. You, *Electrochim. Acta* **2002**, 47, 3037.
- [286] H. You, D. J. Zurawski, Z. Nagy, R. M. Yonco, *J. Chem. Phys.* **1994**, 100, 4699.
- [287] P. Fuoss, K.-C. Chang, H. You, *J. Electron Spectrosc. Relat. Phenom.* **2013**, 190, 75.

- [288] J. Gustafson, M. Shipilin, C. Zhang, A. Stierle, U. Hejral, U. Ruett, O. Gutowski, P. A. Carlsson, M. Skoglundh, E. Lundgren, *Science* **2014**, 343, 758.
- [289] T. Matsushita, T. Takahashi, T. Shirasawa, E. Arakawa, H. Toyokawa, H. Tajiri, *J. Appl. Phys.* **2011**, 110, 102209.
- [290] J. Fink, E. Schierle, E. Weschke, J. Geck, *Rep. Prog. Phys.* **2013**, 76, 056502.
- [291] A. Fasolino, P. Carra, M. Altarelli, *Phys. Rev. B* **1993**, 47, 3877.
- [292] S. Ferrer, J. Alvarez, E. Lundgren, X. Torrelles, P. Fajardo, F. Boscherini, *Phys. Rev. B* **1997**, 56, 9848.
- [293] G. M. Watson, D. Gibbs, G. H. Lander, B. D. Gaulin, L. E. Berman, H. Matzke, W. Ellis, *Phys. Rev. Lett.* **1996**, 77, 751.
- [294] G. M. Watson, D. Gibbs, G. H. Lander, B. D. Gaulin, L. E. Berman, H. Matzke, W. Ellis, *Phys. Rev. B* **2000**, 61, 8966.
- [295] J. Miao, T. Ishikawa, I. K. Robinson, M. M. Murnane, *Science* **2015**, 348, 530.
- [296] C. Zhu, R. Harder, A. Diaz, V. Komanicky, A. Barbour, R. Xu, X. Huang, Y. Liu, M. S. Pierce, A. Menzel, H. You, *Appl. Phys. Lett.* **2015**, 106, 101604.
- [297] C. Glorieux, E. Zolotoyabko, *J. Appl. Crystallogr.* **2001**, 34, 336.
- [298] N. Laanait, Z. Zhang, C. M. Schlepütz, *Nanotechnology* **2016**, 27, 374002.
- [299] K.-S. Kim, S.-Y. Chung, *IEEE Signal Process. Lett.* **2019**, 26, 1506.
- [300] J. Jiang, J. A. Fan, *Nano Lett.* **2019**, 19, 5366.